UNIVERSITÀ DEGLI STUDI
DI SALERNO

Dipartimento di Fisica "E.R. CAIANIELLO''
Università degli Studi di Salerno

Dottorato di Ricerca
in
MATEMATICA, FISICA ED APPLICAZIONI
curriculum: Fisica
XXX ciclo

Doctor of Phylosophy in *Mathematics, Physics and Applications*

Tesi di Dottorato in:

Electrical properties of pure and Co-substituted ZnO thin films investigated by UV-assisted SPM experiments

Domenico D'Agostino

Tutor:
Prof. Fabrizio Bobba
Università degli Studi di Salerno

Coordinator:
Prof. Roberto Scarpa
Università degli Studi di Salerno

2017/18

To my beloved family.

CONTENTS

Acronyms and Symbols

A-	Negatively charged adsorbates
a_0	Intermolecular distance
AFM	Atomic force microscope
ARPES	Angle-resolved photoemission spectroscopy
BCB	Bottom of the conduction band
C-AFM	Conductive atomic force microscopy
CB	Conduction band
CBM	Conduction band minimum
CS	Charge storage
DFT	Density functional theory
DFT+U	DFT with on-site Coulomb interaction
D-V	Cantilever-deflection vs DC-voltage
E_{CB}	Energy of the bottom level of the conduction band
E_D	Donor levels
EDS	Energy dispersive spectroscopy
E_F	Fermi energy
EFM	Electrostatic force microscopy
E_g	Band-gap energy
E_v	Vacuum energy
f_0	Free resonance frequency
F_{es}	Electro-static force
FESEM	Field emission scanning electron microscope
F_{int}	Interaction force
FWHM	Full-width-half-maximum
GGA	Generalized gradient approximation
GW	Green's function and Coulomb interaction approximation
h-e	Hole-electron pairs
HV	High vacuum
KPFM	Kelvin probe force microscopy
LDA	Local density approximation
L-J	Lennard-Jones
MEMS	Micro-electro-mechanical system
PFM	Piezo-response force microscopy

PLD	Pulsed laser deposition
P-S	Probe-sample
S_a	Arithmetic average of roughness profile
SEM	Scanning electron microscope
SPM	Scanning probe microscopy
SPV	Surface photo voltage
S_q	Root mean square
STM	Scanning tunnelling microscope
STS	Scanning tunnelling spectroscopy
TEM	Transmission electron microscope
UHV	Ultra high vacuum
UV	Ultra Violet
V_{AC}	AC voltage
VBM	Valence band maximum
V_{CPD}	Contact potential difference
V_{DC}	DC voltage
V_O	Oxygen vacancy
V_S	Band bending potential at surface
W	Work function
XANES	X-ray absorption near edge structure
XRD	X-ray diffraction
Zn_i	Interstitial Zinc
z_t	Separation distance between the probe and the sample surface
λ	Wavelength
Φ	Tunnelling barrier height
χ	Electron affinity

Figures and Tables

Abstract

ZnO is an intrinsic *n*-type, wide band-gap (3.4 eV at 0 K), semiconductor which has been attracted the interest of the scientific community for several decades. More recently, ZnO has caught a renewed interest due to the improvements in the epitaxial growth techniques as well as to the possibility of *p*-type conductivity and ferromagnetic behaviour as a consequence of cation doping. In addition to this, as it shows much stronger electric polarization effects than other wide-gap semiconductors, such as GaN and SiC, ZnO has a great potential for manufacturing energy-harvesting systems. Moreover, as ZnO is a semiconducting piezoelectric material, it is already widely used in electro-mechanical systems for making smart sensors and nano-actuators and in communications for surface acoustic wave and thin film bulk acoustic wave resonator devices. However, the potential applications of ZnO as well as of various transition-metal oxides, e.g. TiO2, V2O5, and SnO2, is affected by their electronic structure and surface chemistry. In particular, the material band structure can be properly designed and tuned by electron doping or atom substitution, whereas the stabilization of surface defects, chemistry and reactivity is still a largely unexplored field.

In this work the effect of Co-substitution on the electronic, electromechanical and surface properties of ZnO thin films (50 nm in thickness) has been deeply investigated. The substitution of Zn with Co atoms ensures no electrical doping, since the valence number of Zn and Co is the same. However, a 5% content of Co-substitution in ZnO has been previously shown to be enough to affect the electron conductivity of ZnO and to induce ferromagnetism in the semiconducting oxide. This behaviour has been theoretically addressed to the capability of Co to affect ZnO electronic band structure, by bonding the oxygen vacancies (typical ZnO intrinsic defects), introducing additional spin-polarized electronic levels close to the conduction band edge. Being spatially localized around the Co-complexes, these levels may alter the concentration of free carriers in intrinsically *n*-type ZnO, hence its bulk conductivity. These effects of Co-substitution on magnetic and conductive

properties of ZnO have been recently studied by means of “bulk” experimental (X-ray absorption near edge structure, Hall measurements, magnetization measurements, …) and theoretical investigation techniques (DFT, calculation for isolated defect in a crystal matrix, …). On the contrary, in the case of our nano-sized thin films (50 nm in thickness) it is of fundamental importance to distinguish between “bulk” effect of Co-substitution and surface properties as well as eventual high defect concentration. In this scenario, scanning probe microscopy based experiments, such as conductive atomic force microscopy, electrostatic force microscopy, Kelvin probe force microscopy and piezo-response force microscopy, have been used to study the effect of Co-substitution on ZnO surface reactivity, work function, piezoelectricity and charge storage. The complexity of the observed phenomena required a deep study in different environmental conditions, such as in air and ultra-high vacuum, dark and under monochromatic UV light irradiation. In this thesis, it will be demonstrated that Co-substitution (5% content) deeply affect ZnO work function, leading to a 410 meV downward shift of the Fermi level, towards the valence band, and surface reactivity, inhibiting the adsorption of reactive molecular species at the surface. On the contrary, it does not affect ZnO piezoelectricity and charge storage phenomenon. These findings will be discussed in the framework of existing theoretical model.

Introduction

Zinc Oxide (ZnO) is considered as a very promising material for semiconducting device applications[1,2]. It is a wide band-gap (3.2÷3.4eV at 300K)[3,4] metal oxide semiconductor, with a direct band-gap (i.e. conduction band minimum and valence band maximum occurring at the same *k*-point, Γ), as depicted in Figure 1a, extending in the near-UV energy region[5–9]. ZnO crystallizes in the wurtzite structure (Figure 1b) with possibility to have large single crystals[10], in contrast with other wurtzite-like semiconductors as GaN.

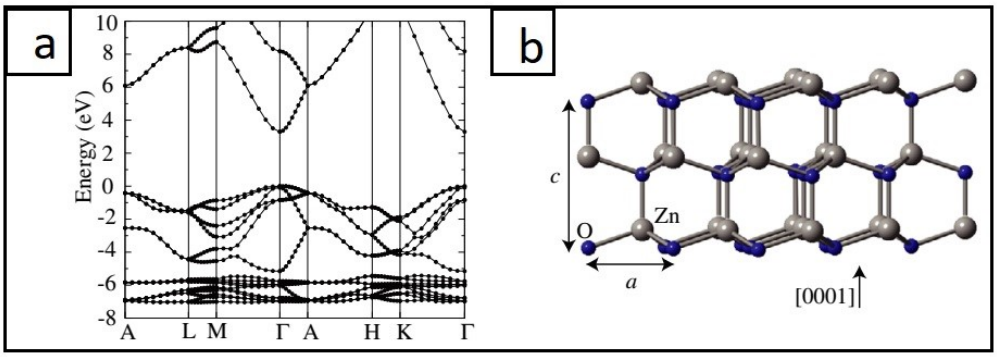

Figure 1 a Calculated energy diagram of ZnO[4]. **b** Wurtzite structure of ZnO.

Despite the fact that physical properties of ZnO have been studied since the beginning of the *semiconductors era*[4], the lack of control over its electric properties, as conductivity, (e.g. only *n*-type ZnO crystals were fabricated with high quality factors up to 1999)[4] discouraged researchers in using ZnO to fabricate semiconducting devices. Over the last two decades, the improvement of quality of ZnO thin films and the possibility to use it as substrate for other materials involved in optoelectronics and electronics (as GaN)[1,2,10] drove many research groups worldwide to control unintentional *n*-type doping of the material and try to achieve *p*-type conductivity. The increasing quality of ZnO films[4], the availability of large

single crystals[10], the discovery of exotic nanostructures[11], as well as the possibility to be used in bio-electronics application due to its biocompatibility[12,13] made ZnO a promising semiconducting material for new generation electronics.

Large efforts have been employed also in theoretical studies and in particular on first-principles calculations based on density functional theory for a deep understanding of the role of native impurities, point defects and for band-gap engineering[14–27] .

Controlling the conductivity in ZnO has remained a major issue. Even relatively small concentrations of native point defects and impurities (down to 10^{-14} cm^{-3} or 0.01 ppm) can significantly affect the electrical and optical properties of semiconductors[4]. Therefore, understanding the role of native point defects (i.e. vacancies, interstitials, and anti-sites) and the incorporation of impurities is key toward controlling the conductivity in ZnO. For a long time it has been postulated that the unintentional *n*-type conductivity in ZnO is caused by the presence of oxygen vacancies or zinc interstitials[28,29]. However, recent state-of-the-art density functional calculations corroborated by optically detected electron paramagnetic resonance measurements on high quality ZnO crystals have demonstrated that this attribution to native defects cannot be correct[15,16,20,22,26,30]. It has been shown that oxygen vacancies are actually deep donors and cannot contribute to *n*-type conductivity[20,30,31]. In addition, it was found that the other point defects (e.g. Zn interstitials and Zn anti-sites) are also unlikely causes of the observed *n*-type conductivity in as-grown ZnO crystals[22,26]. Instead, the cause would be related to the unintentional incorporation of impurities that act as shallow donors, such as hydrogen which is present in almost all growth and processing environments[14–26]. By means of density-functional calculations it has been shown that interstitial H forms a strong bond with O in ZnO and acts as a shallow donor, contrary to the amphoteric behaviour of interstitial H in conventional semiconductors[15]. Subsequently, interstitial H has been identified and characterized in ZnO[32,33]. However, interstitial H is highly mobile[34,35] and can easily diffuse out of the samples, making it difficult to explain the stability of the *n*-type conductivity at relatively high temperatures[36,37].

More recently, it has been suggested that H can also substitute for O in ZnO and act as a shallow donor[26]. Substitutional H is much more stable than interstitial H and can explain the stability of the *n*-type conductivity and its variation with oxygen partial pressure[26]. Other shallow-donor impurities that emerge as candidates to explain the unintentional *n*-type conductivity in ZnO are Ga, Al and In. However, these are not necessarily present in all samples in which *n*-type conductivity has been observed[38]. Obtaining *p*-type doping in ZnO has proved to be a very difficult task[1,2]. A reason lies in a lack of shallow acceptors in ZnO. Column-IA elements (Li, Na, K) on the Zn site are either deep acceptors or are also stable as interstitial donors that compensate *p*-type conductivity[35,39,40]. Column IB elements (Cu, Ag, Au) are deep acceptors and do not contribute to *p*-type conductivity. And because O is a highly electronegative first-row element, only N is likely to result in a shallow acceptor level in ZnO. The other column V elements (P, As, Sb) substituting on O sites are all deep acceptors[39]. Quite a few research groups have reported observing *p*-type conductivity in ZnO[41–47]. In order to explain the reports on *p*-type doping using P, As or Sb, it was suggested that these impurities would substitute for Zn and form complexes with two Zn vacancies[48]. One problem with this explanation is that these complexes have high formation energies and are unlikely to form. In addition, the reports on *p*-type ZnO using P, As or Sb often include unexpectedly high hole concentrations, and contain scant information about the crystal quality of the samples or the stability of the *p*-type conductivity[41–47].

On the other hand, the wide range of useful properties displayed by ZnO has been recognized for a long time[4]. What has captured most of the attention in recent years is the fact that ZnO is a semiconductor with a direct band gap[6-8], which in principle enables optoelectronic applications in the blue and UV regions of the spectrum. The prospect of such applications has been fuelled by impressive progress in bulk-crystal[49,50] as well as thin-film growth over the past few years[43,47,51-54]. A partial list of the properties of ZnO that distinguish it from other semiconductors or oxides or render it useful for applications includes:

- *Intrinsic n-type.* The as-grown ZnO bulk single crystals are always *n*-type irrespective of the growth method. The cause of this unintentional *n*-type

conductivity has been widely discussed in the literature, and has often been attributed to the presence of native point defects such as oxygen vacancies and zinc interstitials. However, recent first-principles calculations indicate that oxygen vacancy is actually a deep donor, and cannot contribute to the observed *n*-type conductivity. It has been then suggested that H can act as shallow donor when substituting Zn or O.

A review on sources of *n*-type conductivity in ZnO will be given in Chapter 1.1.

- *Direct and wide band gap.* The band gap of ZnO is 3.2÷3.4eV at 300K[3,4]. As mentioned above, this enables applications in optoelectronics in the blue/UV region, including light-emitting diodes, laser diodes and photo-detectors[1,2]. Optically pumped lasing has been reported in ZnO platelets[10], thin films[55], clusters consisting of ZnO nanocrystals[56] and ZnO nanowires[57]. Reports on *p*-*n* homo-junctions have recently appeared in the literature, but stability and reproducibility have not been established[45,47,58,59].
- *Large exciton binding energy.* The free-exciton binding energy in ZnO is 60 meV[10,55], compared with, e.g. 25 meV in GaN[60]. This large exciton binding energy indicates that efficient excitonic emission in ZnO can persist at room temperature and higher[10,55]. Since the oscillator strength of excitons is typically much larger than that of direct electron-hole transitions in direct gap semiconductors, the large exciton binding energy makes ZnO a promising material[4] for optical devices that are based on excitonic effects.
- *Large piezoelectric constants.* In piezoelectric materials, an applied voltage generates a deformation in the crystal and vice versa. These materials are generally used as sensors, transducers and actuators. The low symmetry of the wurtzite crystal structure combined with a large electromechanical coupling in ZnO gives rise to strong piezoelectric and pyro-electric properties. Piezoelectric ZnO films with uniform thickness and orientation have been grown on a variety of substrates using different deposition techniques, including sol-gel process, spray pyrolysis, chemical vapour deposition, molecular-beam epitaxy and sputtering[61-68].
- *Promising spin-tronics material.* ZnO is a very promising material for spin-tronics applications, with many groups reporting room-temperature ferromagnetism in films doped with transition metals (such as Co) during growth or by ion implantation. The control of spin-dependent phenomena in conventional semiconductors leads to devices such as spin-light-emitting diodes, spin-field effect transistors, and spin qu-bits for quantum computers.
- *Strong luminescence.* Due to a strong luminescence in the green-white region of the spectrum, ZnO is also a suitable material for phosphor applications. The emission spectrum has a peak at 495 nm and a very broad half-width of 0.4 eV[69]. The *n*-type conductivity of ZnO makes it appropriate for applications in vacuum fluorescent displays and field emission displays. The origin of the luminescence center and the luminescence mechanism are not really understood, being frequently attributed to oxygen vacancies or zinc interstitials, without any clear evidence. As we will discuss later, these defects cannot emit in the green region, and it has been suggested that zinc vacancies are a more likely cause of the

green luminescence. Zn vacancies are acceptors and likely to form in *n*-type ZnO.

- *Strong sensitivity of surface conductivity to the presence of adsorbed species.* The conductivity of ZnO thin films is very sensitive to the exposure of the surface to various gases. It can be used as a cheap smell sensor capable of detecting the freshness of foods and drinks, due to the high sensitivity to trimethylamine present in the odour[70]. The mechanisms of the sensor action are poorly understood. Recent experiments reveal the existence of a surface electron accumulation layer in vacuum annealed single crystals, which disappears upon exposure to ambient air[71-73]. This layer may play a role in sensor action, as well. The presence of this conducting surface channel has been suggested to be related to some puzzling type-conversion effects observed when attempting to obtain *p*-type ZnO[71-73].
- *Strong non-linear resistance of polycrystalline ZnO.* Commercially available ZnO varistors are made of semiconducting polycrystalline films with highly non-ohmic current‑voltage characteristics. While this nonlinear resistance has often been attributed to grain boundaries, the microscopic mechanisms are still not fully understood and the effects of additives and microstructures, as well as their relation to degradation mechanisms, are still under debate[74].
- *Large non-linear optical coefficients.* ZnO crystals and, in particular, thin films exhibit second- and third-order non-linear optical behaviour, suitable for non-linear optical devices. The linear and non-linear optical properties of ZnO depend on the crystallinity of the samples. ZnO films grown by laser deposition, reactive sputtering and spray pyrolysis show strong second-order non-linear response. Third-order non-linear response has recently been observed in ZnO nano-crystalline films[75]. The non-linear optical response in ZnO thin films is attractive for integrated non-linear optical devices.
- *High thermal conductivity.* This property makes ZnO useful as an additive (e.g. ZnO is added to rubber in order to increase the thermal conductivity of tires). It also increases the appeal of ZnO as a substrate for homo-epitaxy or hetero-epitaxy (e.g. for growth of GaN, which has a very similar lattice constant)[76,77]. High thermal conductivity translates into high efficiency of heat removal during device operation.
- *Availability of large single crystals.* One of the most attractive features of ZnO as a semiconductor is that large area single crystals are available, and epi-ready substrates are now commercialized. Bulk crystals can be grown with a variety of techniques, including hydrothermal growth[78], vapour-phase transport[49] and pressurized melt growth[79,80]. Growth of thin films can be accomplished using chemical vapour deposition[53,54], molecular-beam epitaxy[51,52], laser ablation[81] or sputtering[82]. The epitaxial growth of ZnO on native substrates can potentially lead to high quality thin films with reduced concentrations of extended defects. This is especially significant when compared with GaN, for which native substrates do not exist. In view of the fact that the GaN-based devices have achieved high efficiencies despite the relatively large concentration of extended defects, it is possible that a high-quality ZnO-based device could surpass the efficiencies obtained with GaN.

- *Amenability to wet chemical etching.* Semiconductor device fabrication processes greatly benefit from the amenability to low-temperature wet chemical etching. It has been reported that ZnO thin films can be etched with acidic, alkaline as well as mixture solutions. This possibility of low-temperature chemical etching adds great flexibility in the processing, designing and integration of electronic and optoelectronic devices.
- *Radiation hardness.* Radiation hardness is important for applications at high altitude or in space. It has been observed that ZnO exhibits exceptionally high radiation hardness[83,84], even greater than that of GaN, the cause of which is still unknown.

In addition to the above-mentioned properties and applications it is worth mentioning that, similarly to GaN based alloys (InGaN and AlGaN), it is possible to engineer the band gap of ZnO by adding Mg and/or Cd. Although CdO and MgO crystallize in the rock-salt structure, for moderate concentrations MgZnO and CdZnO assume the wurtzite structure of ZnO with band gaps in the range of 2.3 to 4.0 eV[85-90]. It is also worth noting that ZnO substrates offer a perfect lattice match to $In_{0.22}Ga_{0.78}N$, which has a band gap highly suitable for visible light emission. ZnO has also attracted attention due to the possibility of making thin-film transistors on flexible substrates with relatively high electron mobility when compared with amorphous silicon or organic semiconductors[91-93].

This work is aimed to explore the most intriguing and application-ready properties of ZnO, in particular the relationship between the band structure and the UV photo-response, the large piezo-electric effect and the strong sensitivity of the surface to adsorbed gas species. Moreover, it will expand the investigation of such properties down to the nano-scale by using scanning probe microscopy techniques. Paired samples of pristine and Co-substituted ZnO will be time by time studied and results compared in order to infer about the effect of Co on pristine properties. In particular, a topic concentration of 5% has been chosen for Co, to substitute Zn, since it has been proved that in such a concentration it confers magnetic properties to ZnO[94] and forms bonded complexes with intrinsic defects as oxygen vacancies[95,96]. Such complexes are accounted to introduce additional electronic levels into ZnO band structure and then modify UV photo-responsive properties, as well as piezoelectric and conductive behaviours via crystalline structure degradation[81]. On the other hand,

SPM were used to get inside conductive, electrostatic and electro-mechanic properties at nano-scale as successfully reported by Di Trolio *et al.*[97], Qi *et al.*[98], Brillson *et al.*[99] , D' Agostino *et al.*[81]. In this framework it has been possible to explore size effects together with a deep comprehension of photo-induced phenomena by using Co-substitution to modify electronic properties of ZnO.

In Chapter 1 a review of the fundamental properties of ZnO will be given, in order to get inside the questions debated in this work, spanning from the unintentional doping, surface properties of ZnO, to the Co-substitution.

Chapter 2 will be devoted to the illustration of experimental techniques and systems used in the present thesis, with particular regards to fabrication techniques, used to produce samples, and SPMs, exploited to study properties for interest.

Chapter 3 will present results of structural characterization of fabricated samples, photo-induced effects, as well as electro-mechanical and charge storing properties of pristine and Co-substituted ZnO materials. Each section will be ended by a discussion on results.

Finally, Chapter 4 will summarize findings and conclude the work.

BIBLIOGRAPHY

1. Look, D. C. Recent advances in ZnO materials and devices. *Mater. Sci. Eng. B* **80,** 383–387 (2001).

2. Özgür, Ü. *et al.* A comprehensive review of ZnO materials and devices. *J. Appl. Phys.* **98,** 41301 (2005).

3. Kittel, C. *Introduction to Solid State Physics*. (Wiley, 2004).

4. Janotti, A. & Van De Walle, C. G. Fundamentals of zinc oxide as a semiconductor. *Reports Prog. Phys.* **72,** (2009).

5. Thomas, D. G. The exciton spectrum of zinc oxide. *J. Phys. Chem. Solids* **15,** 86–96 (1960).

6. Mang, A., Reimann, K. & Rübenacke, S. Band gaps, crystal-field splitting, spin-orbit coupling, and exciton binding energies in ZnO under hydrostatic pressure. *Solid State Commun.* **94,** 251–254 (1995).

7. Reynolds, D. C. *et al.* Valence-band ordering in ZnO. *Phys. Rev. B* **60,** 2340–2344 (1999).

8. Chen, Y. *et al.* Plasma assisted molecular beam epitaxy of ZnO on c -plane sapphire: Growth and characterization. *J. Appl. Phys.* **84,** 3912–3918 (1998).

9. Srikant, V. & Clarke, D. R. On the optical band gap of zinc oxide. *J. Appl. Phys.* **83,** 5447–5451 (1998).

10. Reynolds, D. C., Look, D. C. & Jogai, B. Optically pumped ultraviolet lasing from ZnO. *Solid State Commun.* **99,** 873–875 (1996).

11. Wang, Z. L. Zinc oxide nanostructures: growth, properties and applications. *J. Phys. Condens. Matter* **16,** R829–R858 (2004).

12. Gopikrishnan, R. *et al.* Synthesis, Characterization and Biocompatibility Studies of Zinc oxide (ZnO) Nanorods for Biomedical Application. *Nano-Micro Lett.* **2,** (2010).

13. Zhao, L.-H., Zhang, R., Zhang, J. & Sun, S.-Q. Synthesis and characterization of biocompatible ZnO nanoparticles. *CrystEngComm* **14,** 945–950 (2012).

14. Van de Walle, C. G. Hydrogen as a Cause of Doping in Zinc Oxide. *Phys. Rev. Lett.* **85,** 1012–1015 (2000).

15. Kohan, A. F., Ceder, G., Morgan, D. & Van de Walle, C. G. First-principles study of native point defects in ZnO. *Phys. Rev. B* **61,** 15019–15027 (2000).

16. Van de Walle, C. G. Defect analysis and engineering in ZnO. *Phys. B Condens. Matter* **308–310,** 899–903 (2001).

17. Zhang, S. B., Wei, S.-H. & Zunger, A. Intrinsic n -type versus p -type doping asymmetry and the defect physics of ZnO. *Phys. Rev. B* **63,** 75205 (2001).

18. Oba, F., Nishitani, S. R., Isotani, S., Adachi, H. & Tanaka, I. Energetics of native defects in ZnO. *J. Appl. Phys.* **90,** 824–828 (2001).

19. Lee, E.-C., Kim, Y.-S., Jin, Y.-G. & Chang, K. J. Compensation mechanism for N acceptors in ZnO. *Phys. Rev. B* **64,** 85120 (2001).

20. Janotti, A. & Van de Walle, C. G. Oxygen vacancies in ZnO. *Appl. Phys. Lett.* **87,** 122102 (2005).

21. Erhart, P., Klein, A. & Albe, K. First-principles study of the structure and stability of oxygen defects in zinc oxide. *Phys. Rev. B* **72,** 85213 (2005).

22. Janotti, A. & Van de Walle, C. G. New insights into the role of native point defects in ZnO. *J. Cryst. Growth* **287,** 58–65 (2006).

23. Erhart, P. & Albe, K. First-principles study of migration mechanisms and diffusion of oxygen in zinc oxide. *Phys. Rev. B* **73,** 115207 (2006).

24. Lany, S. & Zunger, A. Anion vacancies as a source of persistent photoconductivity in II-VI and chalcopyrite semiconductors. *Phys. Rev. B* **72,** 35215 (2005).

25. Janotti, A. & Van de Walle, C. G. Hydrogen multicentre bonds. *Nat. Mater.* **6,** 44–47 (2007).

26. Janotti, A. & Van de Walle, C. G. Native point defects in ZnO. *Phys. Rev. B* **76,** 165202 (2007).

27. Oba, F., Togo, A., Tanaka, I., Paier, J. & Kresse, G. Defect energetics in ZnO: A hybrid Hartree-Fock density functional study. *Phys. Rev. B* **77,** 245202 (2008).

28. Harrison, S. E. Conductivity and Hall Effect of ZnO at Low Temperatures. *Phys. Rev.* **93,** 52–62 (1954).

29. Hutson, A. R. Hall Effect Studies of Doped Zinc Oxide Single Crystals. *Phys. Rev.* **108,** 222–230 (1957).

30. Vlasenko, L. S. & Watkins, G. D. Optical detection of electron paramagnetic

resonance in room-temperature electron-irradiated ZnO. *Phys. Rev. B* **71,** 125210 (2005).

31. Vlasenko, L. S. & Watkins, G. D. Optical detection of electron paramagnetic resonance for intrinsic defects produced in ZnO by 2.5-MeV electron irradiation in situ at 4.2 K. *Phys. Rev. B* **72,** 35203 (2005).

32. Cox, S. F. J. *et al.* Experimental Confirmation of the Predicted Shallow Donor Hydrogen State in Zinc Oxide. *Phys. Rev. Lett.* **86,** 2601–2604 (2001).

33. McCluskey, M. D., Jokela, S. J., Zhuravlev, K. K., Simpson, P. J. & Lynn, K. G. Infrared spectroscopy of hydrogen in ZnO. *Appl. Phys. Lett.* **81,** 3807–3809 (2002).

34. Thomas, D. G. & Lander, J. J. Hydrogen as a Donor in Zinc Oxide. *J. Chem. Phys.* **25,** 1136–1142 (1956).

35. Wardle, M. G., Goss, J. P. & Briddon, P. R. Theory of Li in ZnO: A limitation for Li-based *p*-type doping. *Phys. Rev. B* **71,** 155205 (2005).

36. Jokela, S. J. & McCluskey, M. D. Structure and stability of O-H donors in ZnO from high-pressure and infrared spectroscopy. *Phys. Rev. B* **72,** 113201 (2005).

37. Shi, G. A. *et al.* Hydrogen local modes and shallow donors in ZnO. *Phys. Rev. B* **72,** 195211 (2005).

38. McCluskey, M. D. & Jokela, S. J. Sources of n-type conductivity in ZnO. *Phys. B Condens. Matter* **401–402,** 355–357 (2007).

39. Park, C. H., Zhang, S. B. & Wei, S.-H. Origin of p -type doping difficulty in ZnO: The impurity perspective. *Phys. Rev. B* **66,** 73202 (2002).

40. Lee, E.-C. & Chang, K. J. Possible *p*-type doping with group-I elements in ZnO. *Phys. Rev. B* **70,** 115210 (2004).

41. Minegishi, K. *et al.* Growth of *p*-type Zinc Oxide Films by Chemical Vapor Deposition. *Jpn. J. Appl. Phys.* **36,** L1453–L1455 (1997).

42. Joseph, M., Tabata, H. & Kawai, T. *p*-Type Electrical Conduction in ZnO Thin Films by Ga and N Codoping. *Jpn. J. Appl. Phys.* **38,** L1205–L1207 (1999).

43. Look, D. C. *et al.* Characterization of homoepitaxial *p* -type ZnO grown by molecular beam epitaxy. *Appl. Phys. Lett.* **81,** 1830–1832 (2002).

44. Kim, K.-K., Kim, H.-S., Hwang, D.-K., Lim, J.-H. & Park, S.-J. Realization of *p*-type ZnO thin films via phosphorus doping and thermal activation of the dopant. *Appl. Phys. Lett.* **83,** 63–65 (2003).

45. Ryu, Y. R., Kim, W. J. & White, H. W. Fabrication of homostructural ZnO p–n junctions. *J. Cryst. Growth* **219,** 419–422 (2000).

46. Xiu, F. X. *et al.* High-mobility Sb-doped *p*-type ZnO by molecular-beam epitaxy. *Appl. Phys. Lett.* **87,** 152101 (2005).

47. Ohtomo, A. & Tsukazaki, A. Pulsed laser deposition of thin films and superlattices based on ZnO. *Semicond. Sci. Technol.* **20,** S1–S12 (2005).

48. Limpijumnong, S., Zhang, S. B., Wei, S.-H. & Park, C. H. Doping by Large-Size-Mismatched Impurities: The Microscopic Origin of Arsenic- or Antimony-Doped *p*-Type Zinc Oxide. *Phys. Rev. Lett.* **92,** 155504 (2004).

49. Look, D. C. *et al.* Electrical properties of bulk ZnO. *Solid State Commun.* **105,** 399–401 (1998).

50. Maeda, K., Sato, M., Niikura, I. & Fukuda, T. Growth of 2 inch ZnO bulk single crystal by the hydrothermal method. *Semicond. Sci. Technol.* **20,** S49–S54 (2005).

51. Heinze, S. *et al.* Homoepitaxial growth of ZnO by metalorganic vapor phase epitaxy in two-dimensional growth mode. *J. Cryst. Growth* **308,** 170–175 (2007).

52. Dadgar, A. *et al.* Heteroepitaxy and nitrogen doping of high-quality ZnO. *J. Cryst. Growth* **272,** 800–804 (2004).

53. Ive, T. *et al.* Step-flow growth of ZnO(0001) on GaN(0001) by metalorganic chemical vapor epitaxy. *J. Cryst. Growth* **310,** 3407–3412 (2008).

54. Bierwagen, O., Ive, T., Van de Walle, C. G. & Speck, J. S. Causes of incorrect carrier-type identification in van der Pauw–Hall measurements. *Appl. Phys. Lett.* **93,** 242108 (2008).

55. Bagnall, D. M. *et al.* Optically pumped lasing of ZnO at room temperature. *Appl. Phys. Lett.* **70,** 2230–2232 (1997).

56. Cao, H. *et al.* Random Laser Action in Semiconductor Powder. *Phys. Rev. Lett.* **82,** 2278–2281 (1999).

57. Huang, M. H. Room-Temperature Ultraviolet Nanowire Nanolasers. *Science (80-.).* **292,** 1897–1899 (2001).

58. Mandalapu, L. J., Yang, Z., Xiu, F. X., Zhao, D. T. & Liu, J. L. Homojunction photodiodes based on Sb-doped *p*-type ZnO for ultraviolet detection. *Appl. Phys. Lett.* **88,** 92103 (2006).

59. Chu, S., Olmedo, M., Yang, Z., Kong, J. & Liu, J. Electrically pumped ultraviolet

ZnO diode lasers on Si. *Appl. Phys. Lett.* **93,** 181106 (2008).

60. Madelung, O. *Semiconductors - Basic Data*. (Springer, 1996).

61. Kamalasanan, M. N. & Chandra, S. Sol-gel synthesis of ZnO thin films. *Thin Solid Films* **288,** 112–115 (1996).

62. Paraguay D., F., Estrada L., W., Acosta N., D. R., Andrade, E. & Miki-Yoshida, M. Growth, structure and optical characterization of high quality ZnO thin films obtained by spray pyrolysis. *Thin Solid Films* **350,** 192–202 (1999).

63. Funakubo, H., Mizutani, N., Yonetsu, M., Saiki, A. & Shinozaki, K. No Title. *J. Electroceramics* **4,** 25–32 (1999).

64. Sakurai, K. *et al.* Effects of oxygen plasma condition on MBE growth of ZnO. *J. Cryst. Growth* **209,** 522–525 (2000).

65. Yamamoto, T., Shiosaki, T. & Kawabata, A. Characterization of ZnO piezoelectric films prepared by rf planar-magnetron sputtering. *J. Appl. Phys.* **51,** 3113–3120 (1980).

66. Molarius, J. No Title. *J. Mater. Sci. Mater. Electron.* **14,** 431–435 (2003).

67. Ondo-Ndong, R., Ferblantier, G., Pascal-Delannoy, F., Boyer, A. & Foucaran, A. Electrical properties of zinc oxide sputtered thin films. *Microelectronics J.* **34,** 1087–1092 (2003).

68. Gardeniers, J. G. E., Rittersma, Z. M. & Burger, G. J. Preferred orientation and piezoelectricity in sputtered ZnO films. *J. Appl. Phys.* **83,** 7844–7854 (1998).

69. Stavale, F., Nilius, N. & Freund, H. J. STM luminescence spectroscopy of intrinsic defects in ZnO(0001) thin films. *J. Phys. Chem. Lett.* **4,** 3972–3976 (2013).

70. Nanto, H., Sokooshi, H. & Usuda, T. Sol. *Solid State Sensors and Actuators* **24–27,** 596 (1991).

71. Schmidt, O. *et al.* Effects of an Electrically Conducting Layer at the Zinc Oxide Surface. *Jpn. J. Appl. Phys.* **44,** 7271–7274 (2005).

72. Schmidt, O. *et al.* Analysis of a conducting channel at the native zinc oxide surface. *Superlattices Microstruct.* **39,** 8–16 (2006).

73. Look, D. C. Quantitative analysis of surface donors in ZnO. *Surf. Sci.* **601,** 5315–5319 (2007).

74. Eda, K. Zinc oxide varistors. *IEEE Electr. Insul. Mag.* **5,** 28–30 (1989).

75. Larciprete, M. C. *et al.* Characterization of second and third order optical nonlinearities of ZnO sputtered films. *Appl. Phys. B* **82,** 431–437 (2006).

76. Florescu, D. I. *et al.* High spatial resolution thermal conductivity of bulk ZnO (0001). *J. Appl. Phys.* **91,** 890–892 (2002).

77. Özgür, Ü. *et al.* Thermal conductivity of bulk ZnO after different thermal treatments. *J. Electron. Mater.* **35,** 550–555 (2006).

78. Ohshima, E. *et al.* Growth of the 2-in-size bulk ZnO single crystals by the hydrothermal method. *J. Cryst. Growth* **260,** 166–170 (2004).

79. Reynolds, D. C. *et al.* High-quality, melt-grown ZnO single crystals. *J. Appl. Phys.* **95,** 4802–4805 (2004).

80. Nause, J. & Nemeth, B. Pressurized melt growth of ZnO boules. *Semicond. Sci. Technol.* **20,** S45–S48 (2005).

81. D'Agostino, D. *et al.* Piezoelectricity and charge trapping in ZnO and Co-doped ZnO thin films. *AIP Adv.* **7,** 55010 (2017).

82. Quaranta, F., Valentini, A., Rizzi, F. R. & Casamassima, G. Dual-ion-beam sputter deposition of ZnO films. *J. Appl. Phys.* **74,** 244–248 (1993).

83. Tuomisto, F., Saarinen, K., Look, D. C. & Farlow, G. C. Introduction and recovery of point defects in electron-irradiated ZnO. *Phys. Rev. B* **72,** 85206 (2005).

84. Look, D. C., Hemsky, J. W. & Sizelove, J. R. Residual Native Shallow Donor in ZnO. *Phys. Rev. Lett.* **82,** 2552–2555 (1999).

85. Ohtomo, A. *et al.* MgxZn1−xO as a II–VI widegap semiconductor alloy. *Appl. Phys. Lett.* **72,** 2466–2468 (1998).

86. Ohtomo, A. *et al.* Room-temperature stimulated emission of excitons in ZnO/(Mg, Zn)O superlattices. *Appl. Phys. Lett.* **77,** 2204–2206 (2000).

87. Jin, Y. *et al.* Room temperature UV emission of MgxZn1−xO films. *Solid State Commun.* **119,** 409–413 (2001).

88. Makino, T. *et al.* Band gap engineering based on MgxZn1−xO and CdyZn1−yO ternary alloy films. *Appl. Phys. Lett.* **78,** 1237–1239 (2001).

89. Gruber, T., Kirchner, C., Kling, R., Reuss, F. & Waag, A. ZnMgO epilayers and ZnO–ZnMgO quantum wells for optoelectronic applications in the blue and UV spectral region. *Appl. Phys. Lett.* **84,** 5359–5361 (2004).

90. Gruber, T. *et al.* Optical and structural analysis of ZnCdO layers grown by

metalorganic vapor-phase epitaxy. *Appl. Phys. Lett.* **83,** 3290–3292 (2003).

91. Nomura, K. *et al.* Room-temperature fabrication of transparent flexible thin-film transistors using amorphous oxide semiconductors. *Nature* **432,** 488–492 (2004).

92. Hoffman, R. L., Norris, B. J. & Wager, J. F. ZnO-based transparent thin-film transistors. *Appl. Phys. Lett.* **82,** 733–735 (2003).

93. Hoffman, R. L. ZnO-channel thin-film transistors: Channel mobility. *J. Appl. Phys.* **95,** 5813–5819 (2004).

94. Ciatto, G. *et al.* Defect-induced magnetism in cobalt-doped ZnO epilayers. **332,** 332–336 (2014).

95. Di Trolio, A. *et al.* The effect of Co doping on the conductive properties of ferromagnetic $Zn_x Co_{1-x} O$ films. *J. Mater. Chem. C* **3,** 10188–10194 (2015).

96. Ciatto, G. *et al.* Evidence of cobalt-vacancy complexes in Zn1-xCoxO dilute magnetic semiconductors. *Phys. Rev. Lett.* **107,** 1–5 (2011).

97. Di Trolio, A. *et al.* Ferromagnetism and Conductivity in Hydrogen Irradiated Co-Doped ZnO Thin Films. *ACS Appl. Mater. Interfaces* **8,** 12925–12931 (2016).

98. Qi, J., Olmedo, M., Zheng, J. G. & Liu, J. Multimode resistive switching in single ZnO nanoisland system. *Sci. Rep.* **3,** 1–6 (2013).

99. Brillson, L. J. & Lu, Y. ZnO Schottky barriers and Ohmic contacts. *J. Appl. Phys.* **109,** (2011).

1. Material properties of ZnO

1.1 *n*-type conductivity

The unintentional *n*-type doping of ZnO is a largely debated question[1–9]. In addition to this, the *p*-type ZnO is hard to obtain[10,11] and one of the reasons is that intrinsic defects actually play a role in compensating acceptor centers of *p*-doping[12–14]. For example, some elements from Column IA as Li, Na and K on the ZnO site are too deep (in the energy diagram) acceptors and interstitial Zn easily compensate *p*-type behaviour[15,16]. Cu Ag and Au, from Column IB should be excluded as acceptors since their deep energy position in band structure while, on the first row, only N can be take into account as shallow acceptor but its stability in the ZnO lattice is debated[17]. However, in literature few successful attempts in achieving *p*-type conductivity are reported[18–24]. A key role in compensating *p*-type conductivity is played by native, or intrinsic, point defects that are imperfection of the crystal lattice involving only constituent elements. The deep knowledge of such defects is crucial as they strongly influence the electrical as well as optical properties of the semiconductor acting on doping, carrier lifetime, luminescence and degradation processes of the devices. The abundance of native defects can be controlled in different ways, from tuning the fabrication process to post growth treatments. In the case of ZnO, intrinsic point defects include *vacancies* of atoms at expected regular lattice positions, *interstitial atoms* as atoms occupying interstices in the lattice and *anti-sites* as a Zn occupying the site of an O and vice-versa. The unintentional *n*-type conductivity of ZnO has been often correlated with the presence of those defects and, in particular, oxygen vacancies and interstitial zinc[25–30]. On the other hand, more recently, it has been pointed out that a possible incorporation of hydrogen during fabrication processes of ZnO can lead to the high level of *n*-type conductivity[4,9]. Due to its low kinetic radius, H_2 is hard to eliminate from fabrication chambers and, although it can be pumped away by ionic-pumps, it can penetrate from very small (atom like) leaks of

the systems. In addition to this, the presence of eventual low-vacuum sealing of gas inlet and cooling circuits can act as way in for hydrogen molecule[4,9]. The question has been longer debated. Look et al. ascribed the *n*-type conduction to interstitial zinc (Zn_i) and oxygen vacancies (V_O) [6], while in the same period Van de Walle pointed out the possible role of unintentionally incorporated H as shallow donor in ZnO, by means of Density Functional Theory (DFT) calculations within the local density approximation (LDA). Moreover, within the same theoretical framework, energy levels of V_O and Zn_i were demonstrated to be too deep in the energy diagram[4]. DFT-calculated formation energies of several point defects in ZnO further excluded a dominant role of intrinsic defects as origin for the *n*-type conductivity[2]. On the other hand, H was demonstrated to act as amphoteric impurity in semiconductors, reducing the effective doping of the material since it can behave as acceptor when in presence of *n*-type doping and donor when in presence of *p*-type material[31]. However, as demonstrated by Van de Walle by means of DFT calculations, H acts only as donor, thus efficiently contributing to ZnO unintentional *n*-type doping[9]. Selim et al. dedicated a full review on native defects in ZnO where V_O and Zn_i were excluded to contribute to *n*-type nature of ZnO and H was accounted to be a shallow donor only if occupying an oxygen sub-lattice, i.e. in V_o-H complexes[32]. This result was then confirmed by Nahm et al. in 2014 with a large discussion on hydrogen substituting oxygen and the effect of complex formation on photoconduction[3].

1.2 Band structure in the bulk

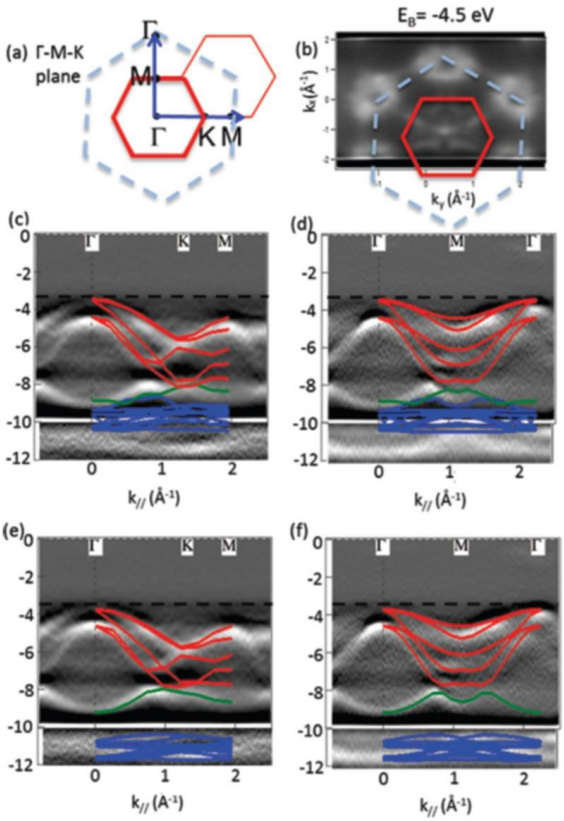

Figure 1. 1 $k_{||}$ scans in hexagonal plane of the ZnO Brillouin zone and comparison between experimental and theoretical band structure. A photon energy of 135 eV was chosen to study the Γ-M-K basal plane. **(a)** The Γ-M-K plane and **(b)** its constant-energy contour plot of the photoemission intensity. The red lines denote Brillouin zone boundaries, and the dashed blue lines are connectors to the Γ points. The arrows indicate the sliced directions measured. **(c)** and **(d)** Comparison between experimental band structure (grey scale) and theoretical band structure within the GW approximation. The origin of energy is chosen at the conduction band minimum. The red lines represent *p*-O bands, the green lines hybridized *s*-Zn/*p*-O bands, and the blue line *d*-Zn bands. It can be seen that the *d*-Zn band is too high, and there is overlap with the *s*-Zn/*p*-O bands. **(e)** and **(f)** Comparison between experimental band structure (grey scale) and theoretical band structure within the GW with *on-site* potential. The *d*-Zn band is no longer too high, and the *s*-Zn/*p*-O and *d*-Zn bands do not overlap[43].

Great efforts have been made to understand, both experimentally and theoretically, the electronic structure of ZnO. Theoretical first principles calculations for ZnO band structure were largely reported in literature with a lack of agreement with experimental data. DFT in the LDA and the generalized gradient approximation (GGA)[33–36] dramatically underestimate the band gap, resulting in a band gap value of less than 1eV compared to the experimental gap of 3.44eV[37]. In general, electronic structure calculation as LDA deal well with ordinary *s-p* materials, such as GaAs or Si, but the stronger self-interaction energy of active *d*-electron materials pose a problem to these methods[33]. The large discrepancy in band gap value between calculations and experiments for ZnO is ascribed to the underestimated binding energy of the *d*-Zn shell[33]. In order to calculate band gap value that well agree to experiments it has been essential to go beyond DFT. For a semiconducting periodic system, it is usually done by calculating the electron self-energy by dealing with Green's function (*G*) and Coulomb interaction (*W*) in the so called GW approximation[38]. However, recent GW calculations for ZnO, including quasi-particle self-consistent GW methods place the *d*-Zn band too high in energy by about 1eV[39–42]. Lim et al. addressed the question by considering an *on-site* potential for *d*-Zn states in order to correct the *d*-band energy. When the *d*-Zn band energy is shifted down by applying an on-site potential during GW calculations to match the experimental *d* band position, an improved value for the band gap is found, resulting in 3.3eV[43]. The ZnO band structure, indeed, has been probed experimentally by angle-resolved photoemission spectroscopy (ARPES) using photons in both the UV region[44] and in soft x-ray region[45]. Figure 1.1 is a comprehensive review of measured band structure of ZnO by means of ARPES and results obtained by GW calculation with and without the addition of the *on-site* potential. The arrows in Figure 1.1(a) sketched out the sliced directions in the Γ-M-K plane where the ARPES measurements were taken, and in Figure 1.1(b) the constant-energy contour plot shows an hexagonal symmetry, reflecting the hexagonal Brillouin zone of the wurtzite ZnO. The valence band maximum (VBM) is located at the binding energy $E_B \sim -3.45$eV and the Fermi level is approximately located near the conduction band minimum (CBM) due to *n*-type nature of ZnO. The ZnO valence band structure can

be partitioned into three segments: (1) the *p*-O bands (red solid lines superimposed to ARPES spectra) at −3.5eV <E_B< −7.5 eV, (2) the *s*-Zn/*p*-O band (green solid lines superimposed to ARPES spectra) at −7.5eV <E_B< −9.5eV, which is formed for the hybridization between empty *s* states of the Zn^{2+} cation and occupied *p* states of the O^{2-} anion, and (3) the *d*-Zn bands (blue lines superimposed to ARPES spectra) at −10eV <E_B< −12eV. The positions of *p*-O and *d*-Zn bands are confirmed experimentally by resonant photoemission of *p*-O states[43]. Figures 1.1(c) and 1.1(d) are ARPES measurements (in grey scale) with superimposed calculated band structures. It turns out the difficulty in correctly predicting the *d* band position and the *p*-O band dispersion with GW calculations. It is worth noting that the under-binding of the *d*-Zn states also causes a spurious mixing with the *s*-Zn/*p*-O band, as seen in Figs. 1.1(c) and 1.1(d). In addition to this, a small band gap of 2.92 eV is also calculated, ascribed to the too-high *d* band energy, pushing the VBM to higher energies. Figures 1.1(e) and 1.1(f) have the same meaning of Figures 1.1(c) and (d), with the only difference that the superimposed simulated band structures was calculated with GW plus *on-site* potential. In this case calculated band structure agrees with measured one. The position of the *d* band is shifted down and the calculated band gap value is 3.3eV very close to the measured 3.44eV[43]**.**

1.3 Surface band structure and its modification in presence of adsorbates

Chemical processes on metal oxide surfaces have attracted great interest for a long time, due to their relevance in the field of *heterogeneous catalysis*. Perfect oxide surfaces usually do not show any reactivity to gas species, but real material, like oxide powders, are known to be highly reactive due to the presence of a number of active sites on their surface[46]. Most of the models proposed for these active sites evoke oxygen vacancies or other defects at semiconductor surface[47].

ZnO surface is extremely reactive to gas molecules and in particular it has been used as fundamental material for developing gas sensors[48,49] as well as catalysing chemical reaction[47]. In this sense, a deep interplay between unintentional *n*-type doping of ZnO and the band structure modifications induced in the bulk and at the surface is a key to understand the high reactivity of this semiconductor surface to gas atoms. The breaking of the translational symmetry at the surface of a solid leads to the occurrence of electronic states which have no analogue in the crystal bulk[50]. In semiconductors, unlike in metals, these states can lead to charged layers, where the concentration of carriers varies significantly with the distance relative to the surface, causing electric fields with strengths on the order of $10 MV cm^{-1}$, decaying in a region of ≈100nm in thickness from the surface [51].

In addition to this, the work function drastically changes when a pristine surface is covered with adsorbates. Let us first consider the expression of the work function for a semiconductor $W_{Semicond.}=(E_v-E_F)\pm eV_S = \chi-(E_{CB}-E_F)\pm eV_S$, where E_v and E_F are the vacuum energy and the Fermi energy, respectively, χ is the electron affinity, E_{CB} is the energy of the bottom level of the conduction band, V_S is the band bending potential at surface due to the localized surface charges A^-, compensated by a number of ionized donors in the depletion layer. It is worth noting that the expression of $W_{Semicond.}$ differs from $W_{Metal}=E_v-E_F$ for the presence of the additional term V_S. Figure 1.2 sketches out the expected energy band diagram of an n-type semiconductor at its surface: on the left-hand side we move into the semiconductor,

while on the right-hand side adsorbates at material surface (Figure 1.2a) have been shown as locally pinned empty/filled levels (A). In this picture, donor levels (E_D) fill the empty levels of A , leading to the building up of a charged region (highlighted in yellow) close to semiconductor surface and to the bonding of the impurity (now charged, A^-).

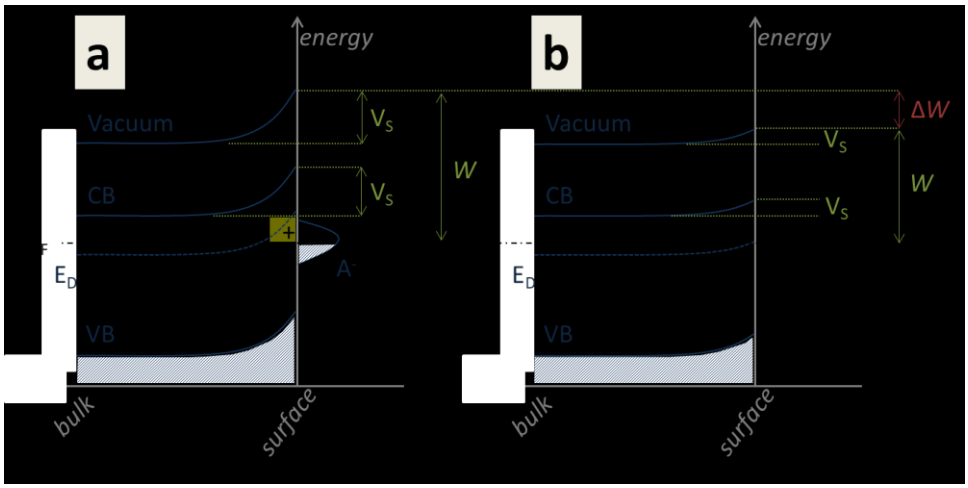

Figure 1. 2 Band structure of a semiconductor close to the surface and its modification (**a**) with and (**b**) without adsorbed charged species.

The local trapping of negative charge in A^- and the appearance of a positive charged layer just above the semiconductor surface introduce an effective pitole at surface[52]. Dipoles, affecting band bending, are responsible for vacuum level upward shift and, in turn, for semiconductor work function increase. When illuminated with UV light with associated photon energy higher than the band gap, an avalanche of photo-generated holes migrates towards the surface along the potential gradient produced by band-bending, discharging the negatively charged adsorbates[53–55]. The freed surface band structure is reported in Figure 1.2 b, where the reduction of the negative adsorbed charges (and, correspondingly, the reduction of the positive charges in the depletion region) results in a lower bending of the potential at the surface, V_s, and thus to a reduction of the work function. Related photo-effects, as photocurrent and photovoltage, ascribed to adsorbed/desorbed species at

semiconductors surface have been extensively investigated in the recent past[54–59]. In general, the desorption process is faster than the adsorption, because at photon energy larger than the band gap, a hole-electron pairs (h-e) plethora is generated; while the adsorption process is driven by different quantity as the *flux* of adsorbates and the *sticking* probability of those at surface, that are deeply related to the partial pressure of gas species (i.e. abundance) in the atmosphere and to the partial coverage of the surface as function of time, respectively.

1.4 Co-substitution

The adsorption of gaseous species at ZnO surface can be reduced with a proper atomic substitution. The idea is to *trap* shallow electrons in lower energy levels, introduced by isovalent atom substitution, in order to reduce the number of bonded adsorbates at surface.

A good candidate for Zn substituting is Co, since it is isovalent to Zn and it has been demonstrated that Co forms Co-V_O complexes, introducing empty electronic levels prone to be filled by free-carriers electrons in *n*-type ZnO[61,62]. Ciatto et al. published a work involving Co-substituting ZnO samples with Co concentration of 2%, 4% and 6%, where the formation of Co-V_O complexes was proved by DFT calculation and x-ray absorption near edge structure (XANES) measurements, showing that the V_O are preferentially located close to Co atoms. In addition to this, a fine analysis of the data proved that the Co-V_O complexes are generally oriented along the *c* axis of the sample and this anisotropy can be addressed to a larger hybridization between Co states involving the *d* orbitals along the *c* axis and the V_O. This is also responsible for major modifications of the electronic structure with respect to substitutional Co which, as anticipated, include the appearance of empty levels[61]. In this context, Di Trolio et al. found a decrease of the conductivity in ZnCoO samples attributed to the presence of levels introduced by Co-V_O complexes. In the same work, the position of the electronic states induced by the Co-V_O complex both when neutral and negatively charged, were calculated, at the level of DFT with on-site Coulomb interaction (DFT+U) description. They are reported in Figure 1.3. Black and red lines correspond to spin-up and spin-down states, respectively. Circles indicate *d*-Co contribution to the electronic levels, as circle radii are proportional to the integral of the corresponding charge densities projected on atom-centered orbitals. The horizontal blue line marks the position of the last occupied eigenvalue. In figure 1.3(a), empty levels induced by neutral Co–V_O are resonant in the conduction band (CB), about 0.5 eV higher than the CBM, while the zero of the energy scale is the VBM. In Fig. 1.3(b), the calculated Co-V_O-induced electronic states get filled by

additional electronic charge, suggesting that the Co-V_O level can indeed be filled by free-carriers introduced in *n*-type ZnO by unintentional shallow donors[61]. Finally, the lowered availability of shallow electrons at ZnCoO surface is expected to reduce the stabilization of adsorbates (see section 1.3).

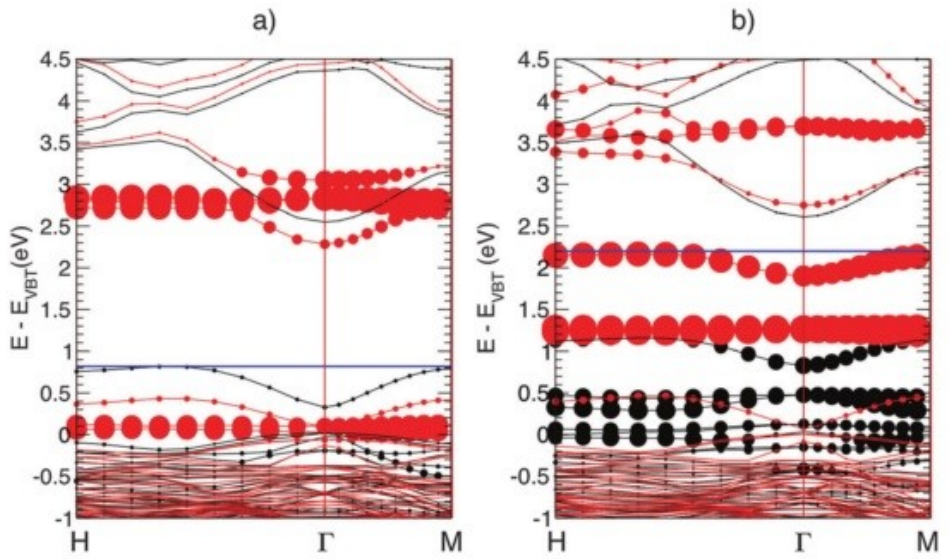

Figure 1. 3 Spin-polarized electronic band structure along the H–Γ–M direction, for the neutral **(a)** and negatively charged **(b)** Co–V_O complex in ZnO[61].

BIBLIOGRAPHY

1. Look, D. C. *et al.* Evidence for native-defect donors in n-type ZnO. *Phys. Rev. Lett.* **95,** 1–4 (2005).

2. Kohan, A. F., Ceder, G., Morgan, D. & Van de Walle, C. G. First-principles study of native point defects in ZnO. *Phys. Rev. B* **61,** 15019–15027 (2000).

3. Nahm, H. H., Park, C. H. & Kim, Y. S. Bistability of hydrogen in ZnO: Origin of doping limit and persistent photoconductivity. *Sci. Rep.* **4,** 1–5 (2014).

4. Walle, C. G. Van De. Hydrogen as a Cause of Doping in Zinc Oxide. *Phys. Rev. Lett.* **85,** 0–3 (2000).

5. Bandopadhyay, K. & Mitra, J. Zn interstitials and O vacancies responsible for n-type ZnO: what do the emission spectra reveal? *RSC Adv.* **5,** 23540–23547 (2015).

6. Look, D. C., Hemsky, J. W. & Sizelove, J. R. Residual native shallow donor in ZnO. *Phys. Rev. Lett.* **82,** 2552–2555 (1999).

7. McCluskey, M. D. & Jokela, S. J. Sources of n-type conductivity in ZnO. *Phys. B Condens. Matter* **401–402,** 355–357 (2007).

8. Janotti, A., Varley, J. B., Lyons, J. L. & Walle, C. G. Van De. Functional Metal Oxide Nanostructures. **149,** (2012).

9. Van de Walle, C. G. Hydrogen as a shallow center in semiconductors and oxides. *Phys. Status Solidi Basic Res.* **235,** 89–95 (2003).

10. Look, D. C. Recent advances in ZnO materials and devices. *Mater. Sci. Eng. B* **80,** 383–387 (2001).

11. Özgür, Ü. *et al.* A comprehensive review of ZnO materials and devices. *J. Appl. Phys.* **98,** 41301 (2005).

12. Janotti, A. & Van de Walle, C. G. Oxygen vacancies in ZnO. *Appl. Phys. Lett.* **87,** 122102 (2005).

13. Janotti, A. & Van de Walle, C. G. New insights into the role of native point defects in ZnO. *J. Cryst. Growth* **287,** 58–65 (2006).

14. Janotti, A. & Van de Walle, C. G. Native point defects in ZnO. *Phys. Rev. B* **76,** 165202 (2007).

15. Park, C. H., Zhang, S. B. & Wei, S.-H. Origin of p -type doping difficulty in ZnO:

The impurity perspective. *Phys. Rev. B* **66,** 73202 (2002).

16. Lee, E.-C. & Chang, K. J. Possible *p* -type doping with group-I elements in ZnO. *Phys. Rev. B* **70,** 115210 (2004).

17. Janotti, A. & Van De Walle, C. G. Fundamentals of zinc oxide as a semiconductor. *Reports Prog. Phys.* **72,** (2009).

18. Minegishi, K. *et al.* Growth of *p*-type Zinc Oxide Films by Chemical Vapor Deposition. *Jpn. J. Appl. Phys.* **36,** L1453–L1455 (1997).

19. Joseph, M., Tabata, H. & Kawai, T. *p*-Type Electrical Conduction in ZnO Thin Films by Ga and N Codoping. *Jpn. J. Appl. Phys.* **38,** L1205–L1207 (1999).

20. Look, D. C. *et al.* Characterization of homoepitaxial *p* -type ZnO grown by molecular beam epitaxy. *Appl. Phys. Lett.* **81,** 1830–1832 (2002).

21. Kim, K.-K., Kim, H.-S., Hwang, D.-K., Lim, J.-H. & Park, S.-J. Realization of *p*-type ZnO thin films via phosphorus doping and thermal activation of the dopant. *Appl. Phys. Lett.* **83,** 63–65 (2003).

22. Ryu, Y. R., Kim, W. J. & White, H. W. Fabrication of homostructural ZnO *p–n* junctions. *J. Cryst. Growth* **219,** 419–422 (2000).

23. Ryu, Y. . *et al.* Synthesis of *p*-type ZnO films. *J. Cryst. Growth* **216,** 330–334 (2000).

24. Xiu, F. X. *et al.* High-mobility Sb-doped *p*-type ZnO by molecular-beam epitaxy. *Appl. Phys. Lett.* **87,** 152101 (2005).

25. Hutson, A. R. Hall Effect Studies of Doped Zinc Oxide Single Crystals. *Phys. Rev.* **108,** 222–230 (1957).

26. Mohanty, G. P. & Azároff, L. V. Electron Density Distributions in ZnO Crystals. *J. Chem. Phys.* **35,** 1268–1270 (1961).

27. Hausmann, A. Ein ?F-Zentrum? als paramagnetischer Donator in Zinkoxid. *Zeitschrift fr Phys.* **237,** 86–97 (1970).

28. Hoffmann, K. & Hahn, D. Electron Spin Resonance of Lattice Defects in Zinc Oxide. *Phys. Status Solidi* **24,** 637–648 (1974).

29. Utsch, B. & Hausmann, A. Halleffekt und Leitf higkeitsmessungen an Zinkoxid-Einkristallen mit Sauerstofflcken als Donatoren. *Zeitschrift fr Phys. B Condens. Matter Quanta* **21,** 27–31 (1975).

30. Hagemark, K. I. Defect structure of Zn-doped ZnO. *J. Solid State Chem.* **16,** 293–299 (1976).

31. Pankove, J. I. & Johnson, N. M. *Hydrogen in Semiconductors, Semiconductors and Semimetals*. (Boston, MA : Academic Press, 1991).

32. Selim, F. A., Weber, M. H., Solodovnikov, D. & Lynn, K. G. Nature of native defects in ZnO. *Phys. Rev. Lett.* **99,** 1–4 (2007).

33. Wei, S.-H. & Zunger, A. Role of metal d states in II-VI semiconductors. *Phys. Rev. B* **37,** 8958–8981 (1988).

34. Schröer, P., Krüger, P. & Pollmann, J. First-principles calculation of the electronic structure of the wurtzite semiconductors ZnO and ZnS. *Phys. Rev. B* **47,** 6971–6980 (1993).

35. Jaffe, J. E., Snyder, J. A., Lin, Z. & Hess, A. C. LDA and GGA calculations for high-pressure phase transitions in ZnO and MgO. *Phys. Rev. B* **62,** 1660–1665 (2000).

36. Zhou, G. C. *et al.* First-principle study on bonding mechanism of ZnO by LDA+U method. *Phys. Lett. A* **368,** 112–116 (2007).

37. Mang, A., Reimann, K. & Rübenacke, S. Band gaps, crystal-field splitting, spin-orbit coupling, and exciton binding energies in ZnO under hydrostatic pressure. *Solid State Commun.* **94,** 251–254 (1995).

38. Hedin, L. New Method for Calculating the One-Particle Green's Function with Application to the Electron-Gas Problem. *Phys. Rev.* **139,** A796–A823 (1965).

39. Preston, A. R. H. *et al.* First-principles calculation of resonant x-ray emission spectra applied to ZnO. *Phys. Rev. B* **83,** 205106 (2011).

40. Fuchs, F., Furthmüller, J., Bechstedt, F., Shishkin, M. & Kresse, G. Quasiparticle band structure based on a generalized Kohn-Sham scheme. *Phys. Rev. B* **76,** 115109 (2007).

41. Shishkin, M. & Kresse, G. Self-consistent GW calculations for semiconductors and insulators. *Phys. Rev. B* **75,** 235102 (2007).

42. King, P. D. C. *et al.* Valence-band electronic structure of CdO, ZnO, and MgO from x-ray photoemission spectroscopy and quasi-particle-corrected density-functional theory calculations. *Phys. Rev. B* **79,** 205205 (2009).

43. Lim, L. Y. *et al.* Angle-resolved photoemission and quasiparticle calculation of ZnO: The need for d band shift in oxide semiconductors. *Phys. Rev. B - Condens. Matter Mater. Phys.* **86,** 1–6 (2012).

44. Girard, R. T. *et al.* Electronic structure of ZnO(0001) studied by angle-resolved photoelectron spectroscopy. *Surf. Sci.* **373,** 409–417 (1997).

45. Kobayashi, M. *et al.* Experimental observation of bulk band dispersions in the oxide semiconductor ZnO using soft x-ray angle-resolved photoemission spectroscopy. *J. Appl. Phys.* **105,** 122403 (2009).

46. Henrich, V. E. & Cox, P. A. *The Surface Science of Metal Oxides*. (Cambridge University Press).

47. Kurtz, M. *et al.* Active Sites on Oxide Surfaces: ZnO-Catalyzed Synthesis of Methanol from CO and H 2. *Angew. Chemie Int. Ed.* **44,** 2790–2794 (2005).

48. Ahn, M. W. *et al.* Gas sensing properties of defect-controlled ZnO-nanowire gas sensor. *Appl. Phys. Lett.* **93,** 1–4 (2008).

49. Sadek, A. Z., Choopun, S., Wlodarski, W., Ippolito, S. J. & Kalantar-zadeh, K. Characterization of ZnO Nanobelt-Based Gas Sensor for H_2NO_2, and Hydrocarbon Sensing. *IEEE Sens. J.* **7,** 919–924 (2007).

50. Lüth, H. *Solid Surfaces, Interfaces and Thin Films*. (2010). doi:10.1007/978-3-642-13592-7

51. Yukawa, R., Ozawa, K., Yamamoto, S., Liu, R.-Y. & Matsuda, I. Anisotropic effective mass approximation model to calculate multiple subband structures at wide-gap semiconductor surfaces: Application to accumulation layers of SrTiO 3 and ZnO. *Surf. Sci.* **641,** 224–230 (2015).

52. Mignolet, J. C. P. On the definition of the pitole moment from the surface potential of a film. **2798,** 122–125 (1955).

53. Wilken, S., Parisi, J. & Borchert, H. Role of oxygen adsorption in nanocrystalline ZnO interfacial layers for polymer-fullerene bulk heterojunction solar cells. *J. Phys. Chem. C* **118,** 19672–19682 (2014).

54. Jin, Y., Wang, J., Sun, B., Blakesley, J. C. & Greenham, N. C. Solution-processed ultraviolet photodetectors based on colloidal ZnO nanoparticles. *Nano Lett.* **8,** 1649–1653 (2008).

55. Dhara, S. & Giri, P. K. Enhanced UV photosensitivity from rapid thermal annealed vertically aligned ZnO nanowires. *Nanoscale Res. Lett.* **6,** 1–8 (2011).

56. Postica, V. *et al.* Morphology dependent UV photoresponse of Sn-doped ZnO microstructures. *Solid State Sci.* **71,** 75–86 (2017).

57. Zakirov, M., Nadtochiy, A. & Korotchenkov, O. Photovoltage decay in sonochemically synthesized ZnO. *YSF 2015 - Int. Young Sci. Forum Appl. Phys.* 2–5 (2015). doi:10.1109/YSF.2015.7333267

58. Kronik, L. & Shapira, Y. Surface photovoltage spectroscopy of semiconductor

structures: At the crossroads of physics, chemistry and electrical engineering. *Surf. Interface Anal.* **31,** 954–965 (2001).

59. Kronik, L. & Shapira, Y. Surface photovoltage phenomena: Theory, experiment, and applications. *Surf. Sci. Rep.* **37,** 1–206 (1999).

60. Ciatto, G. *et al.* Evidence of cobalt-vacancy complexes in Zn1-xCoxO dilute magnetic semiconductors. *Phys. Rev. Lett.* **107,** 1–5 (2011).

61. Di Trolio, A. *et al.* The effect of Co doping on the conductive properties of ferromagnetic $Zn_x Co_{1-x} O$ films. *J. Mater. Chem. C* **3,** 10188–10194 (2015).

2. Materials and Methods

In this chapter we give a brief review of fabrication and characterization techniques used in this work. The first sub-section is dedicated to pulsed laser deposition, by means of which all of the presented samples have been produced. The second subsection concerns scanning probe microscopies and in particular atomic force microscopy. These techniques allowed us to study physical properties (i.e. electric, electrostatic and electro-mechanic) of samples at nano-scale and, in some cases in ultra-high vacuum conditions. The last sub-section describes fundamentals of other techniques, such as scanning electron microscope and X-ray diffraction, used to characterize samples. Finally, each part terminates with a description of our experimental setup, conditions and used parameters.

2.1 Pulsed Laser Deposition

In *pulsed laser deposition* (PLD) technique, or *laser ablation*, a pulsed laser beam is focused on a small region of the bulk material to evaporate (*target*), where the incident photons transfer their energy to the atoms, leading to the evaporation of the material. Evaporated material will be collected on a *substrate*, placed in front of the target. Generally, the laser beam does not perpendicularly hits the target surface, in order to avoid interactions of light with the evaporated material (called *plume* for its typical shape), that emerges normally with respect the surface plane. The energy per unit area (*fluence*) transferred by the laser beam to the target surface, together with laser pulse frequency and the pressure of the PLD chamber influences the *evaporation rate*, i.e. the amount of atoms leaving the target per unit time. On the other hand, the *deposition rate*, i.e. the amount of atoms sitting on the substrate per unit time, is function of the evaporation rate and the temperature of the substrate.
The PLD process has been modelled[1,2] by splitting the fabrication in three phases:

- Laser-target interaction and plasma formation.
- Laser-plasma interaction.
- Plasma expansion.

Laser-Target interaction and plasma formation.

Laser-target interaction and plasma formation are regulated by a previously mentioned parameter, the fluence (or laser beam energy per unit area), that controls the energy transfer from the incident photons to the target atoms. With a low fluence (from 10^{-3} to 10^{-1} J/cm^2) the material evaporates from target, leading to the formation of a "cloud", instead of the plume. This conditions are mainly used for analysing the chemical composition of the target. With a medium fluence (magnitude order of 10^{0} J/cm^2) the evaporating material starts to form the

typical plume shape (Figure 2.1). In this range, the value of the fluence becomes significant for growing good quality samples. By increasing the fluence (above 10^1 J/cm^2), the pulsed laser beam interacts with the evaporating material in a region close to the target surface, causing the ionization of the emerging atoms. Due to a possible ion-electron recombination within the plume, X-ray emissions can occur. For this reason, under controlled conditions, this range of fluence is used as coherent source of X-rays[3].

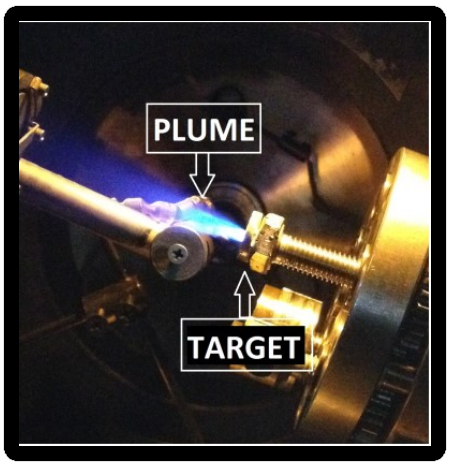

Figure 2. 1 The laser beam (not visible in the picture) hits the target surface, evaporating the material that emerges in a typical shaped *plume*.

Laser-Plasma interactions.

Plume characteristics (temperature, ionization conditions, etc...) depend on both laser-target and laser-plasma interactions. In particular, photons can interact with the plasma causing the typical consequences of light-matter interactions as excitation-ionization effects and temperature increase. All of these processes must be taken into account when dealing with PLD.

Excitation and Ionization

Typical laser wavelength used for PLD (200÷600nm) are not enough to ionize atoms, so that, atoms are generally excited by photons from the laser. However, it is possible to achieve the ionization by means of *multi-photon* processes. The *cross-section* of such processes depends on the number of photons and, in the case of PLD, since the high number of photons (about 10^{26} photons/cm^2) involved, these effects are not negligible.

Thermal Effect

The mean temperature of the plasma depends on a variety of dynamical processes making hard the development of a model. As a consequence, an estimate of the temperature, referred only to the early moments of the laser-target interaction and to the early stage of the laser-plasma interaction, results reasonably around $5x10^4$K [4], by measuring the wavelength of the emitted radiation according to qualitative considerations.

Plasma Expansion

The expansion of the "cloud" of evaporated material starts when the material leaves the target. In general, the dynamic is very complex and the most cited models by *Singh-Narayan*[2,5] and *Kelly-Dieleman*[6,7] will be here discussed. Singh and Narayan divided the plasma expansion process in two phases, dominated by an isothermal and an adiabatic expansion, respectively. At time t (smaller than the pulse time τ_p), the isothermal expansion has the following expression

$$n(\vec{r},t) = N\frac{t}{\tau_p}\frac{1}{X(t)Y(t)Z(t)}e^{-\left[\frac{x^2}{2X(t)}+\frac{y^2}{2Y(t)}+\frac{z^2}{2Z(t)}\right]} \qquad (2.1.1)$$

where N is a normalization coefficient and $X(t)$, $Y(t)$, $Z(t)$ are the plasma fronts at t.

The pressure of the early phase is estimated from the ideal gas law in tens of atmospheres, and $n(\vec{r},t)$ is calculated from Equation 2.1.1. Geometrical

considerations ensure that the plasma fronts X(t), Y(t), Z(t) correspond to a material leaving the surface in a perpendicular direction.

The second phase, the adiabatic expansion, is ruled by

$$T(t)[X(t)Y(t)Z(t)]^{\gamma-1} = const. = T_0[X_0Y_0Z_0]^{\gamma-1} \quad (2.1.2)$$

where $X_0Y_0Z_0$ are the positions of the plasma fronts at the end of the expansion.

The Singh's calculations also provide a quite reliable model for the shape of the plasma.

On the other hand, Kelly-Dieleman's model is focused on the gas-dynamic of the plasma expansion problem. They consider a layer of evaporating material, the so called *Knudsen Layer*, to predict the angle distribution of the material emerging from the surface, that follows a $cos^n(\theta)$ law with $2 \leq n \leq 8$.

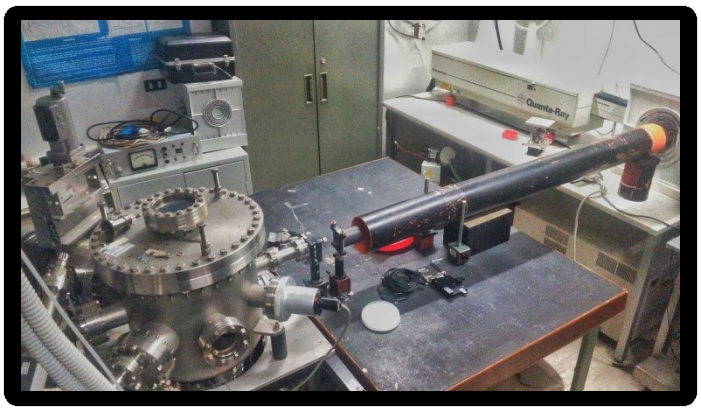

Figure 2. 2 PLD System at ISC-CNR (Rome). The vacuum chamber is visible on the left side of the image, while the laser source is placed on the upper right

Experiment

Sample fabrication has been carried out by means of a PLD equipment at *Istituto dei Sistemi Complessi* of *Consiglio Nazionale delle Ricerche* in Tor Vergata (Rome, IT). Figure 2.2 shows the high vacuum (HV) chamber with laser source on the right side. The chamber is made of austenitic steel, with interstitial intrusion of carbon into the

iron lattice conferring it a high structural resistance and anti-corrosion feature. The desired vacuum pressure (~10^{-6}mbar) is reached by means of a series of *turbo-molecular* and *rotary* pumps and all flanges have been sealed with copper gaskets. On the other hand, a *flux-meter* permits to inlet a controlled quantity of pure (99,99%) O_2 gas, up to reach and maintain a constant deposition pressure.

A solid state laser with Neodymium-doped $Y_3Al_5O_{12}$ crystal (Nd:YAG), fabricated by Spectra-Physics, producing a coherent light with *fundamental* harmonic of wavelength λ_{Fund}=1064nm, has been used as laser source. A commutator group provides the derivation of three consecutive harmonics of 532nm, 355nm and 266nm wavelength, covering a range from infrared to ultra-violet spectrum. In addition to this, it is possible to set the repetition rate (i.e. number of laser pulses per second) and the intensity of the beam, while pulse duration is fixed at 7ns. We fabricated ZnO and $Zn_{0.95}Co_{0.05}O$ (here in after ZnCoO, for simplicity) thin films deposited on p-doped Si substrates. Deposition parameters are summarized in Table 1.

Material	Substrate Temperature (°C)	Pressure (mbar)	Energy per Laser Pulse (mJ)	Deposition Time
ZnO – ZnCoO	500	$1*10^{-5}$ (With O_2 inlet)	100	1’

Table 1. Deposition parameters.

2.2 Scanning Probe Microscopy

An exciting sentence by Richard Feynman, "There is plenty of room at the bottom", pointed out a new direction for science down to a nano-scale world. Indeed, Feynman enlightened the possibility to access and control the physics at the nano-scale facing off with a quantum world but, on the other hand, gaining new "room" for solving problems associated with the continuous development of our modern world. Half a century later, nanotechnology turned up as the only way to solve fundamental problems by combining input from many scientific disciplines, spanning from biology through chemistry and physics to medicine.

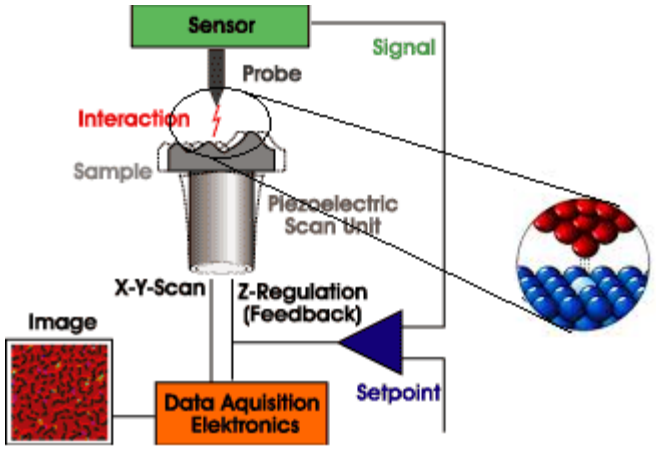

Figure 2. 3 SPM basic setup. The interaction has a functional dependence on probe-sample distance and a feedback system uses the signal acquired from sensor, compared with a setpoint value, to drive a piezo-actuator in order to separate or approach probe to sample, restoring the interaction at the desired setpoint

Tens of years later, during '80s, the invention of Scanning Tunnelling Microscope (STM)[8] and Atomic Force Microscope (AFM)[9] confirmed the futuristic ideas presented by Feynman. Moreover, the abilities of the STM and AFM in imaging and manipulating single atoms as well as investigating physical properties of samples at nano-scale, largely contributed to develop the scientific field of nanotechnologies.

Scanning probe microscopies (SPM) are based on the interaction between a probe and the surface of the specimen. Depending on interaction (tunnelling current for STM, Lennard-Jones' potential for AFM, and so on…), different physical properties of the sample can be investigated. Several investigation techniques have been developed by starting from STM and AFM setup, e.g. Kelvin Probe Force Microscopy (KPFM), Conductive AFM (C-AFM) and Piezo-response Force Microscopy (PFM).

The basic experimental setup of a SPM system (Figure 2.3) consists of a nano-metric accurate scanning unit (a piezoelectric tube in the largest part of the equipment), a signal acquisition unit, a feedback circuit and a probe. Since interactions are strictly dependent on probe-sample (P-S) distance (*z* direction), the feedback system is used to keep constant P-S interaction by varying their mutual distance. The actuation of the movement along the *z* direction is demanded to the piezo-tube. In addition to this, the tube actuates the *x-y* movements, related to the raster scan of the sample surface.

In the following subsections we will explain in more detail how this general setup can be adapted to investigate the physical properties we deal with into this thesis. Anyway, a complete dissertation on SPM techniques can be found elsewhere[10].

Atomic Force Microscopy.

During last twenty years, many AFM-based techniques have been developed dealing with different P-S interactions. So that, recorded signals are related to several physical properties investigated with nano-metric resolution. Despite this variety, the fundamental interaction for the AFM is driven by the Lennard-Jones' (L-J) potential, as shown in Figure 2.4. The interaction force F_{int} is function of the separation distance z_t between the probe apex and the sample surface and can assume both positive (repulsive P-S force) and negative (attractive P-S force) values. The whole F_{int} graph can be divided into three zones:

- **Attractive Force only.** Starting from infinite z_t and approaching to P-S contact, the interaction is dominated by a genuine Van der Waals' force leading the probe to deflect towards the surface.

- **Turning zone.** Both attractive and repulsive forces contribute to the interaction. In this zone, the two kind of forces reach the equilibrium point. Moreover, the distance between the minimum of the potential and this equilibrium point is equal to the inter-molecular (P-S) distance a_0.
- **Repulsive Force only.** Starting from the "full-contact" point, i.e. the equilibrium point, this regime is dominated by a chemical-like potential leading to a P-S separation force.

It is possible to distinguish among three different operation modes, depending on the kind of force: *Non-contact, Tapping* and *Contact*, respectively. The basic SPM setup described in the previous subsection is adapted for the AFM (Figure 2.5) by using a laser-photodiode system to read the P-S interaction as cantilever deflection. Indeed, the probe for an AFM is a cantilever with a sharp tip (ideally ending with a single atom), able to deflect under the F_{int}. In detail, at any point of the raster *x-y* scan, the cantilever is deflected upward or downward for a certain amount under the interaction of the tip with the surface, depending on the local height of the sample.

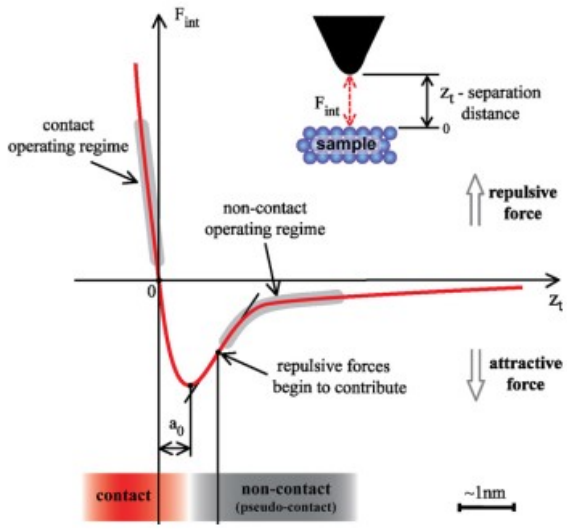

Figure 2. 4 Interaction potential sketch of AFM working modes.

Contact mode.

A very simple way how to operate the AFM is the contact mode, where the cantilever is held in permanent contact with the sample, i.e. repulsive regime. Some advantages of the contact operation are related to the possibility to recover information about friction[11], elasticity[12] and many other mechanical properties of the material under investigation at nano-metric scale[13]. Moreover, the model describing the deflection of the lever is a simple spring-like model leading to a good control of the probe pressure on the surface.

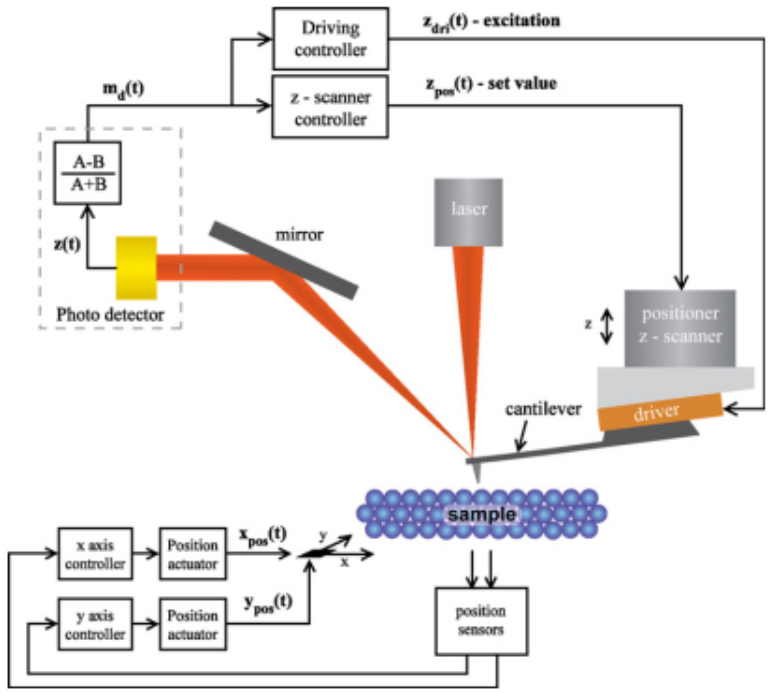

Figure 2. 5 General setup used for AFM and derived techniques. In this case a piezo-tube under the sample provides the raster scanner, while *z-scan* is effectuated by another piezo actuator behind the tip-holder. In brown, an optional piezo plate is mounted behind the probe in order to provide the cantilever oscillation in *alternate contact* and *non-contact* modes. Sensing equipment is composite by a laser-photodiode system, able to measure the cantilever deflection.

However, it is not recommended to use the contact mode when dealing with soft samples as the probe can scratch or destroy the surface.

Non-contact mode.

Contrary to contact mode, also known as *static* mode since the cantilever is kept at the same deflection value from the feedback system, the *non-contact* is a *dynamic* operation mode. The cantilever is kept far from the surface and it is oscillating at certain frequency (generally close to the resonance frequency f_0) excited by a piezo-plate. As the probe approaches the surface, while oscillating, the frequency shifts under the P-S interaction. In this case, the AFM is working into the first part of the L-J's potential, so that the interaction is exclusively attractive. The great advantage of this technique is the possibility to work with soft samples since the tip scans the surface without scratching it, but unfortunately, the non-contact is only possible when in ultra-high vacuum, in order to have a genuine resonance of the cantilever.

Tapping mode.

In *tapping* mode the probe alternatively hits the surface, as the name suggests, and the AFM system is working into the *turning* regime, alternatively moving from repulsive to attractive forces. A piezo-plate provides the excitation, forcing the cantilever to oscillate, as for *non-contact* mode, but, instead of the frequency, the system monitors the amplitude of the oscillation. When far from the sample surface, the free-oscillation amplitude is recorded as reference amplitude. Then, as the P-S distance is reduced, the probe interacts repulsively and attractively during the operation cycle and the amplitude of the oscillation is reduced or increased, respectively. The feedback system acts on the piezo-tube in order to work with a fixed value of the amplitude, generally the 75% of the free-oscillation amplitude.
By using tapping mode it is possible to investigate both hard and soft samples. Moreover, it is a skilled technique to study cells or living samples by carrying out *in-liquid* experiments. On the other hand, this mode is problematic when a quantitative study of the interaction between probe and sample is needed, since the amplitude modulation is not easily related to the interaction.

AFM-based Techniques.

Kelvin Probe Force Microscopy.

KPFM is an AFM-based technique that measures the contact potential difference (V_{CPD}) between a conducting probe and the sample surface[14]. Starting from V_{CPD}, it is possible to calculate the *work function* (W) of the sample with high spatial resolution.

Indeed, this technique has been widely used to study electronic properties of metals[15], semiconductors[16] as well as organic semiconductors[17] and it has been used to develop biosensor devices able to recognize molecular interactions[18]. V_{CPD} is defined as:

$$V_{CPD} = \frac{W_{tip} - W_{sample}}{e} \tag{2.2.1}$$

where W_{tip} and W_{sample} are the work functions of tip and sample and e is the electronic charge.

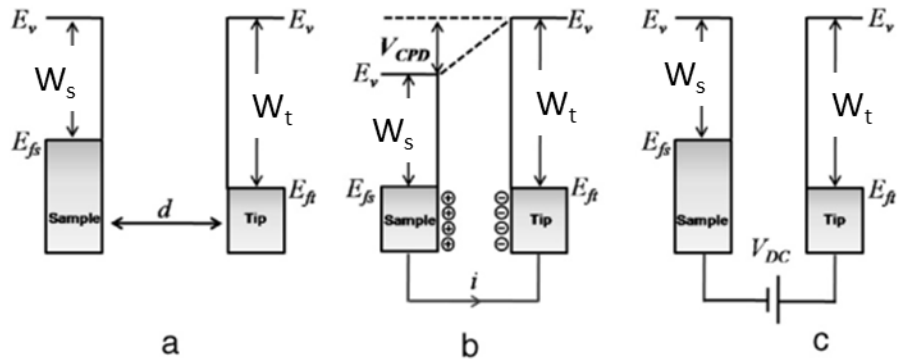

Figure 2. 6 Electronic energy levels for (**a**) probe and sample separated of a distance *d*, (**b**) probe and samples in electrical contact with a current *I* flowing to equilibrate Fermi levels, (**c**) probe and sample when a DC bias is applied in order to nullify V_{CPD}.

Figure 2.6 sketches the energy level for tip and sample when not in contact (2.6a), in contact (2.6b) and an external bias is applied in order to nullify the V_{CPD} (2.6c).

When the tip is brought close to the contact with the sample surface, an electrostatic force is generated due to the differences in their Fermi levels. In this case, the E_vs are aligned but not the Fermi levels (Figure 2.6a). Equilibrium is reached when a current can flow between tip and sample to level the Fermi energies, as P-S are in contact or close enough for tunnelling current (Figure 2.6b). So that, a V_{CPD} will form and an electrical force acts on the contact area. To nullify this force, it is possible to apply a DC voltage (V_{DC}) in order to align the vacuum levels (Figure 2.6c). The amount V_{DC} is equal to the work function difference between the tip and the sample and, once W_{tip} is known, it is possible to recover W_{sample} from Eq. 2.2.1. By applying an AC voltage (V_{AC}) plus V_{DC} to the AFM tip, the probe starts to oscillate under an electrostatic force F_{es}:

$$F_{es}(z) = -\frac{1}{2}\Delta V^2 \frac{dC(z)}{dz} \tag{2.2.2}$$

where z is the direction normal to the sample surface, dC/dz is the gradient of the capacitance between P-S and

$$\Delta V = (V_{DC} \pm V_{CPD}) + V_{AC}\sin(\omega t) \tag{2.2.3}$$

The sign ± depends whether the bias is applied to the sample (+) or the tip (-). By substituting Eq. (2.2.3) in Eq. (2.2.2) it is possible to obtain the expression of the electrostatic force acting on the AFM probe:

$$F_{es}(z,t) = -\frac{1}{2}\frac{\partial C(z)}{\partial z}[(V_{DC} \pm V_{CPD}) + V_{AC}\sin(\omega t)]^2 \tag{2.2.4}$$

This equation can be divided into three terms:

$$F_{DC} = -\frac{\partial C(z)}{\partial z}\left[\frac{1}{2}(V_{DC} \pm V_{CPD})\right]^2 \tag{2.2.5}$$

$$F_{\omega} = -\frac{\partial C(z)}{\partial z}(V_{DC} \pm V_{CPD})V_{AC}\sin(\omega t) \tag{2.2.6}$$

$$F_{2\omega} = \frac{\partial C(z)}{\partial z}\frac{1}{4}{V_{AC}}^2\,[\cos(2\omega t) - 1] \qquad (2.2.7)$$

F_{DC} results in a static deflection of the cantilever, F_ω is actually used to measure the V_{CPD} and $F_{2\omega}$ is used in scanning capacitance microscopy[10].

In particular, Eq. (2.2.6) is used to measure V_{CPD} in KPFM. A lock-in amplifier measures the oscillation of the probe under F_ω at the frequency of V_{AC} and a feedback system sets V_{DC} so that the electrostatic oscillation is nullified, i.e. the electrostatic force is zero. This implies that $V_{DC} = V_{CPD}$ and, once W_{tip} is known, by substituting V_{DC} into Eq. (2.2.1), it is possible to calculate W_{sample}.

Conductive AFM.

Conductive AFM (C-AFM) is a technique that simultaneously acquire the topography of the specimen surface and the electric current flowing at the P-S contact point. It was first introduced by Murrel in 1993[19] to study local electrical properties of conductive materials with nano-metric resolution. Conductive probe is brought in contact with sample and two different modes are available:

- **Open Loop operation.** A DC bias is applied between P-S and the system acquires the current flowing through the contact point.
- **Closed Loop operation.** A current setpoint is settled before starting the acquisition. During the scan, a feedback system applies a DC bias between tip and sample in order to recover the current setpoint.

Together with mapping modes, a *spectroscopic* mode is also available. The probe is steady in a point, in contact with the surface, and a bias voltage is swept, allowing the acquisition of current-voltage curves.

Piezoresponse Force Microscopy

PFM uses a standard SPM operated in contact mode with an additional oscillating voltage applied to the conductive tip. The voltage-induced deformations of the

sample lead to periodic vibrations of the sample surface which are transmitted to the tip. The resulting oscillations of the cantilever are sensitively read out with the help of a lock-in amplifier. PFM is generally applied to the investigation of ferroelectric domain patterns, since ferro-electricity entails piezoelectricity and the domain pattern can be visualized by its piezo-mechanical deformation under the application of an electric field. In the case of PFM the electric field is applied locally to the sample to the area under the tip. For standard PFM operation the frequency f of the alternating voltage is set to values of $f \approx$ 10-100 kHz and amplitude typically to $V \approx$ 0.5-10 V.

Scanning Tunneling Microscopy.

In a STM the fundamental interaction is the tunnelling current. Indeed, a metallic tip is kept at nano-metric distance from the sample surface and, in these conditions, there is a finite probability for the electrons of the tip to pass through the vacuum barrier in between and reach the sample (or vice versa), due to the quantum mechanics *tunnel effect*. The tunnelling current is exponentially dependent on P-S distance, which gives rise to a sub-Å resolution in the z-direction. This dependence is described by the electronic wave-function inside the barrier:

$$\Psi(z) = \Psi(0)\, e^{-k\, z} \text{ with } k = \frac{\sqrt{2m(\Phi - eV)}}{\hbar} \qquad (2.2.8)$$

where z is the P-S distance (the tunnelling barrier), Φ is the height of the barrier and eV is the electron energy supplied by the applied bias voltage. So that, the probability for a single electron to tunnel is:

$$|\Psi(z)|^2 = |\Psi(0)|^2 e^{-2\, k\, z} \qquad (2.2.9)$$

with a net tunnel current proportional to the electron occupation in the region (E_F-eV)$\div E_F$:

$$I(z) \propto \sum_{E_{n=E_F-eV}}^{E_F} |\Psi_n(0)|^2 e^{-2kz} \propto I(0) \quad ^{-2kz} \qquad (2.2.10)$$

Once Φ has been fixed, a 1 Å change in tip-sample separation results in a change of the tunnelling current of an order of magnitude. A feedback system is used to keep the tunnel current constant by varying the P-S separation acting on the piezo-tube (this is the so called *constant current mode*). So that, a morphological map of the sample surface is acquired.

Together with map acquisition at very high spatial resolution (up to atomic), it is possible to perform scanning tunnelling spectroscopy (STS) investigations. In general, the tunnel effect for an electron moving from probe to sample is allowed only if void electron states are available at the sample surface. Indeed, once the P-S is fixed, by keeping the probe steady above the sample surface and varying the bias voltage it is possible to acquire the tunnelling current at that point that is proportional to the electronic density of states of the sample.

Experiment

AFM and AFM-based measurements at ambient pressure were performed by using a Bruker Multimode AFM (Figure 2.7), with Nanoscope V controller, installed at *SPNM Lab* of the Physics Department – University of Salerno. The equipment was settled in a Plexiglas box, in order to achieve a good acoustic insulation, with the possibility to completely obscure it and inlet N_2 gas. C-AFM measurements have been carried out by extending the AFM with a current pre-amplifier connected to the probe.

Ultra high vacuum (UHV) measurements have been carried out by means of Omicron "RT-AFM/STM" system (Figure 2.8). Samples can be loaded into the measurement chamber via a load-lock in order to preserve the UHV ($P<10^{-9}$ mbar). For each investigation a proper probe has been chosen among several type, different for mechanical, conductive and constitutive properties. For C-AFM, a conductive Pt bulk probe (Bruker RMN) with resonance frequency of 9kHz, elastic constant of 0.3N/m and an apex radius lower than 20nm has been chosen. The solid Pt tip was chosen instead of a platinum coated Si one to ensure the stability of the material

during conductive measurements (i.e. the raster scanning can easily wear out the coating from Si).

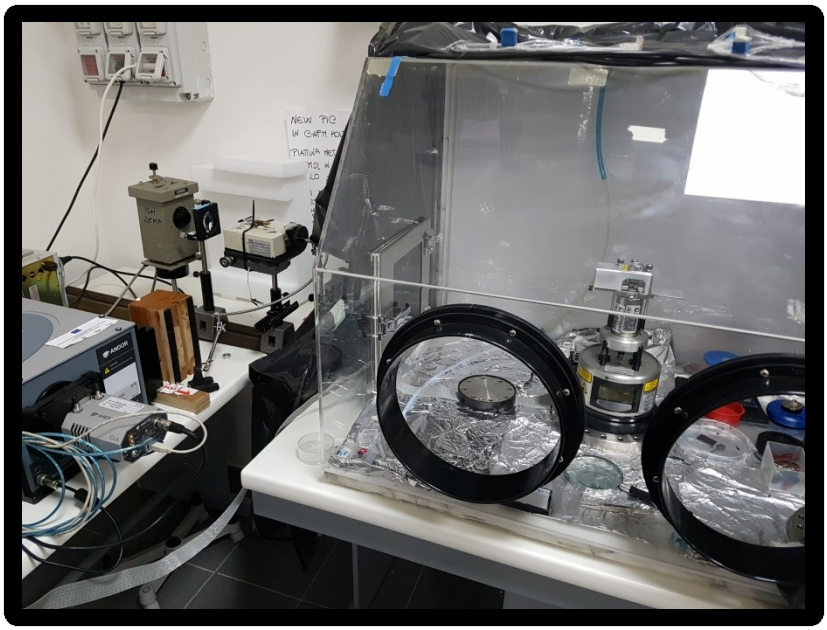

Figure 2. 7 Bruker AFM into its acoustic box with UV equipment on the left side.

To establish a good conductive contact between probe and sample surface, a normal force of 1.4μN has been applied to the cantilever for both maps and I(V) data acquisition. On the other hand, the values of bias voltage used during map acquisition never exceeded few hundreds of mV, in order to avoid electrostatic force acting on cantilever (leading to an increase of the normal on the probe) with a change of the contact force and in the extreme case the change in the contact area due to tip-sample deformations. KPFM experiments required a second raster scan of the surface at certain constant height, after topographic data have been acquired. In this case, topography has been measured in alternate contact AFM with a Pt coated probe with nominal resonance frequency of 80kHz and spring constant of 3N/m (SCM-PIT by Bruker). The second scan height, or *lift mode*, was fixed at 110nm in order to avoid any signal cross-talk between Van der Waal's and electrostatic forces. Moreover, to assure the complete disengagement of the probe from surface,

nullifying Van der Waal's interaction, a first 150nm lift of the probe was executed by the system at any lift mode measurement point. Finally, a V_{AC}=500mV with ω close to the resonance frequency of the lever was settled between probe and sample to acquire KPFM maps with an improved noise/signal ratio.

PFM was performed on all of the fabricated samples to investigate electro-mechanic properties, by mounting Pt coated probe, with resonance frequency of 9kHz and spring constant of 0.3N/m (SCM-PIC Bruker). A contact force of 10nN was established and kept constant during measurements in order to assure the mechanical contact between tip and surface. For each sample, before starting measurements, the characteristic resonance frequency (*contact frequency*) of the P-S system was acquired together with relative Q-factor. Then, PFM was performed by establishing a V_{AC} between probe and sample at that contact frequency, with the aim to maximize the piezoelectric-response of the sample and exploiting the highest sensitivity of the probe. Q-factor was also useful to recover quantitative information from PFM maps. Indeed, by using $d_{33} = \frac{Amplitude\ [nm]}{V_{AC}[V]\ Q}$ it has been possible to calculate the d_{33} coefficient of materials from acquired amplitude maps.

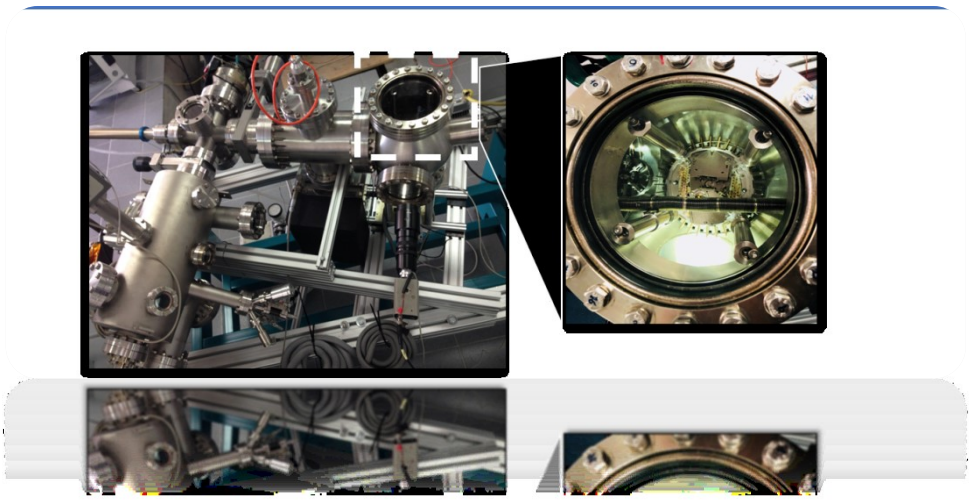

Figure 2. 8 UHV Omicron "RT-AFM/STM" system.

2.3 Other Techniques

Scanning Electron Microscope, Field Emission Scanning Electron Microscope and Energy Dispersive Spectroscopy

Scanning electron microscope (SEM) is a non-optical microscopy based on the interaction of an electron beam with a conductive material. A raster scan of the sample is performed and, for each point of the scan, the electrons knocked out or backscattered from the sample are collected and the acquisition system produces the image of the surface. SEM was developed from transmission electron microscope (TEM) in the first part of 1900's. However, really efficient SEM was only produced in 1952 as a result of the great effort of McMullan (University of Cambridge)[20]. Theoretical resolution limit of an electron microscope is defined by wave theory and depends on the wavelength of the electromagnetic radiation used to make the observation. So that, for a 100keV beam energy, the corresponding wavelength is 0.050 Å, leading to a resolution of 0.025 Å.

Practical resolution, however, is affected by experimental factors that reduce the resolution as diffraction, astigmation and chromatic aberration. Schematic representation of a SEM equipment is given in Figure 2.9: electrons are generated from a tungsten wire, as cathode, and are accelerated beyond the anode; a system of electronic lenses focuses and deflects the beam to perform the raster scan. SEM chamber is under high vacuum, with an augmented mean free path of electrons. Because of its great depth of field, materials with rough topography are particularly well suited for SEM investigation. Indeed, secondary electrons leave the sample with low energy (less than 50 eV) and are collected by the detector while their path is deflected by the positive potential arising from the anode. The secondary electrons have also two fundamental characteristics that have to be taken into account.

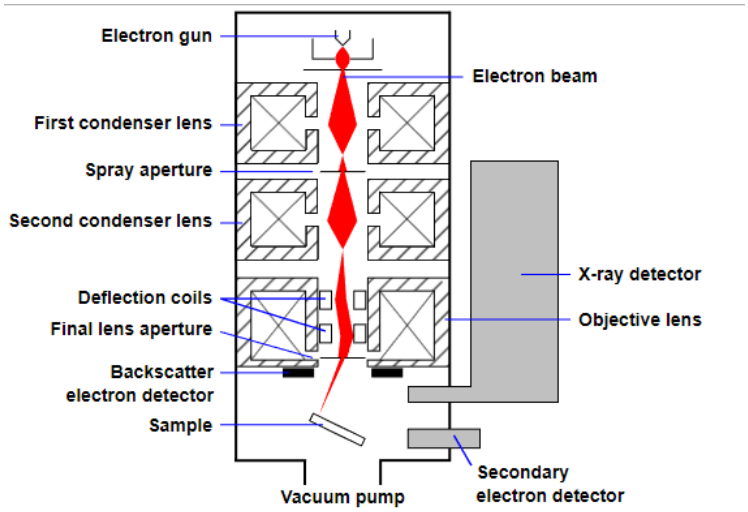

Figure 2. 9 General SEM setup. An electron beam is generated by a filament for thermo-electric emission. Then electrons are accelerated and collimated by electron lenses. Finally the beam is deflected in order to perform the raster scan. A SEM can be equipped by different detectors for several acquisition modes.

First, only secondaries arising at the specimen surface contribute to the image buildup; those arising below the surface alter the contrast. Second, secondary electrons show little response to variation in electron density of the surface material.

One of the great advantages of SEM lies in its extremely simplified specimen preparation techniques. However, it is possible to perform measurements only on conductive sample and, for insulating specimens it is mandatory to metallize the surface.

As described, electrons are generated by thermionic emission from a tungsten wire, whereas in the case of the field emission SEM (FESEM) a very focused electron beam is generated by field emission effect from a tip shaped wire. Compared to SEM, FESEM produces clearer, less electrostatically distorted images, with spatial resolution down to 0.5 nm.

By fruiting of the X-rays generated by the electron beam/surface interaction, it is possible to acquire other information on the sample along with the topography.

Indeed, scattered X-rays are characteristic of the elements forming the material under investigation and they can be detected by wavelength or energy. The energy dispersive spectrometers (EDS) are the most common type of detectors. In this case, a semiconducting Li-doped Si plate is placed between the two electrodes and powered with a voltage of 1kV. As a photon hits the semiconductor, a certain number of hole-electron pairs is generated for photo-electric adsorption. The energy of the incident photon is calculated as the number of photo-generated charge carriers divided by the energy needed to generate a single pair. Finally, a counter registers the number of incoming photons at any energy, building up the EDS spectrum.

X-Ray Diffraction

In crystallography, X-ray diffraction (XRD) is a technique used for determining the atomic structure of a crystal[21]. Diffraction occurs due to the atomic regular distribution in the crystal and, by measuring angles and intensities of the diffracted beams, it is possible to produce a three-dimensional picture of the density of electrons within the crystal. From this electron density, the mean positions of the atoms in the crystal can be determined, as well as their chemical bonds and other information. Not only metals[22] and minerals[23] can form crystals but also inorganic and biological molecules, so that XRD has become widely used in studying vitamins[24], drugs[25], proteins[26], DNA[27,28] and polymers[28,29].

The basic XRD equipment consist of a X-ray source, a goniometer where the sample is mounted on and a detector. A focused monochromatic X-ray beam illuminates the specimen mounted on the goniometer at different orientation, i.e. different incident

angle, of the beam with respect the crystal.

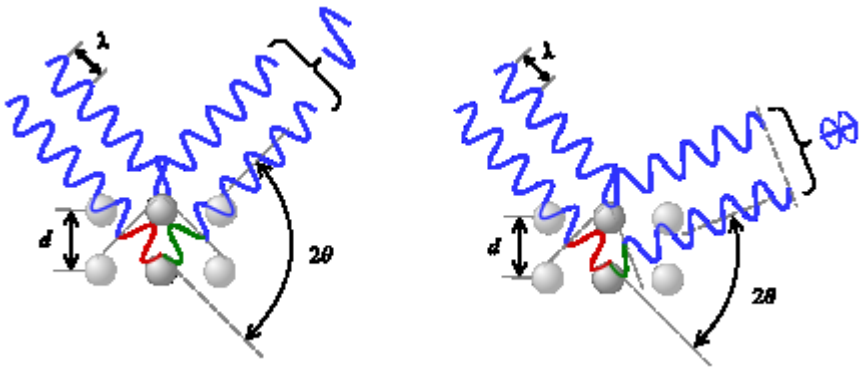

Figure 2. 10 Bragg's law.

As the sample rotates, previous reflections disappear and new ones appear. The intensity of every spot is recorded at any orientation of the crystal on the goniometer by the detector.

Figure 2. 11 XRD and FESEM equipment installed at MUSA lab of SPIN-CNR (U.O.S. Salerno) on the left- and right-side, respectively.

Sometimes, especially when dealing with organic and biological molecules, a 3-D reconstruction of the molecule is needed, by mean mathematic data processing. XRD is based on Bragg's model of diffraction where at certain specific wavelengths (λ) and incident angles (θ), crystals produce intense peak of reflected radiation

(Figure 2.10). This leads to Bragg's law[30], describing the conditions on λ and θ for having a constructive interference:

$$2d\sin(\theta) = n\lambda$$

with *n* a positive integer.

In an XRD experiment, the sample rotates of an angle θ, while the detector can either moves of an angle 2θ or can be kept fix. In the latter case, the intensity of the reflected beam as a function of θ rotation angle gives information on the mosaicity of the sample (i.e. the spread of crystal plane orientations). This technique is also called ω-scan.

BIBLIOGRAPHY

1. Singh, R. & Narayan, J. ,. *Mat. Sci. Eng.* **3,** 217 (1989).

2. Singh, R., Holland, O. W. & Narayan, J. ,. *J. Appl. Phys.* **68,** 233 (1990).

3. Murmane, M. M., Kapteyn, H. C., Rosen, M. D. & Falcone, R. W. ,. *Science (80-.).* **251,** 531 (1991).

4. Zel'dovich, Y. B. & Raizer, Y. P. *Physics of Shock Waves and High Temperature Hydrodynamic Phenomena*. (1966).

5. Singh, R. & Narayan, J. ,. *Phys. Rev. B* **41,** 8843 (1990).

6. Kelly, R. & Miotello, A. Pulsed-laser sputtering of atoms and molecules. Part I: Basic solutions for gas-dynamic effects. *Appl. Phys. B Photophysics Laser Chem.* **57,** 145–158 (1993).

7. Kools, J. C. S., van de Riet, E. & Dieleman, J. A simple formalism for the prediction of angular distributions in laser ablation deposition. *Appl. Surf. Sci.* **69,** 133–139 (1993).

8. Binnig, G. & Rohrer, H. Scanning tunneling microscopy. *Surf. Sci.* **126,** 236–244 (1983).

9. Binnig, G., Quate, C. F. & Gerber, C. Atomic Force Microscopy. *Phys. Rev. Lett.* **56,** 930–933 (1986).

10. Kalinin, S. V. & Gruverman, A. *Scanning Probe Microscopy*. (Springer, 2007).

11. Meyer, G. & Amer, N. M. Simultaneous measurement of lateral and

normal forces with an optical-beam deflection atomic force microscope. *Appl. Phys. Lett.* **57,** (1988).

12. Jarvis, S. P., Yamada, H., Yamamoto, S. I., Tokumoto, H. & Pethica, J. B. Direct mechanical measurement of interatomic potentials. *Nature* **384,** (1996).

13. Giessibl, F. J., Hembacher, S., Bielefeld, H. & Mannhart, J. Subatomic features on the silicon (111)-(7x7) surface observed by atomic force microscopy. *Science (80-.).* **289,** (2000).

14. Sadewasser, S. & Glatzel, T. *Kelvin Probe Force Microscopy*. (Springer Series in Surface Sciences, 2012).

15. Lü, J. *et al.* Kelvin probe force microscopy on surfaces: investigation of the surface potential of self-assembled monolayers on gold. *Langmuir* **15,** 8184–8188 (1999).

16. Polak, L. & Wijngaarden, R. J. Two competing interpretations of Kelvin probe force microscopy on semiconductors put to test. *Phys. Rev. B* **93,** (2016).

17. Huang, H., Wang, H., Zhang, J. & Yan, D. Surface potential images of polycrystalline organic semiconductors obtained by Kelvin probe force microscopy. *Appl. Phys. A Mater. Sci. Process.* **95,** 125–130 (2009).

18. Lee, H., Lee, W., Lee, J. H. & Yoon, D. S. Surface potential analysis of nanoscale biomaterials and devices using Kelvin probe force microscopy. *J. Nanomater.* **2016,** (2016).

19. Murrell, M. P. *et al.* Spatially resolved electrical measurements of SiO

2 gate oxides using atomic force microscopy. *Appl. Phys. Lett.* **62,** 786–788 (1993).

20. Collett, B. M. Scanning electron microscopy: A review and report of research in wood science. *Wood Fiber Sci.* **2,** 113–133 (1970).

21. Ryland, A. L. X-ray diffraction. *J. Chem. Educ.* **35,** 80 (1958).

22. Flinn, P. A. & Chiang, C. X-ray diffraction determination of the effect of various passivations on stress in metal films and patterned lines. *J. Appl. Phys.* **67,** 2927–2931 (1990).

23. Moore, D. M. & Reynolds, R. C. *No Title*. (1989).

24. Hvoslef, J. The crystal structure of L-ascorbic acid, `vitamin C'. I. The X-ray analysis. *Acta Crystallogr. Sect. B Struct. Crystallogr. Cryst. Chem.* **24,** 23–35 (1968).

25. Waugh, K. M. *et al.* Synthesis and Characterization of Selected Heteroarotinoids. Pharmacological Activity as Assessed in Vitamin A Deficient Hamster Tracheal Organ Cultures. Single-Crystal X-ray Diffraction Analysis of 4,4-Dimethylthiochroman-6-yl Methyl Ketone 1,1-Dioxide a. *J. Med. Chem.* **28,** 116–124 (1985).

26. Zimmerman, S. B. & Pheiffer, B. H. A RNA.DNA hybrid that can adopt two conformations: an x-ray diffraction study of poly(rA).poly(dT) in concentrated solution or in fibers. *PNAS* **78,** 78–82

27. Schellman, J. A. & Parthasarathy, N. X-ray diffraction studies on cation-collapsed DNA. *J. Mol. Biol.* **175,** 313–329 (1984).

28. Arnott, S. & Hukins, D. W. L. Refinement of the structure of B-DNA and

implications for the analysis of X-ray diffraction data from fibers of biopolymers. *J. Mol. Biol.* **81,** 93–105 (1973).

29. Morgan, A. B. & Gilman, J. W. Characterization of polymer-layered silicate (clay) nanocomposites by transmission electron microscopy and X-ray diffraction: A comparative study. *J. Appl. Polym. Sci.* **87,** 1329–1338 (2003).

30. Bragg, W. H. & Bragg, W. L. The Reflection of X-rays by Crystals. *Proc. R. Soc. A Math. Phys. Eng. Sci.* **88,** 428–438 (1913).

3. RESULTS AND DISCUSSION

3.1 Introduction

In this chapter the results of scanning probe microscopy experiments on different ZnO-based materials (pure ZnO and Co-substituted $Zn_{1-x}Co_xO$ (namely ZnCoO), with nominal x=0.05) will be presented. The first part will be focused on structural (XRD and EDS) and morphological sample characterization (FESEM and AFM), aiming at showing the high quality of fabricated specimens, checking their thickness as well as the substitution percentage and spatial homogeneity. The second part will be dedicated to C-AFM, electrostatic force microscopy (EFM) and KPFM experiments performed in dark and under monochromatic-UV irradiation, aiming at studying how Co-substitution affects the reactivity of ZnO surface. The third part will be dedicated to electro-mechanical and charge-storing properties of pure and Co-substituted ZnO, of great interest for micro-electro-mechanical systems (MEMS) and energy fields. Finally, a discussion section will end each part.

3.2 Structural and morphological characterizations

Introduction.

ZnO and ZnCoO thin films (nominal 50 nm in thickness), deposited by PLD on *p*-type Si, were characterized by XRD, EDS, FESEM and AFM in order to check the crystalline growth, chemical composition as well as sample morphology. The fabrication process has been optimized by measuring XRD spectra, in order to minimize the full-width-half-maximum (FWHM) of the (002) peak in the ω-scan. On the other hand, EDS spectra have been used to control the dilution of Co into Co-substituted samples. Finally, sample morphology has been investigated by means of AFM and FESEM, aiming at getting a complete characterization of morphology, roughness and thickness of such films.

X-Ray diffraction and electron-dispersive spectroscopy of ZnO and ZnCoO thin films.

X-Ray diffraction spectra and ω-scans were acquired by means of Phillips "X'Pert" High-resolution diffractometer, by using the Cu Kα line (λ = 1.5418 Å), whereas electron dispersive spectra were acquired by means of a "LEO-EVO 50" SEM by Zeiss, equipped with EDS analyzer; the XRD and EDS results are summarized in Figure 3.1 for ZnO, in black, and ZnCoO, in red, respectively. Figure 3.1a shows the XRD pattern of both ZnO and ZnCoO, proving the crystalline growth of both materials: the (002) and (004) peaks dominate the spectra at 2θ=34° and 72°, along with Si peak at 2θ=69° (coming from the substrate). However, the comparison of the ω-scan spectra (Figure 3.1b), around (002) ZnO peak, highlights a wider FWHM in

Co-substituted sample (4.49°), with respect to pure ZnO (3.28°), meaning that a higher spread of crystal plane orientation is present in ZnCoO.

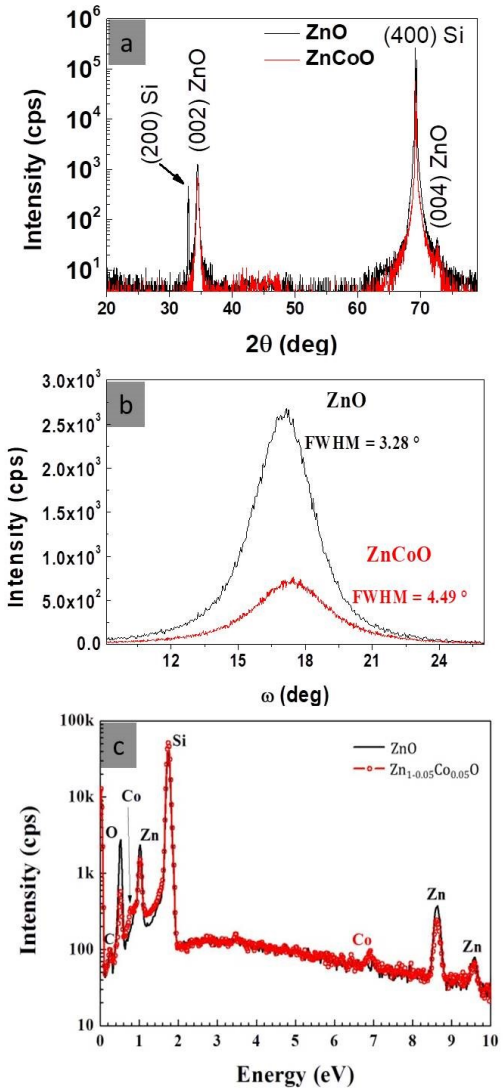

Figure 3. 1 a XRD pattern for ZnO (in black) and ZnCoO (in red). **b** ω-scan around (002) ZnO peak. **c** EDS analysis for ZnO (in black) and ZnCoO (in red) samples.

Figure 3.1c presents EDS spectra of the pure (black) and Co-substituted (red) material, acquired on 2mm × 1mm area. As expected, Zn, O and Si peaks are always present, whereas Co is revealed only in the ZnCoO sample. The evaluation of Co content have been obtained by averaging 50 different areas (2mm x 1mm in lateral size), resulting in a Co/Zn ratio of 5% (±0.5%), which corresponds to the nominal composition (5%). A small C contamination was measured on both samples, addressed to the exposure of sample surface to the ambient atmosphere.

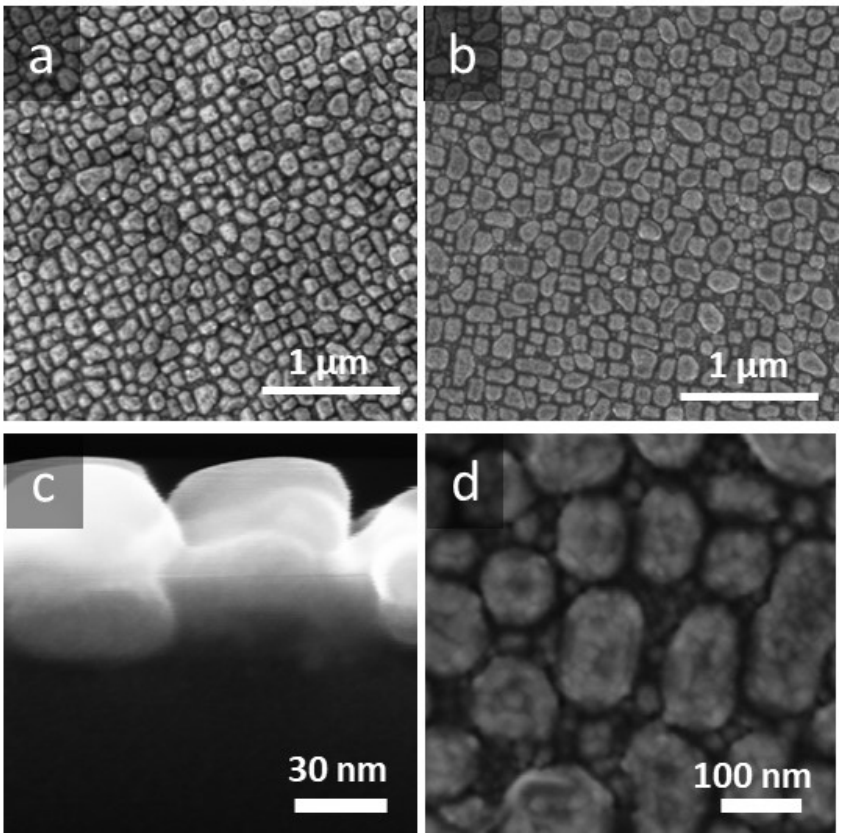

Figure 3. 2 Topography of (**a**) ZnO and (**b**) ZnCoO acquired by means of FESEM, on 3µm x 3µm scan area. Both pure and Co-substituted ZnO show a granular morphology with grain lateral size ranging from 50 to 200 nm. **c** Transversal FESEM imaging of the ZnO sample. The

brighter area is the ZnO film, whereas the beneath darker area is the Si substrate. **d** Close-up of the ZnCoO surface.

Surface morphology and thickness measurements.

Sample topographies presented in this section have been acquired by means of AFM "MultiMode V" by VEECO in tapping mode, by using a SCM-PIT probe (Si tip coated with PtIr, cantilever resonance frequency of 80 kHz and spring constant 3N/m) by Bruker, and FESEM "Σigma Gemini" by Zeiss.

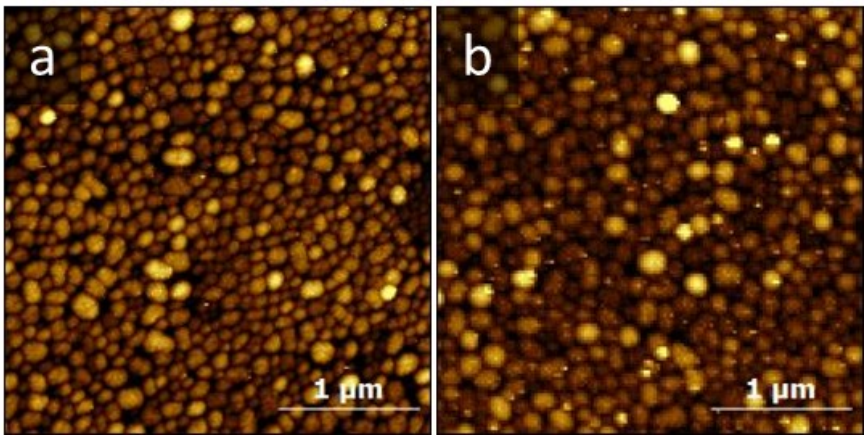

Figure 3. 3 AFM images, 3µm x 3µm scan size, acquired on (**a**) ZnO and (**b**) ZnCoO.

Figure 3.2 shows FESEM topographies, obtained on (a, c) pure and (b, d) Co-substituted ZnO samples, respectively. As shown in figures 3.2a,b, both ZnO and ZnCoO have the same granular morphology, with a lateral grain size ranging from 50 to 200 nm. Even though the FESEM images of figure 3.2a,b seem to indicate a growth of the materials in spaced nano-islands, more detailed analysis, obtained both by standard- and transverse-FESEM, presented in Figure 3.2c,d, revealed an under connection between those islands. In particular, Figure 3.2c shows a transverse FESEM image acquired on ZnO. In order to image the film transversally, the sample was cracked along an atomic plane of the Si substrate and measured by FESEM. This image was acquired with 1M magnification and an acceleration voltage of 16kV, and

highlights, in grey contrast, the material difference between ZnO (brighter) and Si substrate (darker). Such an image clearly shows (1) the granular growth of the film (2) the interconnection between grains (3) a film thickness of d≈75 nm. Figure 3.2d is a close-up of ZnCoO surface, showing the interconnection between bigger grains because of a carpet of smaller crystallites.

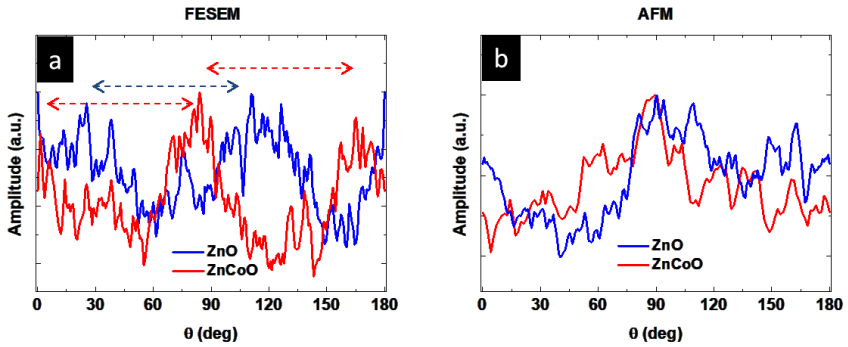

Figure 3. 4 Angular distribution of **a** ZnO and **b** ZnCoO grains, as extracted from Figure 3.3a and b, respectively.

AFM topographies reported here are representative of tens of measurements performed on six samples, three of pure and three of Co-substituted ZnO, covering a total area of 500μm x 500μm. In particular, Figures 3.3a,b are topographies obtained on ZnO and ZnCoO, respectively. Those images were acquired by keeping the same scan size of FESEM measures, to facilitate the direct comparison of morphological features, as seen by FESEM and AFM. Both techniques agree on granular growth of the films and lateral grain size.

The angular distribution of ZnO and ZnCoO grains, imaged by FESEM and AFM, is reported in Figure 3.4a (FESEM) and b (AFM). In the case of FESEM images, the angular distribution reveals an orientation of ≈30-120 deg in pure and ≈85-175 deg in Co-substituted ZnO. Such a 90deg-difference, highlighted by the dotted arrows in Figure3.4a, indicates that the length and breadth axis of the grains are perpendicular each other.

On the other hand, the angular distribution of the grains as extracted from AFM images (Figure3.4b) indicates that AFM is measuring more rounded features on both pure and Co-substituted ZnO samples. This discrepancy can be justified by taking into account that the AFM measurements is affected by the shape convolution of the morphological features with the probe.

	ZnO		ZnCoO	
	FESEM	**AFM**	**FESEM**	**AFM**
S_a **[nm]**	n.a.	7.03	n.a.	5.53
S_q **[nm]**	n.a.	8.85	n.a.	7.23
Roundness	0.60	0.52	0.64	0.54
Form Factor	0.75	0.50	0.79	0.58

Table 2. Roughness and shape analysis results for ZnO and ZnCoO thin films.

Surface roughness has been measured by AFM, and the arithmetic average of roughness profile and the root mean square (namely S_a and S_q, respectively) have been calculated. Moreover, for both FESEM and AFM images, *roundness* and *form factor* values have been calculated aiming at characterizing the grain shape. In detail, Sa (S_q) is the roughness average (root mean square), defined as $S_a = \frac{1}{MN}\sum_{i=0}^{M-1}\sum_{j=0}^{N-1}\left|z(x_i, y_j)\right|$ $\left(S_q = \sqrt{\frac{1}{MN}\sum_{i=0}^{M-1}\sum_{j=0}^{N-1}\left[z(x_i, y_j)\right]^2}\right)$; *roundness* describes the shape's resemblance to a circle (the *roundness* factor of a shape will approach 1.0 the closer the shape resembles a circle or $2/\pi \approx 0.63$ the closer the shape resembles a square) and it is defined by $Roundness = \frac{4\frac{Area}{\pi}}{(Maximum\ Diameter)^2}$; *form factor* provides a measure that describes the shape of a feature and is defined by $FormFactor = \frac{4\pi\ Area}{Perimeter^2}$. Results of roughness and shape analysis are reported in Table 2.

The direct comparison between S_a and S_q values in ZnO and ZnCoO indicates a higher average roughness and root mean square for the pure ZnO with respect the

Co-substituted one. On the other hand, *roundness* values for the two materials are similar but, as already explained for the angular distribution discrepancy, they are strictly dependent on the imaging techniques. The FESEM images (Figure 3.2) clearly show a population of squared grains, consistent with *roundness* values of 0.60 (ZnO) and 0.64 (ZnCoO), whereas the tip-convoluted, elliptical-like, shape of the grains imaged by AFM results in a roundness of 0.52 (ZnO) and 0.54 (ZnCoO). The same reasoning for the *form factor*, where similar values have been obtained for pure and Co-substituted ZnO samples but different depending on the imaging technique. In this case, from FESEM (AFM) images I obtained a *form factor* of 0.75 (0.50) for ZnO and 0.79 (0.58) for ZnCoO.

Discussion.

The comparison between structural characterizations of ZnO and ZnCoO has first confirmed that the Co-dilution agrees with the expected nominal Co-content of 5%. In addition to this, XRD spectra revealed that Co-substitution does not alter the overall crystallinity of ZnO, although a higher mosaicity of ZnCoO has been shown by the ω-scan. On the other hand, morphological analysis of pure and Co-substituted samples, by AFM and FESEM, have highlighted a similar peculiar morphology made by highly packed interconnected grains. The similar values of *roundness* and *form factor* for pure and Co-substituted ZnO indicates that Co substitution (at 5%) does not alter the growth of the material.

Finally, transverse FESEM has given insights into the presence of a sharp interface between the high conducting *p*-type Si substrate and Zn(Co)O grains, allowing at the same time a measure of the film thickness.

3.3 The effect of Co-substitution on the reactive properties of ZnO surface

Introduction.

In this section, I studied the effect of Co-substitution on the sticking probability of gas molecules at ZnO surface. The presence of adsorbed species at the material surface and the surface reactivity when exposed to ambient atmosphere, were studied by UV-assisted SPM experiments, aiming at measuring UV-photovoltage and UV-photocurrent effects, both in air and UHV conditions. In particular, in-air-KPFM and C-AFM measurements were carried out both in dark and UV lighting, by using "MultiMode V" AFM by VEECO. In this case, the AFM was equipped with an optical path having a low power light source (wavelength range 200-800 nm), a Jobin-Yvon "H.10" Monochromator (wavelength ±5 nm) and optical lenses, needed to focus the UV light on the under-tip region of sample surface. On the other hand, the effect of in-vacuum-annealing on sample adsorbates has been investigated, by performing SPM experiments afterwards, both in air (by means of Multimode V AFM) and in UHV-conditions (by means of the "Omicron RT-AFM/STM").

Surface photo-voltage measurements.

To investigate the surface photovoltage phenomenon on both ZnO and ZnCoO, I performed UV-assisted KPFM experiments, aiming at measuring the contact potential difference, $V_{CPD}=(W_{probe}-W_{sample})/e$, both in dark and UV-lighting conditions. The surface photo-voltage (SPV) is then defined as $V_{CPD}^{(UV)} - V_{CPD}^{(dark)}$.

Figure 3.5a-b show V_{CPD} maps acquired on ZnO (a) and ZnCoO (b). Those maps have been acquired in dark conditions by using the same PtIr AFM probe, in order to have the same work function reference (W_{probe}) when measuring V_{CPD}. Moreover, to facilitate the direct comparison between V_{CPD} maps, Figure 3.5a-b are here presented by using the same colour scale and contrast range from 320mV to 480mV. Figure 3.5c shows V_{CPD} histograms as measured from V_{CPD} maps of Figure 3.5a-b. Such distributions are centered at 450 mV and 340 mV for ZnO and ZnCoO respectively, with a standard deviation of 10 mV, confirming the spatial uniformity of V_{CPD} in both samples. It results that the contact potential difference of ZnCoO is down shifted of (110±20) mV with respect to the pure material. Moreover, given the positive sign of V_{CPD}, the P-S interface between PtIr probe and Zn(Co)O behaves as a Schottky barrier [1].

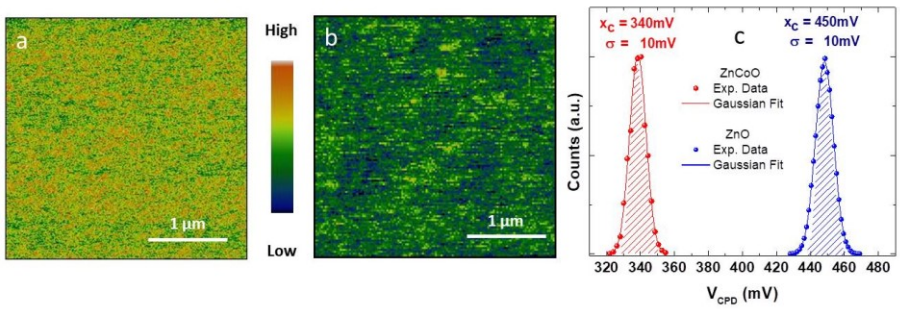

Figure 3. 5 a-b KPFM maps, 3µm×3µm in lateral size, of ZnO (**a**) and Co:ZnO (**b**), acquired in air and dark illumination conditions; (**c**) V_{CPD} distributions of ZnO (in blue) and ZnCoO (in red) extracted from **a** and **b**, respectively.

The same measurements were performed by irradiating the surface region under the AFM probe in the 280 nm to 440 nm wavelength range (4.4 eV to 2.8 eV), in order to light up the presence of the SPV. In particular, Figure 3.6a and 3.6c compare V_{CPD} maps of as-grown ZnO (a) and ZnCoO (c), respectively in dark and under UV-light conditions, with a wavelength of 340 nm (3.65 eV). As for previous measurements, the same PtIr AFM-probe was kept for each pair of maps (dark-UV)

to have the same work function reference (W_{probe}). V_{CPD} distributions both under dark and UV-lighting conditions are shown in Figures 3.6b,d, on (b) pure ZnO and (d) ZnCoO, and fitted by a Gaussian function.

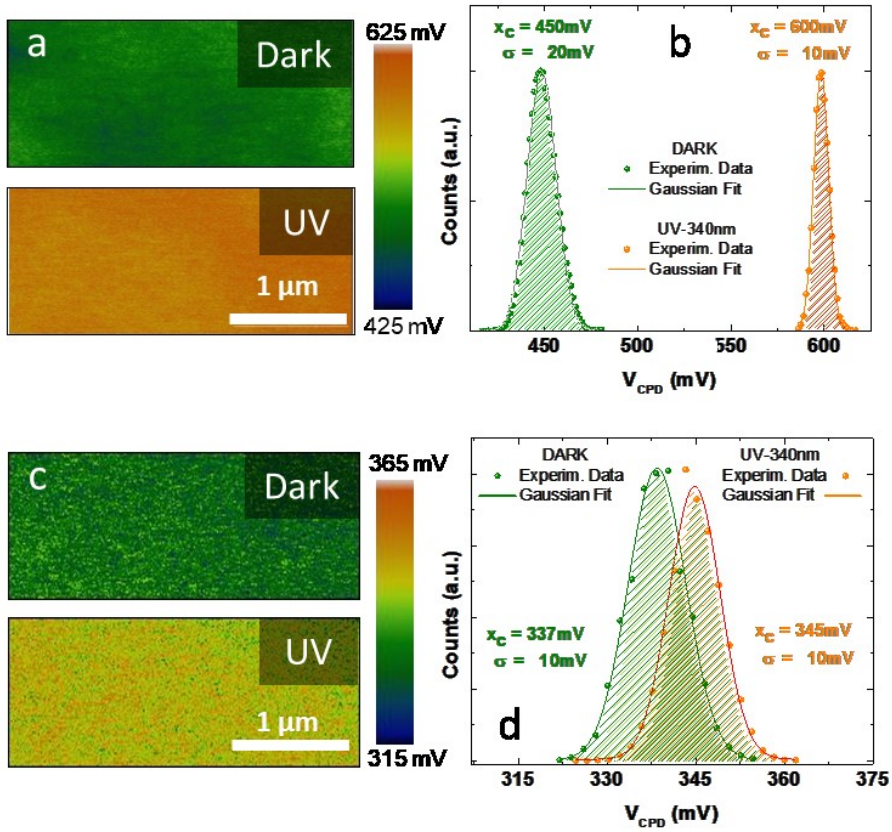

Figure 3. 6 a KPFM maps, 3µm×1µm in size, of as-grown ZnO in dark conditions (top) and under UV-lighting (bottom), acquired in air; **b** V_{CPD} distributions of dark (green) and UV-irradiated ZnO (orange) from a statistic of 256×256 points equally distribute on 3µmx3µm scan areas, fitted by Gaussian function; **c** KPFM maps, 3µm×1µm in size, of ZnCoO in dark conditions (top) and under UV-lighting (bottom), acquired in air; **d** V_{CPD} distributions of dark (green) and UV-irradiated ZnCoO (orange) from a statistic of 256×256 points equally distribute on 3µmx3µm scan areas, and fitted by Gaussian function.

Standard deviations of 10 to 20 mV confirm a good spatial uniformity of V_{CPD} and, in particular, the sharpening of the V_{CPD} peak under UV lighting is strictly related to the effect of UV on surface adsorbates (that will be discussed later). In this case the desorption of gas molecules and the consequent "cleaning" of the surface, increases the uniformity of the measured V_{CPD} values.

As a consequence of the UV lighting, V_{CPD} shifts to higher values in pure ZnO (Figure 3.6a), resulting in SPV=(150±30) mV. On the contrary, the V_{CPD} change of ZnCoO, as a consequence of UV illumination, is much smaller, resulting in (10±20) mV of shift. Moreover, further SPV measurements were performed by sweeping the light wavelength from 440 nm down to 280 nm (2.8eV to 4.4eV). Figure 3.7a shows the behaviour of SPV as a function of photon energy (light wavelength) for both ZnO (blue dots) and ZnCoO (red dots).

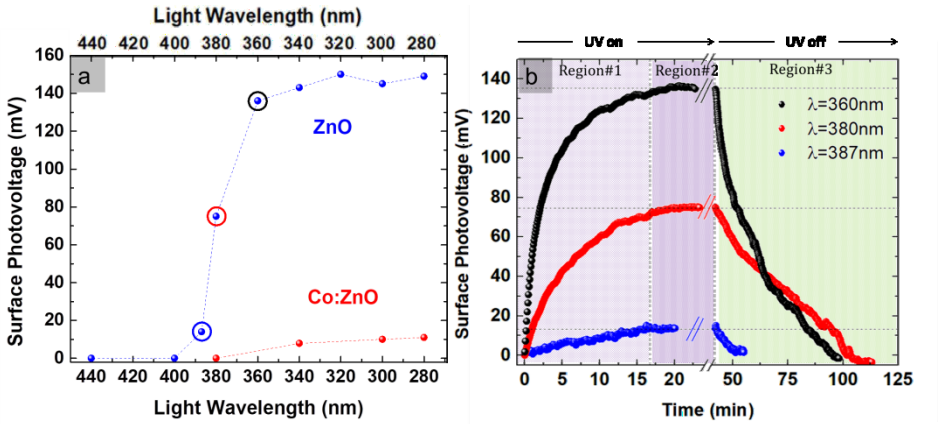

Figure 3. 7 a SPV vs Photon Energy (Light Wavelength) of ZnO (in blue) and ZnCoO (in red); **b** SPV rise and decay processes measured on ZnO for 3 representative wavelength of 360, 380 and 387 nm. Colour of circlets in **a** correspond to the same colour curve in **b**.

Consistently with results of figure 3.6, a minor effect of UV light on Co-substituted ZnO is always measured at any considered light wavelength. In agreement with photoluminescence results[2], photons with energy in the range 2.8÷3.2 eV do not affect ZnO (blue curve) and ZnCoO (red curve) photo-response. On the other hand, as soon as the wavelength-light gets equal to 380 nm (photon energy 3.26 eV), an

appreciable SPV appears in ZnO and becomes more effective as it approaches 370 nm (3.35 eV),where photons transfer an amount of energy to electrons comparable to the material band-gap. Finally, a saturation of SPV value occurs as 360 nm (3.44 eV) is overcome. Given a room temperature band gap of 3.37eV[3] for ZnO, the presence of a non-zero a SPV even when the photon energy is 110 meV (≈4.5 k_BT) lower than the nominal material band-gap, is justified by the thermal energy smearing at the measurements temperature of 293 K.

On the contrary, I did not measure any appreciable SPV when lighting the ZnCoO with a wavelenght of 370 nm (3.35 eV), whereas a very small SPV of 10 meV only occurs at a wavelength (photon energy) equal or lower (higher) than 340 nm (3.65 eV). In addition to this, the time evolution of SPV in pure ZnO during UV irradiation at 360, 380 and 387 nm is reported in Figure 3.7b (black, red and blue SPV lines of Figure 3.7b correspond to the blue dots of Figure 3.7a, enclosed into black, red and blue circles). As shown, the UV-light is turned on at t=0sec and SPV gradually increases (Region#1), reaching the saturation in about 17 minutes. At this point, the light is kept on for about half an hour (Region#2) to verify the equilibrium regime and, after that, it is turned off in order to follow the SPV relaxation (or decay) (Region#3).

In order to check wheatear the measured SPV behaviour is a consequence of surface adsorbates release (when UV is on – Region#1+2) and re-adsorption (when UV is off – Region#3), the samples were annealed in HV conditions, to favour adsorbates thermal release, and then measured again. If gas molecules are released from the surface, because of the annealing procedure, no change will be measure in V_{CPD} when UV is turned (SPV=0).

The annealing procedure was performed by heating the sample up to 400°C, at a pressure of $6x10^{-5}$ mbar, paying attention not to modify sample structure, morphology and composition. The results of the UV-assisted KPFM experiments performed after HV annealing, at wavelength of 340 nm, on both pure and Co-substituted ZnO are summarized in the table of Figure 3.8: both ZnO and Co-substituted ZnO show the same SPV of 15±10 mV, supporting the hypothesis of surface adsorbates release from ZnO surface and the absence of those at Co-

substituted ZnO surface.

To further investigate the SPV phenomenon in ZnO (which exhibits the highest response to UV and annealing procedure), the annealed ZnO sample was exposed back at air, and the time evolution of V_{CPD} in dark conditions was measured.

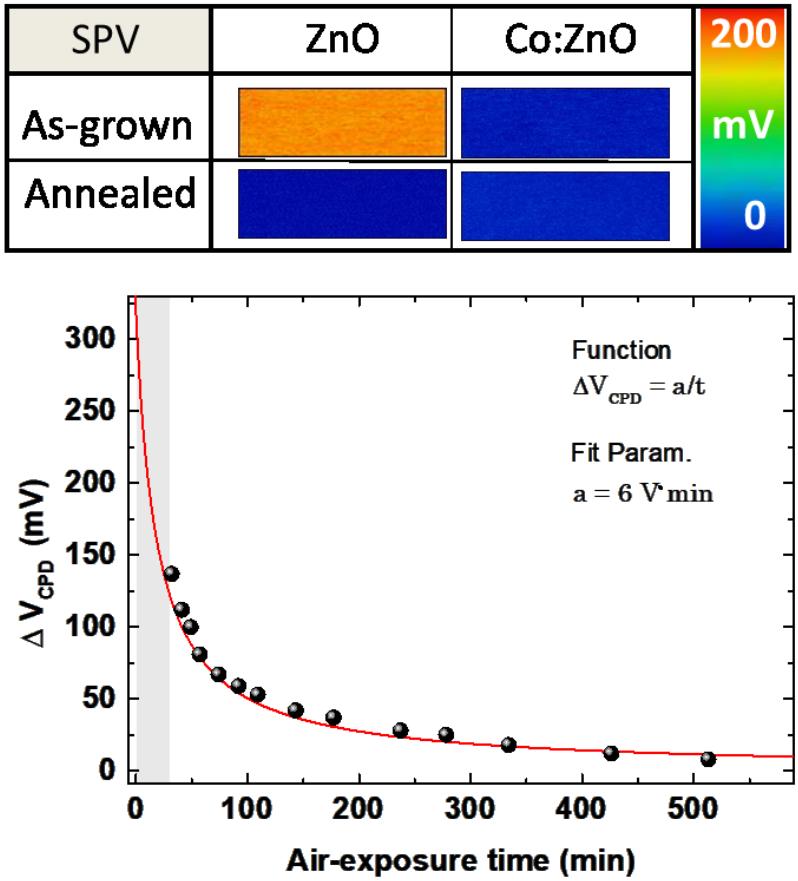

Figure 3. 8 Top: SPV comparison between as-grown and annealed ZnO and ZnCoO. Cropped maps are 1µm x 3µm in size. Bottom: recovering time of SPV in ZnO in air after annealing.

Figure 3.8 (bottom) shows $\Delta V_{CPD}(t)$ as a function of the air exposure time, i.e. $\Delta V_{CPD}(t) = V_{CPD\text{-}HV\ ann.} - V_{CPD}(\textit{air exposure time})$. The experimental data (black dots) are fitted by the power law function $\Delta V_{CPD} = a/t$, in red, with a=6 Vmin. The time

change of V_{CPD} is justified by assuming a gradual re-adsorption of gas molecules, which affect the value of ZnO surface work function. Indeed, such a power law behaviour is well known to be expected in the case of chemical adsorption of molecules on the surface. Stochastic processes depict these phenomenon, by taking into account the percentage of molecules surface coverage and their sticking probability. By following these models, the re-adsorption process is regulated by different parameters, such as the flux of particles (F), the sticking probability (S) of gas molecules to the surface and the surface coverage (θ). In first approximation, the time evolution of the coverage is given by a recursive expression, $\theta(t) = F\,S\,t$, where S depends on the coverage and can be modelled as $\frac{S}{S_0} = (1 + K\frac{\theta}{1-\theta})^{-1}$ [4], giving rise to a stochastic Markov chain. In the latter formula, K depends on molecules sticking probability to be (1) chemisorbed, (2) chemi-desorbed and (3) physisorbed if chemisorbed already. S_0 is the sticking probability when the surface is completely free (i.e. the first incoming particle has all of the sites available). Even though the description of adsorbates' dynamics is highly not trivial, the inverse proportionality between ΔV_{CPD} and θ is rather intuitive, resulting in an power law decay trend, that is a typical behaviour of *packing vs. space* problem[4].

Summarizing, we can notice that: (1) the annealing procedure, which usually leads to the desorption of surface adsorbates, is very effective on ZnO, confirming the presence of gas molecules at its surface; (2) the annealing procedure is not effective on ZnCoO, bringing to the conclusion that the Co-substitution affect the reactivity of sample surface, inhibiting the adsorption; (3) the SPV of after-annealing ZnO is the same as ZnCoO (not affected by the annealing procedure), confirming the conclusion (1) and (2); (4) ZnO recovers the before-annealing-V_{CPD} on characteristic long time scale (≈530min.) .

All of these points are consistent with the re-adsorption dynamics of gas molecules at material surface that reflects the band-bending increase as the number of adsorbates increases. It is worth noting that the initial 30 minutes of the re-adsorption process are missing in the experimental data of Figure 3.8, because this time window overlaps with the time needed to bring the sample out from the HV

chamber and set up the KPFM experiment (grey area). Moreover, EFM experiments have been performed in UHV conditions on the annealed samples, to measure the work function of adsorbates-free surfaces. In this case, the in-air sample transfer from the HV-annealing chamber to the UHV-measurement one lasted less than 1 minute.

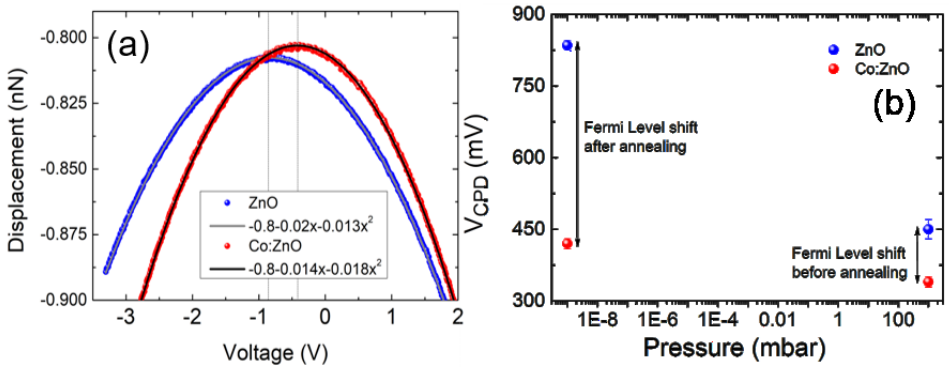

Figure 3. 9 a D-V curves representative of EFM measurements, in UHV, on ZnO (in blue) and Co:ZnO (in red), with correspondent second-order polynomial fitting function; **b** summary of results of KPFM and UHV-EFM experiments, in ambient and vacuum conditions, on ZnO and ZnCoO.

In general, EFM measures the "cantilever-deflection vs DC-voltage (D-V)", resulting in a parabolic behaviour. Figure 3.9a shows representative D-V curves for both ZnO (in blue) and ZnCoO (in red), acquired with the same PtIr AFM probe, to keep the same work function reference. The D-V curves, different in both center and curvature of the parabola, reflecting the different electrostatic interaction of the PtIr AFM probe with pure and Co-substituted ZnO, were fitted by a second-order polynomial function $F_N=aV^2+bV+c$, where F_N is the normal electrostatic force acting between the probe and the sample, V is the bias voltage. The V_{CPD} is then found at the minimum of the normal force. By fitting the D-V curve, the V_{CPD} is found as $V_{CPD}=b/2a$, resulting in $V_{CPD}^{ZnO-UHV} = 830\,mV$ and $V_{CPD}^{ZnCoO-UHV} = 420\,mV$. It worth noticing that when dealing with adsorbates-free surfaces the difference in V_{CPD} due to Co substitution has been found to be $(V_{CPD}^{ZnO-UHV} - V_{CPD}^{ZnCoO-UHV}) = 410\,meV$

rather than $(V_{CPD}^{ZnO-air} - V_{CPD}^{ZnCoO-air}) = 110\,mV$, as summarized in Figure 3.9b. Moreover, in the hypothesis of an adsorbates-free surface for ZnCoO we can assume $V_{CPD}^{ZnCoO-UHV} \approx V_{CPD}^{ZnCoO-air}$ as cross-reference value for measurements in air and UHV. In this case, by considering the difference $(V_{CPD}^{ZnO-UHV} - V_{CPD}^{ZnCoO-UHV}) - (V_{CPD}^{ZnO-air} - V_{CPD}^{ZnCoO-air})$, I obtained that the net contribution of adsorbates to the band bending is $V_{CPD}^{ZnO-UHV} - V_{CPD}^{ZnO-air} = 300\,mV$.

These results are summarized below:

	Annealed	ZnO-Adsorbates	ZnCoO-Adsorbates	V_{CPD}(ZnO)-V_{CPD}(ZnCoO)	W(ZnO)-W(ZnCoO)
Air	NO	YES	NO (Few)	+110mV	-110meV (E_F in ZnCoO moves toward the valence band)
Ultra-High Vacuum	YES	NO	NO	+410mV	-410meV (E_F in ZnCoO moves toward the valence band)

$$(V_{CPD}^{ZnO} - V_{CPD}^{ZnCoO})UHV - (V_{CPD}^{ZnO} - V_{CPD}^{ZnCoO})air = 300mV$$

$$V_{CPD}^{ZnO;UHV} - V_{CPD}^{ZnCoO;UHV} - V_{CPD}^{ZnO;air} + V_{CPD}^{ZnCoO;air} = 300mV$$

In the hypothesis of adsorbates-free surface for ZnCoO: $V_{CPD}^{ZnCoO;UHV} \approx V_{CPD}^{ZnCoO;air}$

$$V_{CPD}^{ZnO;UHV} - V_{CPD}^{ZnO;air} = 300mV$$

Photo-conductive properties.

The effect of Co-substitution on the surface properties of ZnO has been further investigated by performing C-AFM experiments both in air and in ultra-high vacuum ($P<10^{-9}$ mbar), on ZnO and ZnCoO, while keeping the bias voltage at 0V, to light up the presence of surface charged areas. Figure 3.10 shows C-AFM maps acquired on (a) as-grown ZnO in ambient conditions, (b) in-vacuum annealed ZnO, and (c)

ZnCoO in ambient conditions, on scan size of 3μm×3μm. When as-grown ZnO is first measured in ambient conditions, C-AFM maps acquired at zero bias (Figure 3.10a) show regions where a negative current of about 5nA is measured.

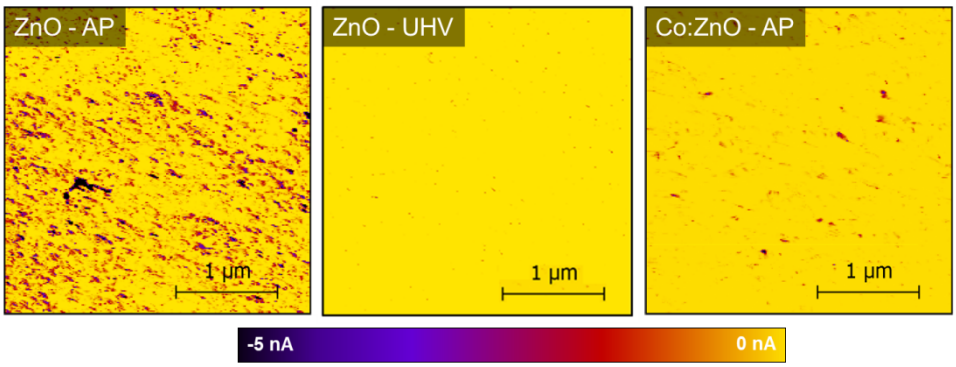

Figure 3. 10 C-AFM maps at V=0V of 3μm×3μm in size on (**a**) ZnO in air, (**b**) ZnO in UHV and (**c**) in ZnCoO. The colour scale has been equalized to the same range of values for all of the presented maps, in order to facilitate the direct comparison.

Given the negative sign of the measured current and being the AFM probe grounded, we can deduce the presence of negative charges at ZnO surface. To check if such negative charges are coming from surface adsorbates I repeated C-AFM measurements at V=0V in UHV conditions ($P<10^{-9}$ mbar), after having annealed the sample at T=120°C and a pressure of $6x10^{-5}$ mbar for 90 minutes. After the annealing procedure, the density of charged areas is strongly suppressed as shown in Figure 3.10b, indicating that localized charged across the surface are removed by the UHV annealing procedure. On the other hand, Figure 3.10c shows the result of C-AFM at V=0V on ZnCoO in air: the density of charged areas is much lower in this sample even when measured in air, further confirming the role of Co substitution in suppressing surface reactivity.

Moreover, I observed that the excess of negative charges at sample surface, when in ambient conditions, can be locally removed by repeatedly scanning the grounded AFM probe on the same area. Figure 3.11 compares such a tip induced discharge process in ZnO and ZnCoO, on the left- and on the right-hand column, respectively,

in dark (top) and UV-irradiation conditions (bottom). All the C-AFM maps of Figure 3.11 are 3µm x 1µm in lateral size and have been analysed afterwards by setting a constant current threshold of -1 nA.

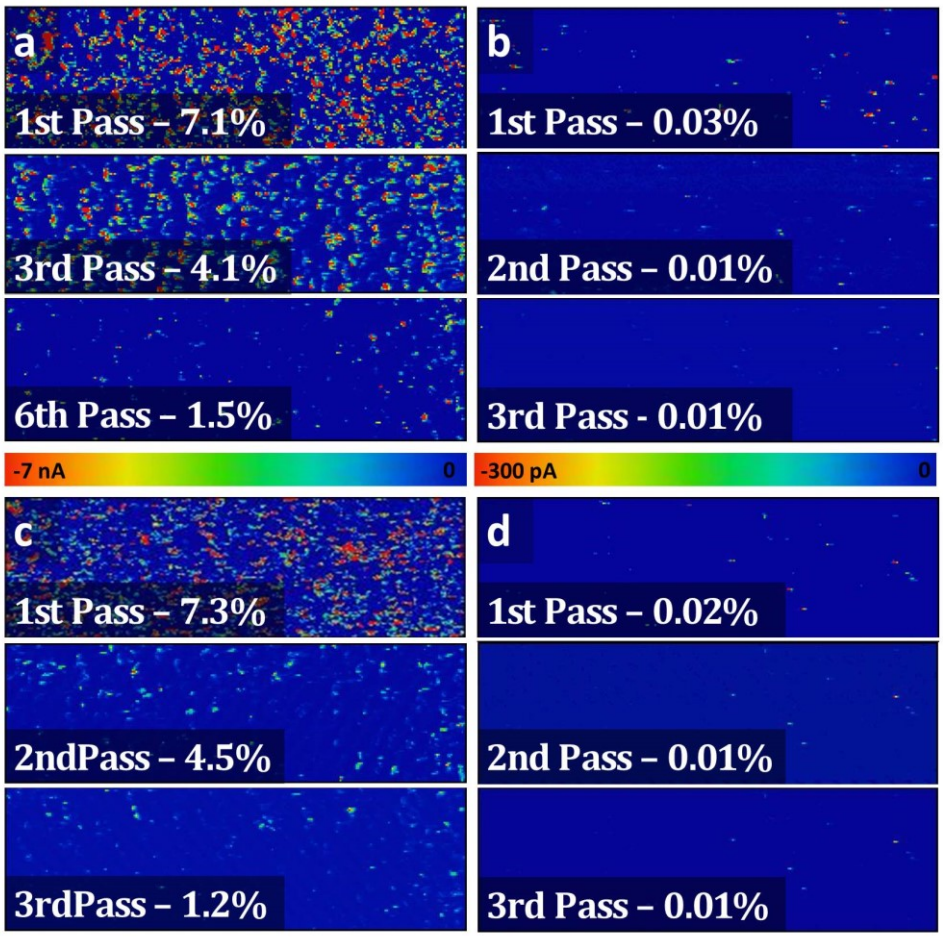

Figure 3. 11 C-AFM maps acquired on (**a**, **c**) ZnO and (**b**, **d**) ZnCoO of subsequent scanning with grounded probe and 0V bias applied in (**a**, **b**) dark and (**c**, **d**) UV light conditions. Each frame reports the percentage of scanned area with measured current above |-1 nA|.

In dark conditions, we found a density of over-threshold charged areas of 7.1% in ZnO and only 0.03% in ZnCoO, as reported in Figure 3.11a and b, respectively. Furthermore, six scans are needed to bring this percentage down to 1.5% in ZnO,

whereas it is already 0.01% after the 2nd scan in ZnCoO. I performed the same discharging procedure on both ZnO and ZnCoO, this time by turning the UV light on after the 1st scan. The results are shown in the bottom part of the Figure 3.11. In this case the discharge process is much faster and 3 scans are enough to bring the percentage of charged areas down to 1.2% in ZnO (six scans were needed to reach the same percentage in dark conditions). On the contrary, ZnCoO did not show any significant difference when the discharge process is performed in dark or in UV lighting conditions.

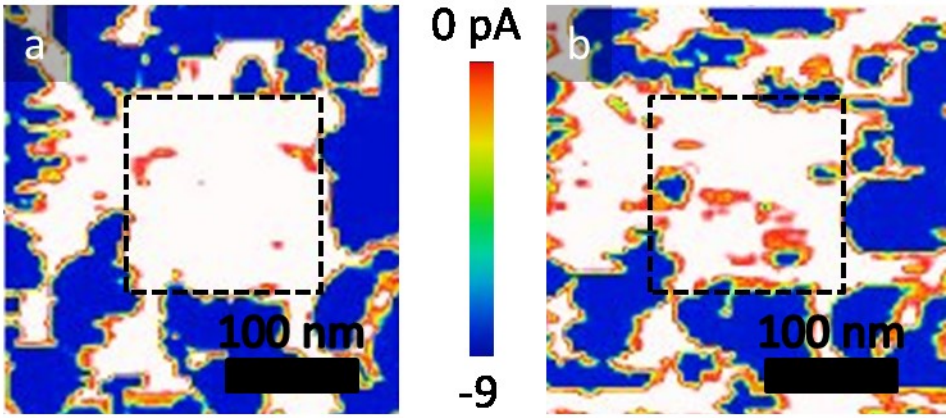

Figure 3. 12 Re-charge process of the ZnO surface investigated by means of 0V bias C-AFM experiments. **a** C-AFM map after the discharge process of a sub-area (highlighted with a dashed square) and **b** after 1 hour.

Finally, I used C-AFM technique to visualize the process of re-adsorption of gas molecules at ZnO surface. In this case, I freed a portion of the ZnO surface by subsequently scanning with the AFM probe grounded and then waited 1 hour before scanning it again. Figure 3.12a-b show C-AFM maps on the same scan area. A close up of this area (in the blue dotted square) was discharged by subsequently scanning the grounded tip above the surface. After the discharging process, a transport current of about 0 pA (white in the colour scale) is measured almost everywhere inside the blue dotted square of Figure 3.12a.

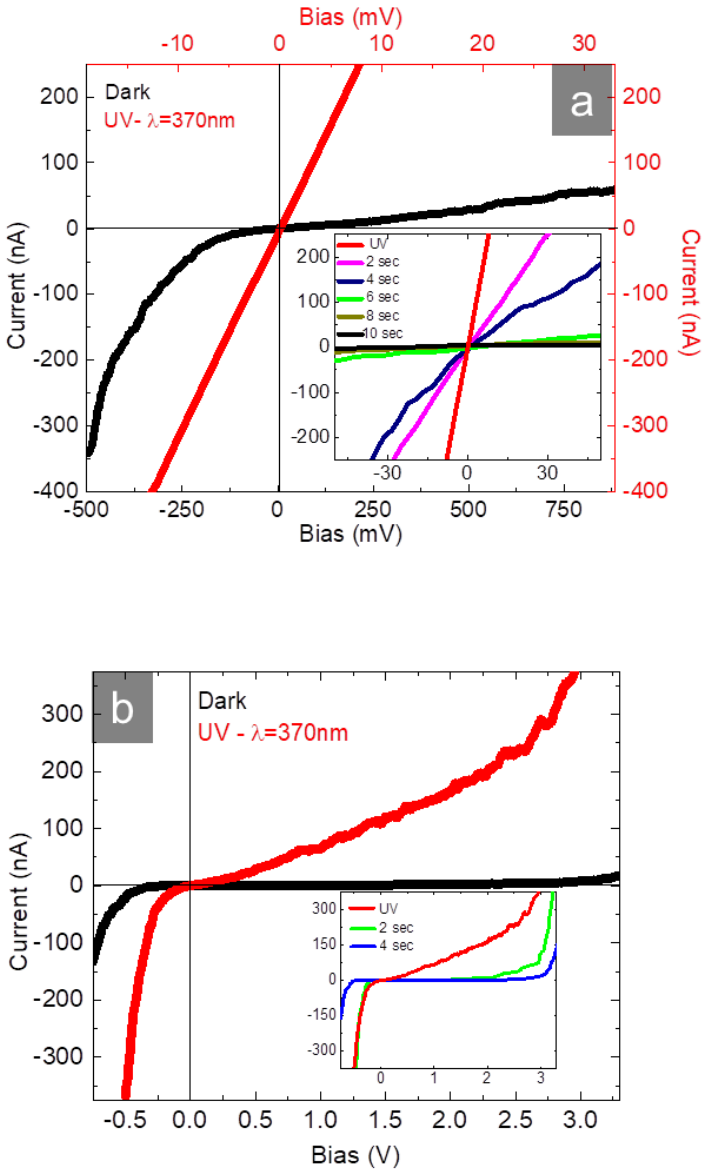

Figure 3. 13 Main plots: IVs in dark (black) and under UV-illumination conditions (red) acquired on (**a**) ZnO and (**b**) ZnCoO. The drastic change in conductivity for ZnO is not present in ZnCoO. Insets: representative IVs showing the behaviour of the conductivity in ZnO and ZnCoO after the UV excitation have been turned off.

After one hour waiting, I repeated the C-AFM measurement on the same area and, as shown in Figure 3.12 b, charged areas reappeared again. Such a result is in agreement with the reabsorption of gas molecules and with the reactive surface scenario.

In addition to this, I studied the effect of Co-substitution on the photo-conductive properties of ZnO by investigating the behaviour of the photocurrent at ambient pressure under illumination with UV monochromatic light. In details, I performed C-AFM in spectroscopy by means of Multimode V AFM, in dark and UV-lighting conditions. The main plots of Figure 3.13 show the average of more than hundreds IVs for ZnO and ZnCoO acquired in dark conditions and under UV-lighting (in black and red respectively), having a wavelength of 370nm (3.35 eV), that reasonably compares to the material band gap.

In dark conditions, both ZnO and ZnCoO IVs exhibit a Schottky-like behaviour, due to the metal/semiconductor interface occurring at the contact area between Pt-AFM probe and ZnO (ZnCoO). In order to compare ZnO and ZnCoO conductivity, the same contact pressure of 1.4μN has been applied during C-AFM measurements on both samples, in order to have the same Pt-AFM probe/sample contact area. This comparison shows that current transport at sample/AFM probe interface is higher in ZnO with respect to ZnCoO at any applied bias. Such an effect has been addressed to the capability of Co substitution to form Co-V_O complexes, introducing new energy levels inside the band gap able to trap free electrons.

When turning the UV-light on, ZnO switches into a high-conductance state (red IV of Figure 3.13a), as a consequence of the creation of electron-hole pairs due the illumination with supra-band-gap photons. On the contrary, the same UV-light only causes a minor change of the IVs when in presence of Co-substitution (red curve in Figure 3.13b). Moreover, the insets of Figure 3.13 show that, when turning the UV light off, the recovery times of ZnO and ZnCoO are different, resulting in about 10s and 4s, respectively.

Discussion.

The effect of Co-substitution on electrical conductivity and surface reactivity of ZnO has been investigated by means of scanning probe microscopy experiments, such as C-AFM, KPFM and EFM. The results of these measurements lighted up:

(1) A reduction of conductivity in ZnCoO with respect to ZnO;
(2) A reduction of surface reactivity of ZnCoO with respect to ZnO;
(3) An increase of ZnCoO work function with respect to ZnO.

All of these findings can be explained within a theoretical model which deals with the appearance of an impurity band in ZnCoO, due to the formation of Co-V_O complexes, that sucks electrons from the donor levels[5,6].

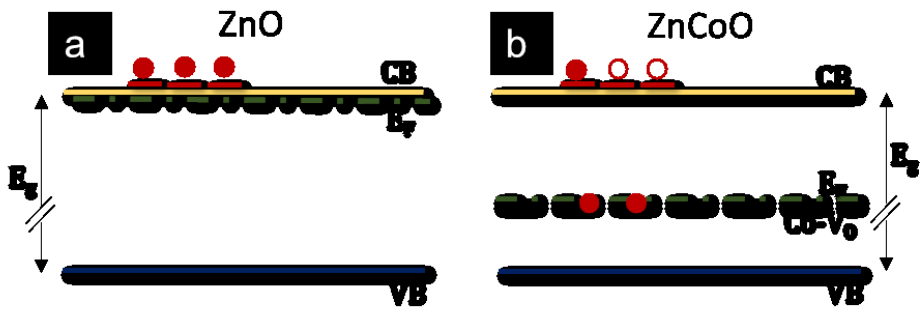

Figure 3. 14 Sketch of the electronic band structure, for (**a**) ZnO and (**b**) ZnCoO. Free electrons in CB, from donor levels (red dots), reduce their energy by moving into lower energy levels introduced by C-V_O complexes.

Figure 3.14 sketches a scheme of ZnO (a) and ZnCoO (b) band structure in the bulk. In both cases conduction band (CB) and valence band (VB) are separate by an energy interdicted region E_g=3.37eV (at room temperature), the band-gap. In ZnO, the Fermi energy (E_F) is inside the band-gap, closer to CB, due to the presence of E_D (red dots) which give rise to its *n*-type semiconducting nature. In ZnCoO (Figure 3.14b), Co-V_O complexes introduce empty electronic levels above the conduction

band edge of ZnO. When a large concentration of free carriers exists, as in *n*-type ZnO, these levels may get occupied and act as localized traps for the carriers. A downward shift of the Fermi energy is to be expected, in view of a reduced number of electrons in the conduction band. This simple sketch results from DFT calculations at the generalized gradient approximation with the Hubbard-U correction level of approximation[6] for the band structure modifications induced by Co-V_O complex formation in ZnO. Figure 3.15 shows the DFT electronic structure for neutral and negatively charged Co-V_O in ZnO.

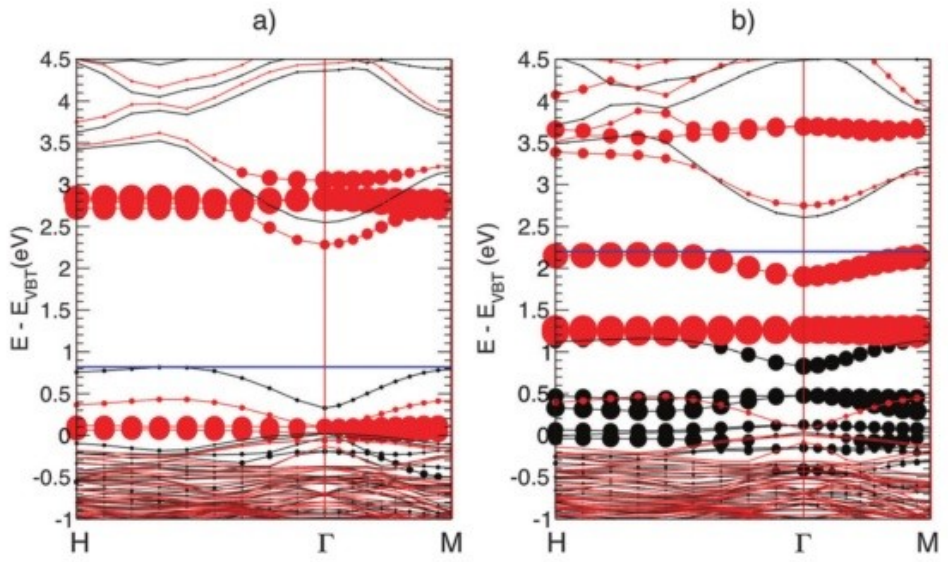

Figure 3. 15 Spin-polarized electronic band structure along the H–Γ–M direction, for the neutral **(a)** and negatively charged **(b)** Co–V_O complex in ZnO[6].

Macroscopic transport measurements on samples with similar Co-content show a reduction of electron conductivity in Co-substituted ZnO, in agreement with such a theoretical model[6,7]. Moreover, microscopic C-AFM experiments here reported have further confirmed this behaviour. However, the lower number of free electrons in CB, which leads to a reduction of the conductivity, also affects the surface reactivity of ZnCoO: the incoming gas particles do not find many free electrons to be

chemisorbed with, resulting in a net reduction of surface molecule coverage. The investigation of surface reactivity and its comparison between ZnO and ZnCoO have been pursued by performing C-AFM at 0V, UV-assisted KPFM and after-annealing in-air KPFM and in-vacuum EFM, resulting in: (1) C-AFM maps at 0V bias show a much higher density of charged areas in ZnO with respect to ZnCoO surface, (2) UV-assisted KPFM experiments show a SPV of (150±30) mV in ZnO and only (10±20) mV in ZnCoO, (3) ZnO shows a time-dependence of V_{CPD} after annealing or UV-lighting in air, whereas no change are measured in vacuum conditions or on ZnCoO. All of these findings agree with a reduced surface reactivity in Co-substituted ZnO.

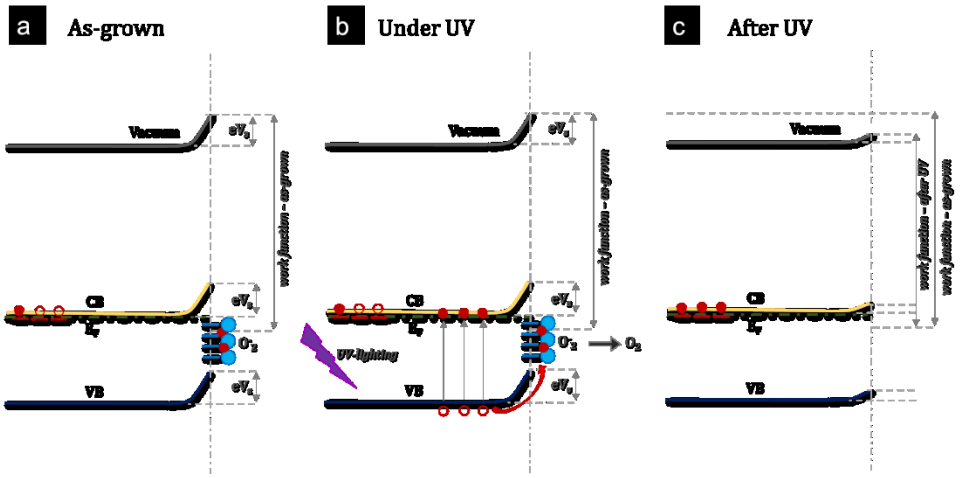

Figure 3. 16 Sketch of the energy band structure, close to the surface in ZnO (ZnCoO) (**a**) as-grown (**b**) UV-lighted and (**c**) after-UV.

Clearly, the presence of adsorbates is supposed to affect the energy band structure at the material surface. In this scenario, Figure 3.16a shows a sketch of ZnO band diagram in presence of surface adsorbates: typically ZnO surface undergoes to a chemisorption of adsorbates like O_2 molecules, which capture electrons from the CB ($O_2 + e^- \rightarrow O_2^-$) and give rise to an electron depletion layer and an upward bend-banding of VB, CB and Vacuum, of a quantity eV_s. Upon illumination with photon energies comparable to or larger than the band gap energy, photo-excited holes will

migrate to the surface along the potential gradient produced by the band-bending, discharging the adsorbates (Figure 3.16b), which will release the electrons back into the CB, as confirmed by "SPV vs photon energy" behaviour (in Figure 3.6a). When the releasing process is complete, the surface band-bending relaxes and the measured work function decreases, as shown in Figure 3.16c.

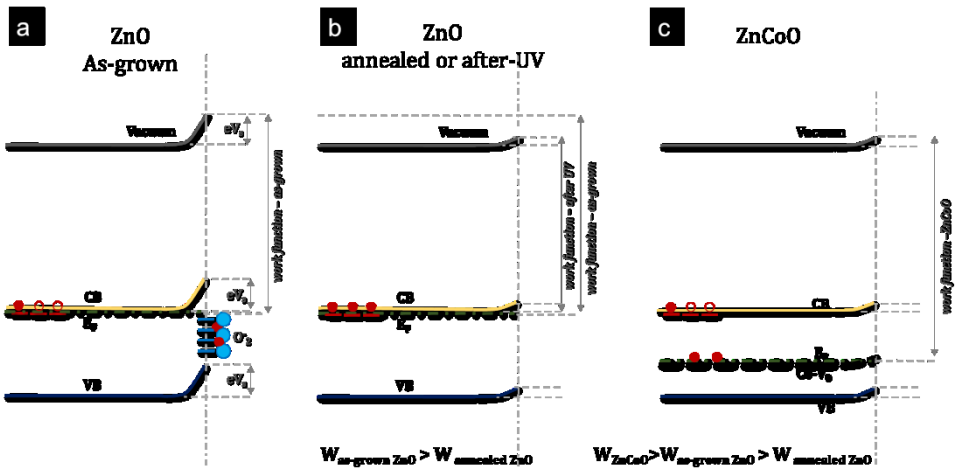

Figure 3. 17 Sketch of the electronic band structure, close to the surface in (**a**) as-grown ZnO (**b**) annealed or UV-irradiated ZnO (**c**) ZnCoO.

It is worth noting that a converse situation can occur: if adsorbates like atomic hydrogen transfer their electrons to the semiconductor, a positively charged surface and a downward band-bending will take place, giving rise to an electron accumulation layer. However, such a scenario would not be compatible with our results concerning the decrease of work function upon UV-lighting and has been proved to appear only after annealing at 850°C in reducing ambient[2]. The measured SPV of (150±30) meV in ZnO and (10±20) meV in ZnCoO, under UV irradiation confirms that (1) the work function on ZnO decreases upon illumination, in agreement with the chemisorption of O_2-like adsorbates and (2) the density of surface adsorbates (reflected in the eV_s material band bending) is strongly suppressed when substituting the Co into the ZnO.
In addition to this, the increase in work function due to Co-substitution (5%) has

been measure both by in-air KPFM (in presence of surface adsorbates) and in-vacuum EFM (with no surface adsorbates), resulting in 110 meV and 410 meV respectively. Even though both values indicate a downward motion of the Fermi level toward the VB (as sketched in figure 3.14b), due to Co substitution, a net difference of 300 meV is measured. Such a contribution has to be related to the presence of surface adsorbates in ZnO when performing in-air KPFM and their absence in in-vacuum EFM experiments. Figure 3.17a sketches the band structure of as-grown ZnO, reporting on a pronounced upward band bending due to the adsorbates at surface. When such adsorbates are released (because of in-vacuum annealing or UV-lighting) the charge depletion layer is reduced, leading to a decrease of the work function value (Figure 3.17b). We estimate as 300meV such a decrease, which would correspond to the contribution of the gas molecules to the surface band bending. As stated before, the presence of the impurity band, acting as electron trap, in ZnCoO (Figure 3.17c) reduces the number of free electrons and, indirectly, the surface reactivity, leading to a much reduced surface band banding with respect to ZnO. In this case, the work function increase, with respect to ZnO, is due to the downward motion of the Fermi level.

A further confirmation of the adsorbates presence on ZnO surface, relays on both the reversibility of V_{CPD}, in-air, after UV-lighting or annealing, and on the long-time-scale of its rise and decay. The reversibility its coherent with a phenomenon of desorption (when in-vacuum annealed or under UV-irradiation) and re-adsorption (when exposed to the air) of gas molecules at ZnO surface, mediated by photo-excited charge carriers and extrinsic defects, respectively. On the other hand, the long-time-scale deals with stochastic process of gas particles re-adsorption at the material surface .

Finally, the role of surface adsorbates has been definitively proved by comparing the relaxing trend of ΔV_{CPD} in air (shown in Figure 3.8), after annealing, to the stabile EFM measurement carried out in UHV. In the latter case, since the extreme measurement conditions, adsorbates do not populate the surface again and we do not measure a relaxation of V_{CPD}. We underline that the work function difference between ZnO and ZnCoO, as measured by EFM in UHV, is the most accurate

evaluation of the Fermi level shift induced by Co-substitution (5%), turning out as 410 meV.

Finally, we stress out that the adsorbates contribution to the surface band banding in ZnO has been measured as 137mV by in-air KPFM (Figure 3.8) and as 300mV by UHV-EFM (Figure 3.9), both of them after having annealed the sample. Such a difference lies into the time needed to set up the experiments: the first in-air KPFM measurement starts about 30 minutes after the sample has been taken out from the high vacuum chamber, where the annealing is performed; in the case of UHV-EFM, it takes about 1 minute to transfer the samples from the annealing HV chamber to the load-lock of the "Omicron RT-AFM/STM". However, the missing 30minutes of the in-air KPFM experiment have been highlighted as a grey area in Figure 3.8, and the extrapolation of the fitting function at the starting point agrees with a delta V_{CPD} of 300mV.

3.4 Electro-mechanical and charge storing properties

Introduction.

The conversion of electric energy into mechanical one is of fundamental relevance in a word requiring fast developing technologies. In particular, when a great accuracy is required in automation and sensing, the possibility to convert mechanical strain into voltage or vice-versa can fuel emerging fields as smart-sensing and nano-manipulation[8–10]. For all of these reasons, piezoelectric materials are of great interest for the scientific community, even though nano-scale experiments are needed to investigate and develop nano-size transducers. In this scenario, PFM allows the study of the piezoelectric properties at nanoscale[11] . In this section, I'll be proving the piezoelectricity of ZnO by means of PFM and check wheatear it is affected by Co-substitution.

By taking into account that reliable devices need to have a high level of spatial uniformity in the piezoelectric response, I focused on the spatial dependence of ZnO and ZnCoO piezoelectricity, by acquiring PFM maps where amplitude and phase of their piezo-response can be studied with nano-metric resolution.

On the other hand, great interest is also rising into the design of next generation accumulator[12–14], by fruiting of charge storage phenomena. For this reason, I used KPFM technique to investigate such phenomena at the nano-scale, by comparing the response of pure and Co-substituted ZnO, both in dark and under UV light conditions.

Electro-mechanical properties.

The local electro-mechanical response of both ZnO and ZnCoO has been investigated at the nano-scale by means of PFM. Piezoelectric-response to an AC voltage bias have been here measured by means of surface oscillation amplitude and phase maps, acquired on ZnO and ZnCoO and reported in Figure 3.18 and Figure 3.19.

In figure 3.18 the amplitude maps of ZnO (a) and ZnCoO (b) piezoelectric response are shown. Regions with higher piezoelectricity are highlighted in red/yellow in the used color scale.

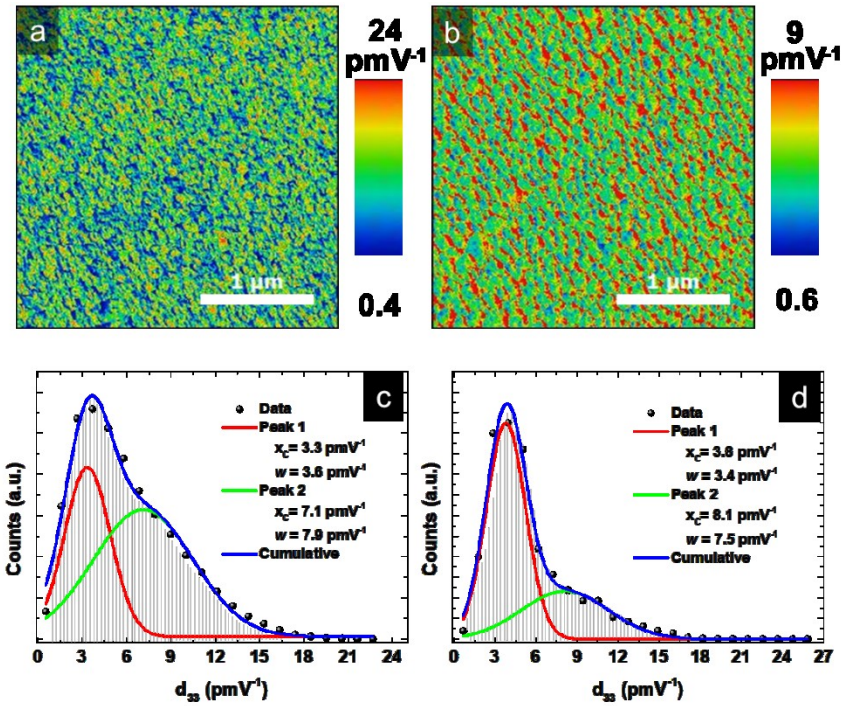

Figure 3. 18 a (**b**) Amplitude maps of PFM acquired on ZnO (ZnCoO). **c** (**b**) Distribution of d_{33} coefficient for ZnO (ZnCoO) recovered from map **a** (**b**).

Furthermore, the histograms of Figures 3.18c,d detail the distribution of the out-of-plane piezoelectric matrix element d_{33} for ZnO and ZnCoO, respectively. By following the procedure reported in Materials and Methods, the $d_{33} = Amplitude[nm]/Vac[V]Q$ values were calculated by rescaling the amplitude maps with respect to both the applied voltage V_{ac} and the quality factor Q of the resonance peak at the working frequency (V_{ac}=500mV at f=50kHz and Q=20-30 in the presented measurements). As shown in Figure 3.18c, the d_{33} distribution of ZnO can be fitted

by a double-peak Gaussian function having mean values at 3.3 pmV^{-1} and 7.1 pmV^{-1} and standard deviation of 3.6 pmV^{-1} and 7.9 pmV^{-1}, respectively. Similarly, the d_{33} distribution of ZnCoO, in Figure 3.18d, has been fitted by a double-peak Gaussian function, centred around 3.8 pmV^{-1}, with a standard deviation of 3.4 pmV^{-1}, and 8.1 pmV^{-1} with a standard deviation of 7.5 pmV^{-1}. Such findings indicate a negligible effect of Co-substitution (5%) into the piezoelectric response of ZnO.

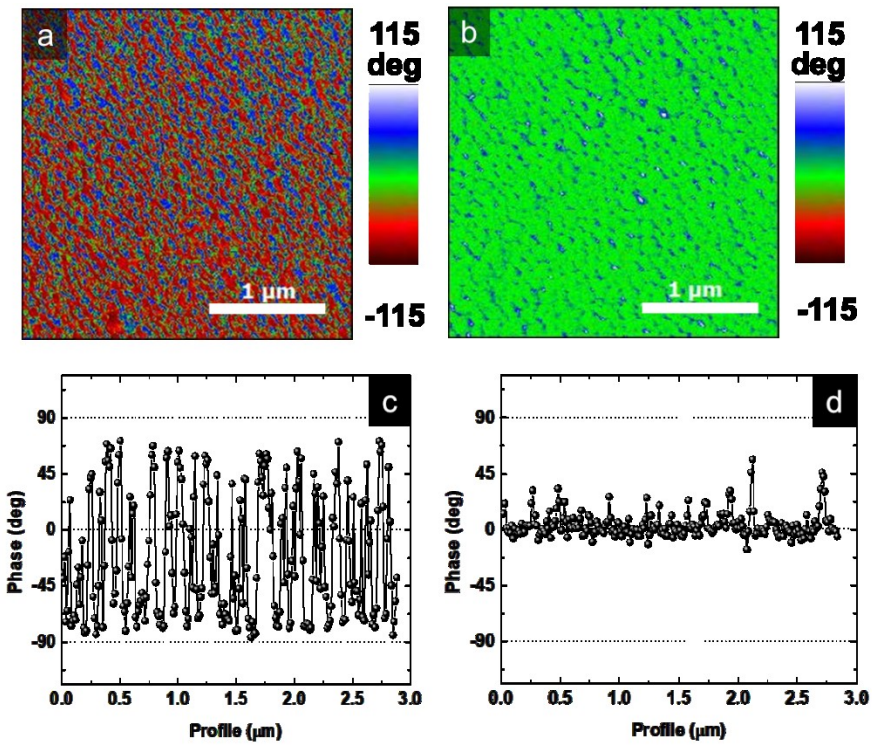

Figure 3. 19 a (**b**) PFM phase maps acquired on ZnO (ZnCoO). **c** (**d**) profile line extracted across phase maps of ZnO (ZnCoO).

While the PFM amplitude provides information on the magnitude of the electromechanical displacements, the PFM phase depends on the polarity of the piezoelectric domains. In perfectly c-axis oriented ZnO films, local spontaneous polarization orientation is either from the top surface to the bottom electrode or vice-versa, depending on the terminating atom (Zn or O) at the surface[15]. Indeed, a

spontaneous polarization is driven by the presence of ions at the surface and always points from Zn face to O face. For perfectly c-axis-oriented ZnO films, the PFM phase image is then either in-phase or out-of-phase with the external AC driving voltage, corresponding to Zn- or O-terminating surface, respectively. This allows the determination of the spontaneous polarization as well as the crystalline orientation of the material by studying PFM phase images.

The piezoelectric phase maps of ZnO (Figure 3.19a) and ZnCoO (Figure 3.19b) clearly show a different orientation of grain polarization between the two materials. Indeed, the same phase contrast range (-115° ÷ +115°) and colour scale have been used for both maps to allow a direct comparison between the two piezoelectric phase responses. In ZnO (Figure 3.19a) the phase colour contrast of subsequent grains switches from red (about -90°) to blue (about +90°), whereas in ZnCoO (Figure 3.19b) the almost uniform green colour contrast is representative of a more homogeneous phase value around 0°. Such a behaviour is highlighted by the line profiles of Figure 3.19c,d. Figure 3.19c shows the phase shift on a single scan line of ZnO: the phase values continuously switches between -90° and +90°. On the opposite, the phase shift of ZnCoO along a single scan line is almost 0° everywhere. Since the piezoelectric polarization is never completely out-of-phase with respect to the external AC bias (the measured phase is never 180°), we can infer the absence of O-terminating polar surface in both samples, whereas in ZnCoO a prevalence of the Zn-terminating faces is measured.

Charge storing effect.

Finally, the charge storage phenomenon both in ZnO and ZnCoO has been investigated by means of KPFM based measurements, consisting in a 3-step experiment. First, sample topography (Figure 3.20a) and KPFM signal (Figure 3.20b) are acquired to check the potential spatial uniformity. Then, a V_{DC} is applied between the tip and a sub-region of the initial scan area (yellow dotted square in

Figure 3.20a,b), by scanning in contact mode. Finally, the KPFM measurement is repeated to check if the poling procedure has locally affected the material potential.

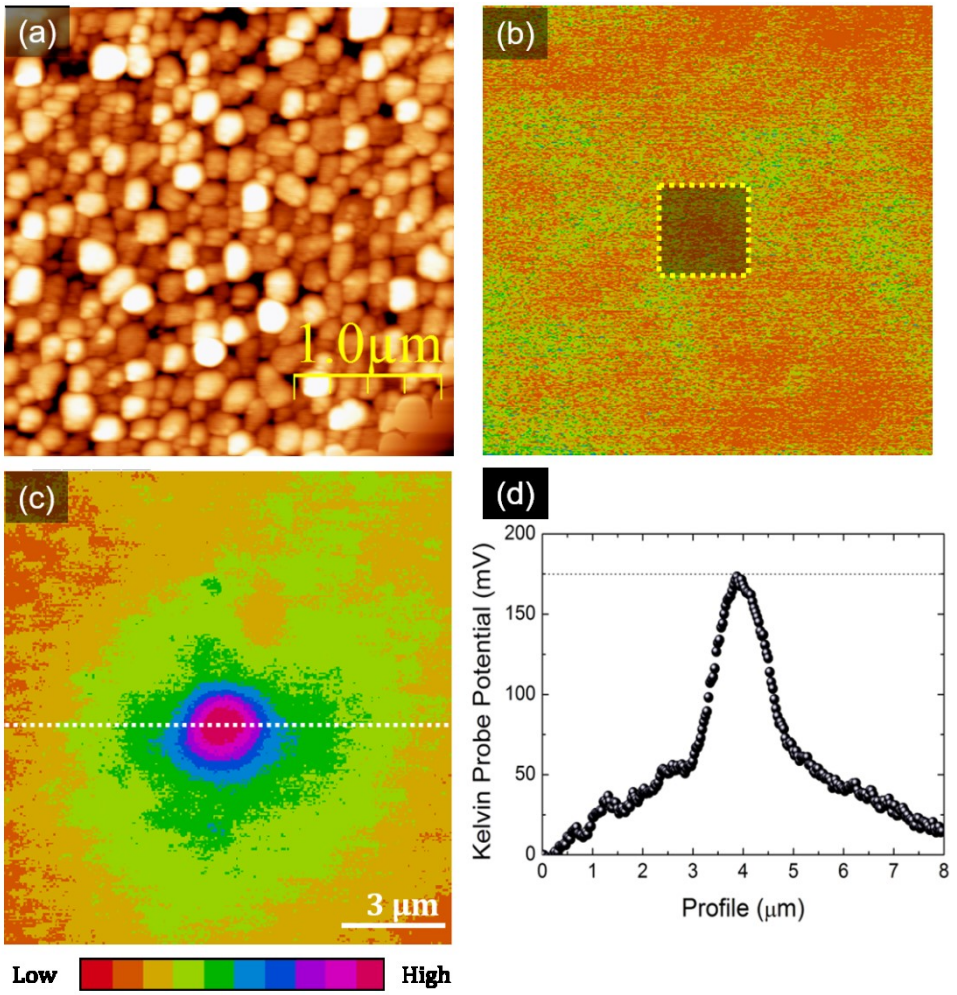

Figure 3. 20 a AFM topography. **b** V_{CPD} map before the poling procedure (that will be performed on the yellow dotted sub-region). **c** V_{CPD} map after the poling procedure. **d** profile line of the poled region along the white dotted line in **c**.

As shown in Figure 3.20c a bump appears into the potential map, in the previously poled area, indicating the presence of a charge storage effect. Figure 3.20d details a potential profile along the white dotted line of figure 3.20c, rescaled with respect to

the minimum value along the scanning line. In this case, the poling with a positive V_{DC} has induced a charge storage, affecting the local potential value by 175 mV or more.

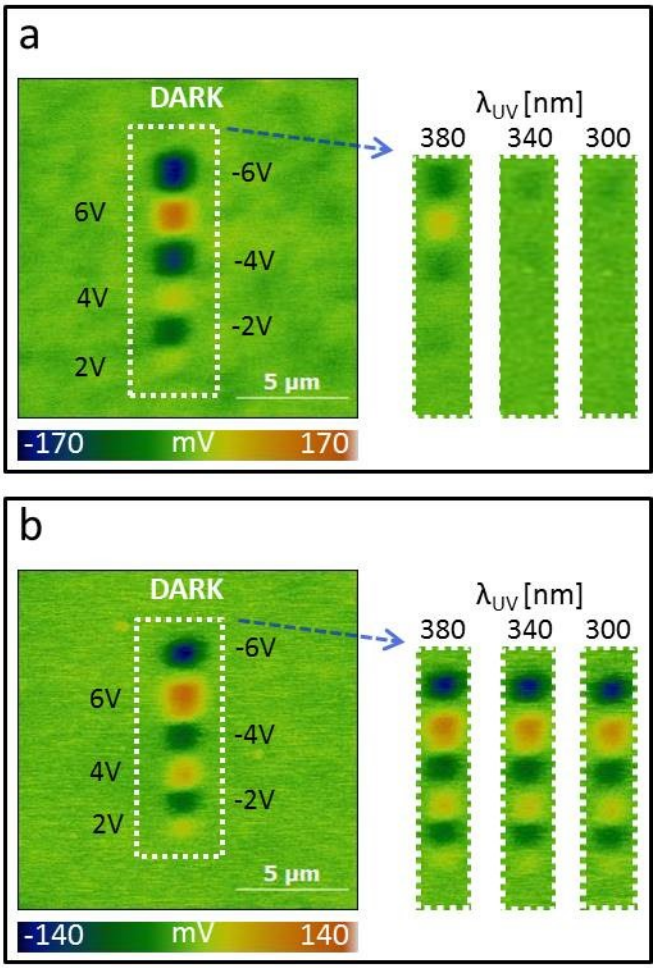

Figure 3. 21 Charge storage measurements performed on **a** ZnO and **b** ZnCoO samples, in dark and UV (380 nm, 340 nm, 300 nm wavelength) light conditions.

Figure 3.21 summarizes the results of charge storage experiments in dark and UV light conditions, with several wavelengths, on both ZnO (a) and ZnCoO (b). As shown in the potential maps of figure 3.21, six near neighbor regions (1µm × 1µm in

size) have been poled, by scanning in contact mode while applying an external DC bias between the metallic PtIr tip and the material. In particular, the same V_{DC}=(+2, -2, +4, -4, +6, -6)V poling biases have been used to induce a charge storage in our samples, realizing a mosaic on the sample surface, read as local V_{CPD} increase (positive V_{DC}) or decrease (negative V_{DC}). Both ZnO and ZnCoO show a charge storage effect when measured by KPFM in dark conditions (left side of Figures 3.21a and b, respectively).

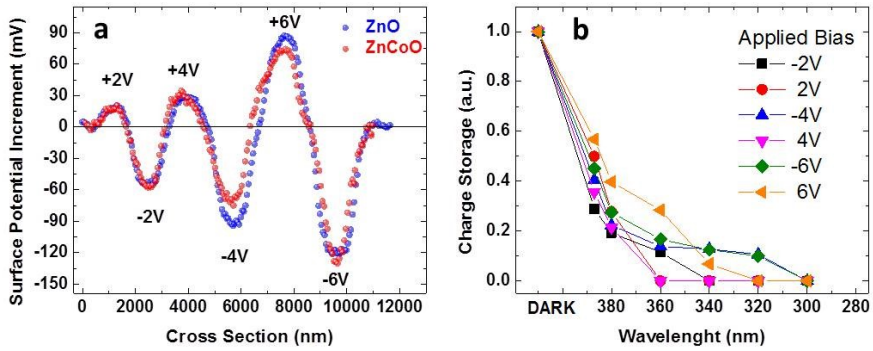

Figure 3. 22 a V_{CPD} profile line along poled areas for ZnO (in blue) and ZnCoO (in red) samples. **b** Behaviour of poled areas in ZnO under UV light conditions.

The colour scale range has been rescaled for both image in figure 3.21, by setting the value of V_{CPD} in the non-poled area as zero. Blue (potential pit) and red (potential bump) colour contrast allow to visualize the charge storage effect, according to the poling bias. Both ZnO and ZnCoO show a significant charge storage effect, with a slightly less intensity on Co-substituted sample. Indeed, the potential scale ranges from -170 mV to 170 mV in ZnO and from -140 mV to 140 mV in ZnCoO. On the other hand, the right-hand side of Figures 3.21 shows the behaviour of charge storage under UV light. In this case, the charge storage contrast on the two materials behaves differently. In ZnO, as the wavelength decreases from 380nm to 300nm, the storage effect is progressively cancelled, whereas no significant changes have been measured in ZnCoO.

Figure 3.22a present a line profile acquired across the V_{CPD} mosaic of charge storing areas, whereas Figure 3.22b shows the cancellation effect at different UV wavelength, for the different biased areas, on ZnO. Figure 3.22a allows to compare the contribution of the charge storage signal to the V_{CPD} shift between pure (blue dots) and Co-substituted (red dots) samples. The two curves exhibit a very good overlap, except for -4 V and +6 V , where ZnCoO shows a lower effect.

On the other hand, Figure 3.22b highlights a different charge storage decreasing trend between positive and negative poled areas of ZnO, when exposed to UV irradiation, with a wavelength spanning from 390 nm down to 300 nm. It does look like that negatively poled areas exhibit a higher endurance under UV-irradiation. However, an UV-light with wavelength of 300 nm is enough to delete any charge storage contribution to the contact potential. In addition to this, it is worth noticing that, if the samples are kept in dark, the charge storage effect lasts for a longer time (more than 1 day).

Discussion.

The effect of Co substitution on piezoelectricity and charge storage properties of ZnO has been investigated exploiting PFM and KPFM experiments. This study has shown that:

(1) Co-substitution (5%) preserves the overall out-of-plane piezoelectricity of ZnO;
(2) Co-substitution (5%) does not alter the charge storage properties of ZnO;
(3) Charge storage properties of ZnO are profoundly affected by UV-lighting;

Co-substitution (5%) makes the charge storage properties of ZnO insensitive to UV-irradiation.

PFM experiments have highlighted a small spatial inhomogeneity of the out-of-plane piezoelectric response of both ZnO and ZnCoO thin films, as indicated by the double-peak Gaussian fitting function of the d_{33} distributions (Figure 3.17a,b). Such distributions are centered in (3.3±3.6) pmV^{-1} – (7.1±7.9) pmV^{-1} and (3.8±3.4) pmV^{-1} – (8.1±7.1) pmV^{-1} for ZnO and ZnCoO respectively. Those values of d_{33} are reasonably the same between ZnO and ZnCoO, in the range of the standard deviations, making the piezoelectric response of ZnO insensitive to Co-substitution (5%). In addition to this, the phase-shift of the piezo-response (Figure 3.19) has been useful to distinguish the eventual polar termination of the films. In particular, piezo-response phase-shift of ZnO is never in- or out- of-phase with the external AC bias, indicating random termination. On the contrary, an in-phase response to the AC voltage is measured on ZnCoO, reflecting a Zn-terminating surface.
On the other hand, I investigated the effect of Co-substitution on charge storing properties of ZnO both in dark and under UV illumination, with wavelength in the range 390-300nm. When working in dark condition, both materials respond to the local negative (positive) DC bias application, showing a local reduction (increase) of V_{CPD}, which increases (in absolute value) as the poling bias increases. This finding indicates that Co content of 5% does not alter the charge storage properties of ZnO. In general, the local change of V_{CPD} under DC bias poling is attributed to three main factors: surface charges, injection of charges, and polarization charges. As show in the previous part, the surface can be discharged by scanning in contact mode with a grounded tip[16] prior performing the electric measurements. On the other hand, the effect of the charge injection becomes efficient only when an Ohmic contact is established between the metallic tip and the sample. Previously discussed KPFM measurements (Figure 3.5) have shown that a Schottky barrier is always expected at the interface between the PtIr tip and both ZnO and ZnCoO samples; as a consequence, charge transfer between the tip and the sample surface is unlikely. On the contrary, electric dipoles can be induced under the application of an external electric field between tip and sample, leading to polarization charges at the sample surface. We infer that this phenomenon plays the biggest role in our systems. Indeed positive (negative) polarization charges at the sample surface, due to the application

of negative (positive) DC bias, locally bend the vacuum level, causing a reduction (increase) of the work function. Such a local change of the work function is read by the KPFM as a pit (bump) of the V_{CPD}, where a negative (positive) bias was previously applied.

Further investigation of charge storage phenomenon in ZnO and ZnCoO under UV-light have highlighted an opposite behavior. On pure material the UV-irradiation has an irreversible effect: the local changes of V_{CPD} due to the poling procedure are completely washed out by the light irradiation. On the contrary, Co-substitution helps in stabilizing the charge storage phenomenon making it insensitive to the used UV-lighting (Figure 3.21).

Such cancellation process can be addressed to the photo-generated carriers that counterbalance the charges induced by poling: in the case of ZnO, a plethora of h-e is generated, as indicated also by UV assisted C-AFM spectroscopy measurements (Figure 3.13), while in the case of ZnCoO its hardness to UV entails the stability of charge storage under UV lighting. In addition to this, in ZnO, the negatively poled areas show a higher hardness (with respect to the positively poled ones) to UV-cancellation, as pointed out in Figure 3.22b. This can be related to the attitude (actually for both materials) in storing positive charge that leads to a down-shift of the Fermi level. The down-shift of the Fermi level leads to the increase of the work function and so to the decrease of the V_{CPD}. The negative poled areas, with a positive charge stored, appear as pits in charge storage maps. Moreover, it is worth noting that in Figure 3.22a areas poled with opposite voltages store a different amount of charge, demonstrating that the attitude in storing positive charge is higher than storing negative ones.

BIBLIOGRAPHY

1. Brillson, L. J. & Lu, Y. ZnO Schottky barriers and Ohmic contacts. *J. Appl. Phys.* **109,** (2011).

2. Li, M. *et al.* Tailoring the charge carrier dynamics in ZnO nanowires: the role of surface hole/electron traps. *Phys. Chem. Chem. Phys.* **14,** 3075 (2012).

3. Kittel, C. *Introduction to Solid State Physics*. (Wiley, 2004).

4. Kisliuk, P. The Sticking Probabilities of Gases Chemisorbed on the Surfaces of Solids. *J. Phys. Chem. Solids* **3,** 95–101 (1957).

5. Ciatto, G. *et al.* Evidence of cobalt-vacancy complexes in Zn1-xCoxO dilute magnetic semiconductors. *Phys. Rev. Lett.* **107,** 127206 (2011).

6. Di Trolio, A. *et al.* The effect of Co doping on the conductive properties of ferromagnetic $Zn_x Co_{1-x} O$ films. *J. Mater. Chem. C* **3,** 10188–10194 (2015).

7. Di Trolio, A. *et al.* Ferromagnetism and Conductivity in Hydrogen Irradiated Co-Doped ZnO Thin Films. *ACS Appl. Mater. Interfaces* **8,** 12925–12931 (2016).

8. Chang, T. & Xuemei Sun. Analysis and control of monolithic piezoelectric nano-actuator. *IEEE Trans. Control Syst. Technol.* **9,** 69–75 (2001).

9. Zaghloul, U. & Piazza, G. 10–25 NM piezoelectric nano-actuators and NEMS switches for millivolt computational logic. in *2013 IEEE 26th International Conference on Micro Electro Mechanical Systems (MEMS)* 233–236 (IEEE, 2013). doi:10.1109/MEMSYS.2013.6474220

10. Wang, X. *et al.* Piezoelectric field effect transistor and nanoforce sensor

based on a single ZnO nanowire. *Nano Lett.* **6,** 2768–2772 (2006).

11. Bonnell, D. A., Kalinin, S. V., Kholkin, A. L. & Gruverman, A. Piezoresponse Force Microscopy: A Window into Electromechanical Behavior at the Nanoscale. *MRS Bull.* **34,** 648–657 (2009).

12. Liu, P., Yang, H. X., Ai, X. P., Li, G. R. & Gao, X. P. A solar rechargeable battery based on polymeric charge storage electrodes. *Electrochem. commun.* **16,** 69–72 (2012).

13. Toupin, M., Brousse, T. & Bélanger, D. Charge Storage Mechanism of MnO 2 Electrode Used in Aqueous Electrochemical Capacitor. *Chem. Mater.* **16,** 3184–3190 (2004).

14. Vlad, A. *et al.* Hybrid supercapacitor-battery materials for fast electrochemical charge storage. *Sci. Rep.* **4,** 4315 (2015).

15. Li, C. P. & Yang, B. H. Local piezoelectricity and polarity distribution of preferred c-axis-oriented ZnO film investigated by piezoresponse force microscopy. *J. Electron. Mater.* **40,** 253–258 (2011).

16. Kumar, A., Herng, T. S., Zeng, K. & Ding, J. Bipolar charge storage characteristics in copper and cobalt co-doped zinc oxide (ZnO) thin film. *ACS Appl. Mater. Interfaces* **4,** 5276–5280 (2012).

4. Conclusions

I fabricated pure and Co-substituted (5%) ZnO thin films by means of pulsed laser deposition (PLD) technique to carry on a comparative study, aiming at investigating the effect of Co-substitution on ZnO. The high quality of such samples has been proved by X-ray diffraction (XRD), whereas energy dispersive spectroscopy (EDS) analysis have confirmed a Co/Zn ratio of 5%, in agreement with the nominal one. Such a specific value of Co concentration has been chosen to compare our results with recent theoretical works, dealing with the appearance of an empty energy band, inside the semiconductor energy gap, led by the formation of Co-oxygen vacancies (Co-V_O) complexes[1,2].

The comparison between ZnO and ZnCoO thin films has been pursued by performing scanning probe microscopy experiments, in different environmental and lighting conditions. As a first result of this study, I start underlining the lower electrical conductivity measured in ZnCoO with respect to pristine ZnO. This result agrees with the formation of Co-V_O complexes, which would drain the free carriers from both donor levels and conduction band (CB). Such a measured lower conductivity is also in agreement with recently proposed experimental investigations[2–4], exploited by macroscopic techniques.

The reduction of charge carrier density in ZnCoO also affects other electrical properties such as the material work function. Indeed by exploiting Kelvin probe force microscopy (KPFM) and electrostatic force microscopy (EFM) experiments, respectively in air and in vacuum, the Fermi level of ZnCoO is proved to move toward the valence band (VB), by a maximum amount of 410 meV, with respect to ZnO Fermi level. On the contrary, no significant change are measured, due to Co-substitution (5%), on the piezoelectric and charge storage properties of ZnO.

Indeed, piezo-response force microscopy (PFM) experiments have demonstrated that ZnCoO shows a similar out-of-plane piezoelectric response, with d_{33} values of the piezoelectric matrix comparable to the ones of ZnO. However, PFM phase indicates that the Co-substitution favours Zn-termination at the material surface,

whereas pure ZnO shows random atomic surface terminations.

Moreover, the charge storage effect has been found on both pure and Co-substituted ZnO. In both cases, the source of such an effect is luckily addressable to a charge induction mechanism, in agreement with the measured Schottky nature of the interface between "metallic (PtIr) probe"/"sample surface", rather than to a charge injection mechanism that would have been favoured when in presence of an Ohmic contact.

Additionally, keeping in mind that the presence of free electrons in n-doped ZnO is responsible of its enhanced surface reactivity (being those ready for chemi/physi-sorption of gas molecules), the reduction of free carriers in ZnCoO (stuck in the Co-Vo energy levels) is expected to suppress its surface reactivity. For this reason, I first proved the presence of charged species at ZnO surface by: (1) conductive atomic force microscopy (C-AFM) experiments at 0V bias, (2) UV-light assisted KPFM in ambient atmosphere, (3) EFM measurements in ultra-high vacuum (UHV), after in vacuum sample annealing. All of these experiments have confirmed the well know property of ZnO to chemisorb reactive oxygen species at its surface. On the contrary, the same experiments carried out on ZnCoO proved its much less reactive surface.

It is worth noting that the presence of negatively charged surface adsorbates in ZnO causes an upward band bending of the vacuum level at the ZnO surface (as well as of the conduction and valence band level). For this treason, the work function of ZnO surface with chemisorbed negative species results higher than the one without those (clean surface). In this scenario, a correct comparison between ZnO and ZnCoO work function requires to remove the adsorbates from ZnO surface (being ZnCoO much less reactive to gas molecules adsorption). By fruiting of UV-light and annealing procedure, I released the surface adsorbates and measured a difference in work function due to Co-substitution of 410 meV, rather than 110 meV, as measured when the ZnO surface is contaminated. By doing this, I also estimated as 300 meV the contribution of the surface adsorbates to band bending and, in turns, on the overestimate of ZnO work function.

In conclusion, I underline that Co-substitution (5%) in ZnO is appealing both for fundamental physics and for applications. On one side it is already well known that

Co makes ZnO a ferromagnetic oxide and I have here demonstrated that it changes its energy band structure, affecting electron conductivity, electrostatic properties and surface reactivity. On the other side, it does not change ZnO electro-mechanical properties, such as its piezo-response and it does not affect the charge storage phenomenon.

BIBLIOGRAPHY

1. Ciatto, G. *et al.* Evidence of cobalt-vacancy complexes in Zn1-xCoxO dilute magnetic semiconductors. *Phys. Rev. Lett.* **107,** 127206 (2011).

2. Di Trolio, A. *et al.* The effect of Co doping on the conductive properties of ferromagnetic $Zn_x Co_{1-x} O$ films. *J. Mater. Chem. C* **3,** 10188–10194 (2015).

3. Ciatto, G. *et al.* Defect-induced magnetism in cobalt-doped ZnO epilayers. **332,** 332–336 (2014).

4. Di Trolio, A. *et al.* Ferromagnetism and Conductivity in Hydrogen Irradiated Co-Doped ZnO Thin Films. *ACS Appl. Mater. Interfaces* **8,** 12925–12931 (2016).

Acknowledgments

First, I would like to thank my advisor, Prof. Fabrizio Bobba, for supporting and guiding me with great experience and passion. I wish him to continue to teach and research with enthusiasm.

I feel grateful to Prof. Anna Maria Cucolo for her suggestions and the passion she transmits in making science.

I would like to acknowledge Prof. Roberto Scarpa, as Ph.D. coordinator, together with the Doctoral Council.

Nobody's critiques sound like suggestions and encouragements as Dr Cinzia Di Giorgio's critiques. Brotherly thanks, to be present every day in this scientific route: I cannot desire a better colleague. I wish her a brilliant career as she deserves.

I would like to express my gratitude to Dr. Antonio Di Trolio for giving me the possibility to produce samples by means of its PLD equipment and for his suggestions.

I thank Dr Aldo Amore Bonapasta and Dr Paola Alippi for their theoretical modelling and advices.

The UV-assisted measurements have been carried out by means of a monochromatic light system provided by Dr Nicola Zema, that I kindly thank.

I feel grateful to all of my Ph.D. collegues for their friendship, good times shared together and very useful discussions.

Author's Publications

IN JOURNALS

A. Guarino, P. Romano, F. Avitabile, A. Leo, N. Martucciello, G. Grimaldi, A. Ubaldini, **D. D'Agostino**, F. Bobba, A. Vecchione, S. Pace, and A. Nigro, "Characterization of $Nd_{2-x}Ce_xCuO_{4\pm\delta}$ (x = 0 and 0.15) Ultrathin Films Grown by DC Sputtering Technique," **IEEE Transactions on Applied Superconductivity**, vol. 27, no. 4, pp. 1-4, June 2017. doi: 10.1109/TASC.2016.2634319

D. D'Agostino, C. Di Giorgio, A. Di Trolio, A. Guarino, A.M. Cucolo, A. Vecchione and Fabrizio Bobba, "Piezoelectricity and charge trapping in ZnO and Co-doped ZnO thin films", **AIP Advances**, vol. 7, no. 5, pp. 055010, 2017. doi:10.1063/1.4983474.

C. Di Giorgio, F. Bobba, A.M. Cucolo, A. Scarfato, S.A. Moore, G. Karapetrov, **D. D'Agostino**, V. Novosad, V. Yefremenko, M. Iavarone, "Observation of superconducting vortex clusters in S/F hybrids", **Scientific Reports**, vol. 6, no.38557, 2016. doi:10.1038/srep38557

IN BOOKS

C. Di Giorgio, F. Bobba, A. Scarfato, **D. D'Agostino**, M. Iavarone, G. Karapetrov, S. A. Moore, M. Polichettia, D. Mancusia, V. Novosad, V. Yefremenko, and A. M. Cucolo, "Low Temperature Magnetic Force Microscopy Studies of Static and Dynamic Vortex-Antivortex Configurations in Magnetically-coupled Superconductor-Ferromagnet Hybrids", Invited Chapter, **Vortex Dynamics and Optical Vortices**, ISNN 978-953-51-4886-9, 2016.